NEGATIVE TONE EPOXIDE MOLECULAR RESISTS AND MATERIALS FOR NEXT GENERATION LITHOGRAPHY

A Dissertation
Presented to
The Academic Faculty

by

Hannah L. Narcross

In Partial Fulfillment
of the Requirements for the Degree
Doctor of Philosophy in the
School of Chemistry and Biochemistry

Georgia Institute of Technology
AUGUST 2019

NEGATIVE TONE EPOXIDE MOLECULAR RESISTS AND MATERIALS FOR NEXT GENERATION LITHOGRAPHY

Approved by:

Dr. Clifford L. Henderson, Advisor
School of Chemical & Biomolecular Engineering, School of Chemical & Biomedical Engineering
Georgia Institute of Technology, University of South Florida

Dr. David G. Bucknall
School of Engineering and Physical Sciences
Heriot-Watt University

Dr. Peter J. Ludovice, co-Advisor
School of Chemical & Biomolecular Engineering
Georgia Institute of Technology

Dr. David M. Collard
School of Chemistry & Biochemistry
Georgia Institute of Technology

Dr. Laren M. Tolbert, co-Advisor
School of Chemistry & Biochemistry
Georgia Institute of Technology

Dr. Carlos Silva
School of Chemistry & Biochemistry
Georgia Institute of Technology

Date Approved: [April 17, 2019]

ACKNOWLEDGEMENTS

Simply put, none of this would have been possible without the support and guidance from my advisor Dr. Henderson. His advice and keen insight into problems over the years has been invaluable and I am incredibly grateful for all of the opportunities I have had while in his research group. I am also grateful for the support from my co-Advisor Dr. Ludovice whose humor and optimism helped me through the many low points of graduate school. I would also like to express my gratitude towards my other co-Advisor Dr. Tolbert and all of my committee members (Dr. Bucknall, Dr. Collard, and Dr. Silva) for their help and feedback throughout my time here at Georgia Tech. The other past members of my research group have also been invaluable sources of support and advice; Dr. Richard Lawson who was an excellent mentor and taught me so much about chemistry and lithography during my first year, Dr. Andrew Peters, Dr. Ben Nation who literally spent hours of his free time helping me in lab without complaint, and Dr. Caleb Breaux who was always willing to help no matter how bizarre the request or how busy he was. I would like to thank in particular Dr. Brandon Sharp for his excellent company and humor over the years, and who has been a great example of professionalism and attitude. Devin Brown has also been a great source of help over the years and I am very thankful for his assistance and willingness to answer my endless questions about electron-beam lithography.

There is no way that I would be writing this right now without the constant support from my friends and family. I was fortunate to move to Atlanta and start graduate school at the same time as Carolyn Buckley who helped immensely with all the struggles of the first few years and has remained a friend and colleague ever since. I've also been incredibly

lucky to have not one, but two fantastic role models of women in science in my mother and older sister Lauren who have helped so much in my growth as a scientist and as a person. Finally, my husband Tyler. Expressing the entirety of my gratitude for him and his support would easily take up another hundred pages which certainly no-one wants to read, so I'll summarize with this. I couldn't have asked for a better partner and teammate throughout the many challenges of graduate school over the years, and I look forward to many more (hopefully at least *slightly* less challenging) years together.

TABLE OF CONTENTS

LIST OF FIGURES

LIST OF SYMBOLS AND ABBREVIATIONS

^{1}H NMR	Proton-1 nuclear magnetic resonance
ACN	Acetonitrile
AIBN	Azobisisobutyronitrile
AS	Acetoxy styrene
BCB	Benzocyclobutene
BCP	Block copolymer
CAR	Chemically-amplified resist
CD	Critical dimension
DCM	Dichloromethane
DI	Deionized
DMSO	Dimethyl sulfoxide
DUV	Deep ultraviolet
E_0	Dose-to-clear
E_{size}	Dose-to-size
EBL	Electron-beam lithography
EL	Ethyl lactate
Ep	Epoxide
ESI-MS	Electrospray-ionization mass spectrometry
FTIR	Fourier transform infrared spectroscopy
GPC	Gel permeation chromatography
EUV	Extreme ultraviolet
IC	Integrated circuit

IPA	Isopropanol
LER	Line-edge roughness
LWR	Line-width roughness
MDSC	Modulated differential scanning calorimetry
MIBK	Methyl isobutyl ketone
NBn	Nitrobenzyl
NGL	Next-generation lithography
NRT	Normalized remaining thickness
PAB	Post-apply bake
PAG	Photoacid generator
PEB	Post-exposure bake
PDN	Photo decomposable nucleophile
PGMEA	Propylene glycol monomethyl ether acetate
RLS	Resolution, line edge roughness, sensitivity
PHEMA	Poly(hydroxyethylmethacrylate)
PHOST	Poly(p-hydroxystyrene)
PMMA	Poly(methyl methacrylate)
PS	Poly(styrene)
SEM	Scanning electron microscope
TAS	Triarylsulfonium
T_g	Glass transition temperature
TGA	Thermogravimetric analysis
TPS	Triphenylsulfonium
UV	Ultraviolet

SUMMARY

The ability to quickly and accurately form nanoscale two-dimensional structures is critical for the high-volume manufacturing of semiconductors and microelectronic devices. Significant progress has been made in developing new exposure sources for next-generation lithography, but scaling challenges, especially at sub-20-nm features will require new materials capable of meeting the strict performance requirements laid out by the International Technology Roadmap for Semiconductors.

Organic molecular resists have been proposed as a possible alternative to traditional polymeric photoresists due in part to their smaller molecular weight and narrower dispersity, but have yet to meet the necessary resolution, line edge roughness, and sensitivity standards for next-generation lithography. One promising type of organic resists are negative-tone photoresists based on the cationic polymerization of epoxides, due to their resistance to pattern collapse which is a common source of patterning failure at sub-100-nm length scales. This thesis will discuss some of the research that has been conducted on understanding structure-property relationships governing the patterning performance of these materials and developing novel additives to improve their performance including cross-linkable photoacid generators capable of use at ultra-high loadings to improve sensitivity and line edge roughness, and phenol-functionalized polymerization control additives to improve resolution.

An alternative lithographic technique that has attracted growing interest over the years is the directed self-assembly (DSA) of block copolymers which offers a means to extend the use of older lithographic technologies or be used complementarily with newer

exposure sources. DSA requires that a substrate be patterned chemically (chemoepitaxy) and/or topographically (graphoepitaxy) with guiding patterns in order to form lithographically useful orientations of morphologies with long range order and low defectivity. This thesis will also discuss some progress made towards developing a non-chemically amplified photodefinable underlayer which can have arbitrary guiding patterns directly written onto it using current (298 and 193 nm) or next-generation (extreme ultraviolet and electron-beam) exposure sources.

CHAPTER 1. INTRODUCTION

1.1 Moore's Law

One of the greatest influences on modern technology is Moore's law, an observation by Gordon Moore in 1965 that the number of transistors per square inch of an integrated circuit chip was doubling every two years and the prediction that this trend would continue for the foreseeable future.[1] What started as a simple observation has become a self-fulfilling prophecy as the semiconductor manufacturing industry has since adopted it as an industry mandate and has integrated Moore's Law thoroughly into its standards and roadmap for future technologies.[2] Moore's Law has also been described as an economic law since if the cost per wafer remains the same, then the cost per transistor will also be halved every two years. The dramatic increase in processing power and drop in cost of computational power over the years enabled by semiconductor manufacturers fighting to adhere to Moore's law has led to the ubiquity of microelectronic devices in almost all facets of society including transportation, education, health care, and consumer goods.

Maintaining Moore's Law has chiefly been enabled by improvements in lithography, the technique used to transfer patterns onto silicon for integrated circuit (IC) fabrication. The ability to quickly and accurately form nanoscale two- and three-dimensional structures is critical for the high-volume manufacturing of semiconductors and microelectronic devices. There are currently significant scaling challenges especially as feature sizes approach molecular and atomic length scales, which will require innovative solutions in patterning technologies, exposure sources, and materials to overcome.[3]

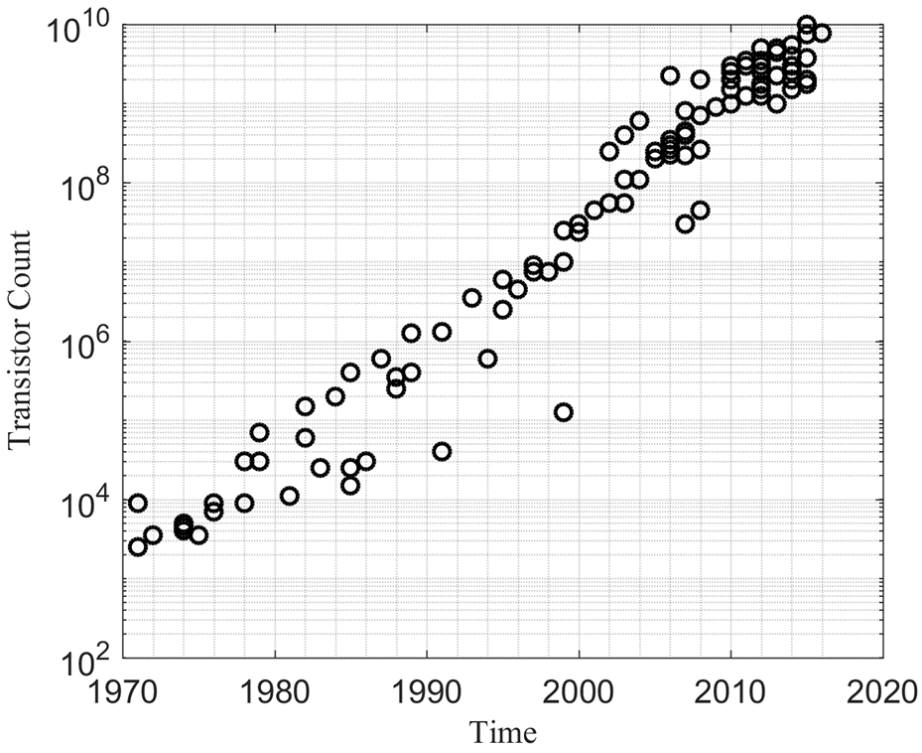

Figure 1.1 Illustration of Moore's Law showing the number of transistors in microprocessors at their date of introduction which doubles every two years.[4]

1.2 Photolithography

The most common form of lithography currently used in high volume semiconductor manufacturing is optical/photo lithography, which uses light to ultimately transfer a pattern onto a substrate (typically a silicon wafer). A simplified optical lithographic process is as follows (illustrated in Figure 1.2). First, a material known as a photoresist is coated onto a silicon substrate. Light is then shone through an opaque mask which is patterned with transparent regions onto the resist to selectively expose areas of the photoresist. This light initiates reactions that change the solubility of exposed regions of the photoresist in a developing solvent. In positive-tone resists, exposed regions become more soluble and are dissolved, leaving behind a positive relief pattern of the original mask. In negative-tone

resists (the focus of this work) exposed regions become less soluble, leaving behind a negative relief pattern. The relief pattern is used as a protective layer during an etch step which transfers the pattern into the substrate, after which any remaining photoresist is stripped. These exposure/development/etch steps may be repeated multiple times until the complete IC component has been fabricated.

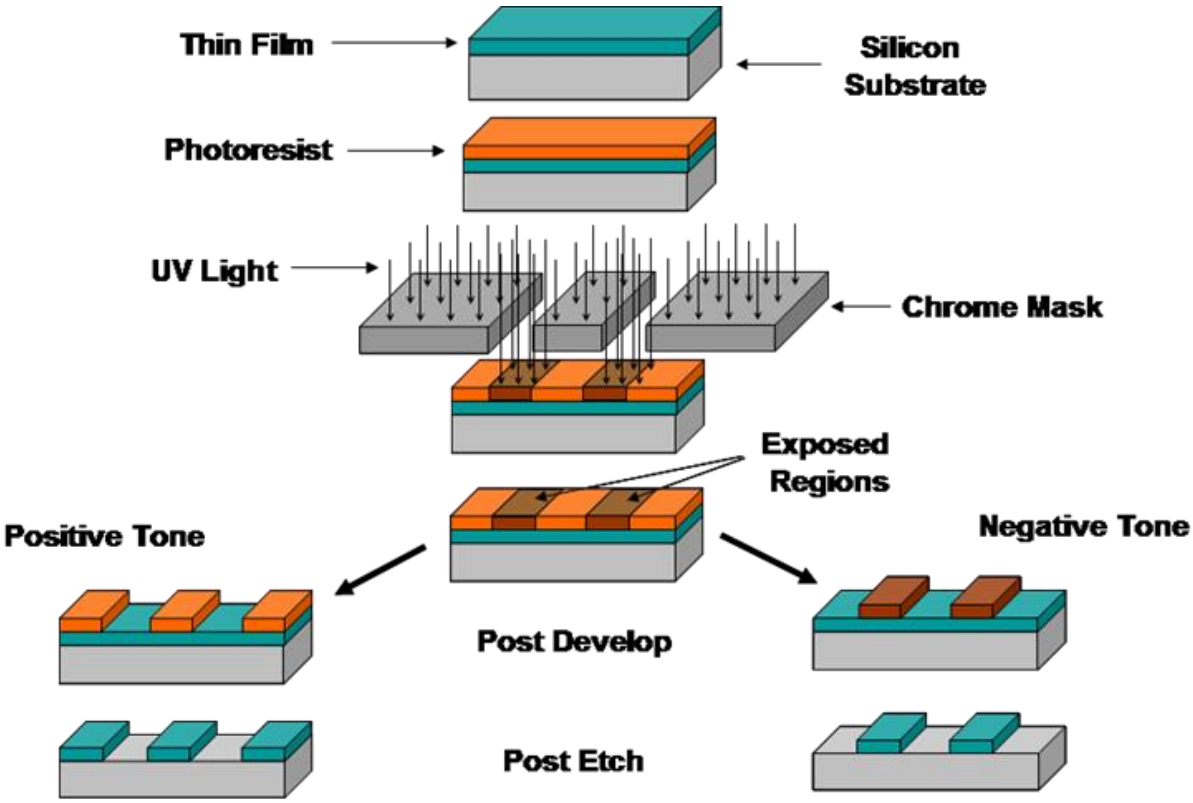

Figure 1.2 Simplified optical lithography process flow.

The resolution of the patterned feature is highly dependent on the wavelength of the light used during the exposure step (the relationship of which is described in Equation (1.1)) where CD is the Critical Dimension (size) of a feature, λ is the wavelength of light of the exposure source, NA is the Numerical Aperture of the system, and k is a process dependent constant.[5]

$$CD = k\frac{\lambda}{NA} \tag{1.1}$$

Much of the progress in shrinking transistor sizes has been enabled by developing new light sources using increasingly smaller wavelengths with exposure sources over the years evolving from 436 nm light in the 1960s to the current workhorse of the industry, 193 nm light. Each change in light source is a non-trivial process often requiring entirely new materials and resist chemistries, processes flows, and expensive exposure tools. Another means of CD reduction is to increase the NA of the system by introducing a medium with a different index of refraction between the lens of the light source and the material being patterned (described in Equation (1.2) where n is the refractive index and θ is the half-angle of the cone of light exiting the lens). At an angular aperture of 180 ° (or a half-angle value of 90 °) the value of sin θ becomes 1 illustrating that the imaging medium refractive index is an important limiting factor in the possible numerical aperture achievable by high-performance objective lenses.

$$NA = n\sin\theta \tag{1.2}$$

Introducing this medium between the lens and the substrate into the manufacturing line is also a non-trivial process and requires both photoresists and lenses that are compatible with the new medium. 193 immersion (193i) lithography using high-purity water as a liquid medium is the predominate means of semiconductor manufacturing at the current 7 nm technology node and, with the use of complicated patterning techniques such as Self-Aligned Quadruple Patterning (SAQP), has extended 193i lithography well beyond its minimum pitch limitations. Even with these patterning techniques 193i cannot be

extended indefinitely and is rapidly approaching its fundamental physical limitations[6], thus alternative technologies are needed for next-generation lithography (NGL).

Significant research and development has been focused on developing replacements for 193i lithography. One proposed alternative is electron-beam or e-beam lithography (EBL) which uses a focused beam of 50 – 100 keV electrons to directly expose areas of a photo-resist. Some major advantages of e-beam lithography are the ability to arbitrarily pattern complicated features without the need of a mask, and the small beam size (which can reach sizes down to 8 nm) which has achieved down to 2 nm isolated features.[7, 8] Despite the benefits of EBL, it has not been adopted in high volume semiconductor manufacturing due to its much slower throughput than optical lithography. Instead of blanket exposing wafers, each pixel must be individually written, which makes the throughput slow and prohibitively expensive. Currently, EBL is primarily used as a means of writing high-resolution low-defect masks for optical lithography. Some efforts have been made to improve the throughput of EBL through the development of technologies such as projection e-beam, multiple-beam, and reflective-beam which are still in the early stages of development.[9] Another proposed NGL technology that has been continuously in development for decades is Extreme Ultraviolet (EUV) lithography, which uses a laser-induced tin plasma to generate 13.5 nm light.[10, 11] According to Equation (1.1), adopting EUV as a light source should dramatically shrink the possible CD size, however, multiple issues have prevented its widescale implementation including difficulties with optics and low power of the light sources. Despite these issues EUV is widely anticipated to be the dominate NGL technique used in future technology nodes.[3]

Regardless of the exposure source, the resolution of patterned features is still dependent on the ability of the photoresist to form well-defined defect free features at required length scales. New materials and resist chemistries are required to keep pace with NGL techniques and enable high-volume manufacturing at future nodes.

1.3 Photoresists

1.3.1 Figures of Merit of Resist Performance

Photoresists and the chemistries used to switch their solubility can vary greatly between the different lithographic techniques and light sources used, but there are some basic material and patterning performance requirements that they all must meet. Photoresists must be able to form high-quality films that adhere to various substrates, have good chemical contrast in a developer between unexposed and exposed regions, be thermally and chemically stable during processing and storage, and have a high etch resistance to the etch process used to transfer resist relief patterns into the substrate. In terms of patterning performance, photoresists are judged on the following figures of merit:

Resolution: the smallest feature that can be successfully imaged with acceptable quality and control. While resolution is heavily dependent external factors such as the exposure tool (as previously discussed) and other processing conditions, the photoresist must be able to image high quality, high resolution (small CD) features that can survive post-exposure processing and development.

Roughness: reported in terms of Line Edge Roughness (the deviation in the edge of a patterned line from the ideal smooth line edge, typically reported as the 3σ value) and Line

Width Roughness (the deviation in width along a patterned line also reported as 3σ value) (Figure 1.3). It is critical that these values are low, especially at sub 100 nm features, where a high LER/LWR can lead to defects in the final patterned features and device performance.[12, 13] LER/LWR can be caused by a variety of sources including stochastic events from the exposure tool, the resist chemistry, and even the physical distribution of the molecules in the resist.

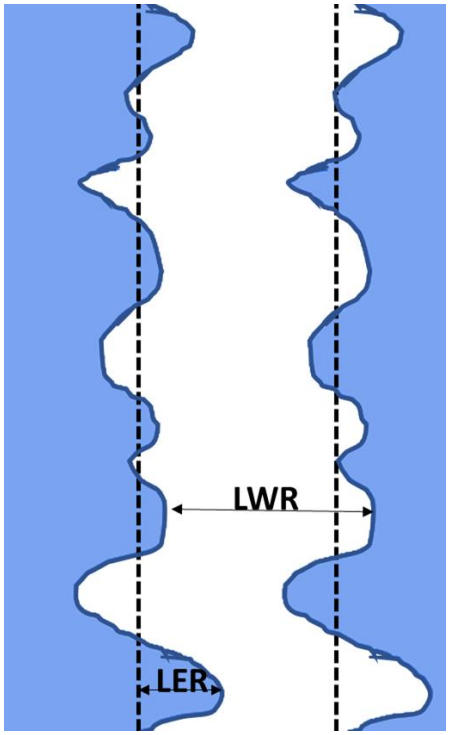

Figure 1.3 Graphical illustration of Line Edge Roughness (LER) and Line Width Roughness (LWR) in a printed feature.

Sensitivity: the dose (reported as amount of energy per unit area) required to successfully pattern a feature. In positive tone resists, where the exposed photoresist is selectively removed with a developing solvent, sensitivity is typically reported as dose-to-clear (E_0) or the dose required such that exposed areas are completely removed. Dose-to-size (E_{size}) is a more generic term of sensitivity which simply refers to the dose required to produce

the proper dimension of the resist feature. In negative tone resists, where exposed photoresist is rendered insoluble in a developing solvent, sensitivity is typically reported as E_{50} / E_{100} or the dose required such that 50 /100 % of the original thickness of the photoresist remains following development. The sensitivity of a photoresist must be high enough (in other words must require a low enough dose) that exposure can be done rapidly and ensure high throughput, but not so low that stochastic events such as lens flare or temperature aberrations cause defects in the patterned feature.[14]

1.3.2 Chemically Amplified Resists and the RLS Trade-off

Chemically amplified resists (CARs) are resists in which a single photon can catalyze multiple solubility switching reactions, dramatically improving their sensitivity compared with non-amplified resists. For this reason, CARs have dominated high-volume manufacturing and are used today in almost all high-resolution patterning. Typically, CARs use a photoacid generator (PAG) additive which upon exposure generates photoacids that trigger multiple reactions in the resist (generally carried out at elevated temperatures during a post-exposure bake (PEB) step). There are a wide variety of CAR chemistries and methods of providing local solubility/insolubility switching, but generally speaking in positive tone resists photoacids catalytically deprotect groups such as phenols and carboxylic acids rendering the resist soluble in an aqueous base developer. This deprotection chemistry can also be used in negative tone resists by rendering exposed regions insoluble in an organic developer. The most commonly used PAGs are onium salts which can generate a variety of photoacids depending on which anion is used (Figure 1.4).

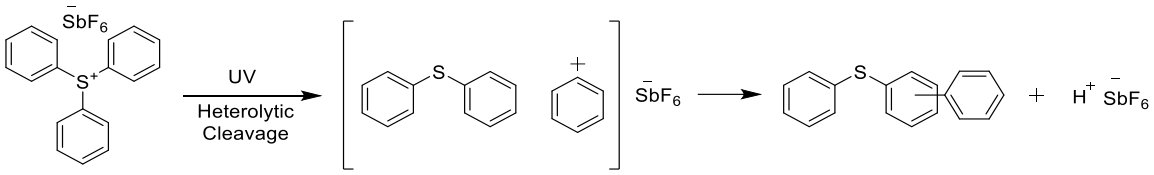

Figure 1.4 Example of the generation of a photoacid from an onium salt photoacid generator (TPS-SbF_6).

The generation, distribution, and diffusion of photoacids in CARs affects almost every aspect of their patterning performance. Photoacids generated during exposure must be able to diffuse throughout the resist to carry out reactions, however if they diffuse too far they can catalyze solubility switching reactions outside of exposed regions and lead to a loss of resolution (Figure 1.5). If the diffusion constant is too low, then sensitivity can be poor and the LER might be overly dependent on the statistical distribution of PAGs in the resist. If the amount of a PAG with a low diffusion constant is raised to improve its statistical distribution and LER, then once again sensitivity and LER are improved but with a commensurate loss in resolution.

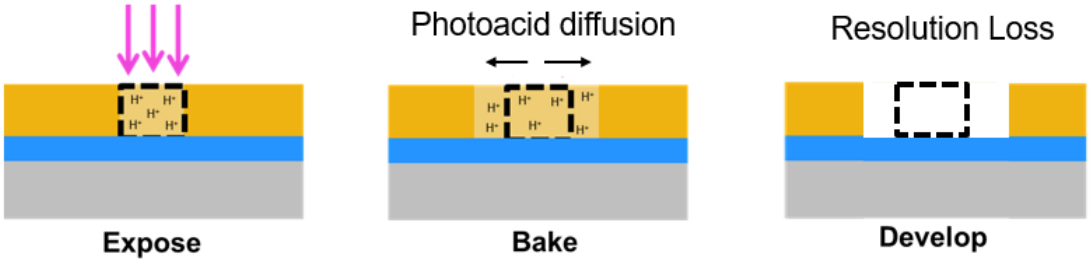

Figure 1.5 Illustration of line-broadening (resolution loss) in a chemically-amplified positive tone resist due to photoacid diffusion.

This fundamental trade-off between resolution, sensitivity, and LER exists across all resists (regardless of physical properties and patterning mechanisms) and is referred to as the RLS trade-off where any improvement of one or two of the performance metrics can

only be improved at the expense of the third.[15, 16] This relationship has been experimentally and mathematically verified to follow Equation (1.3) to give the value "Z" or the "z-parameter" which can be used to roughly gauge the relative performance of a photoresist. .[17]

$$Resolution^3 \times LER^2 \times Sensitivity \approx Z \quad (1.3)$$

There have been many attempts at breaking the RLS trade-off, none of which have been successful so far, and it remains one of the greatest challenges of resists for next-generation lithography.[18] However, it is possible to "shrink" the Z value illustrating that new photoresists can be developed with superior patterning performance while still being fundamentally limited by the RLS trade-off.

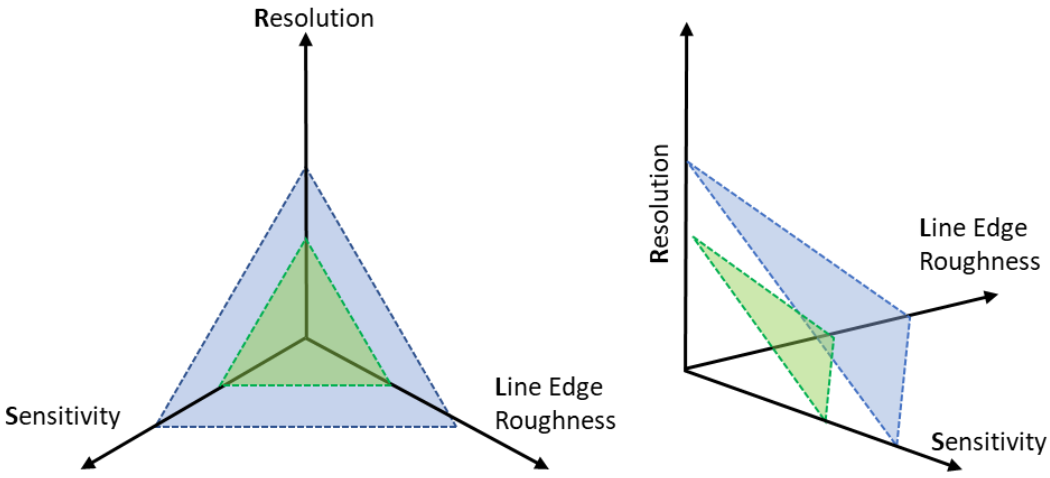

Figure 1.6 Illustration of the RLS trade-off of two photoresists with different Z values.

1.3.3 Molecular Resists

Traditionally, non-chemically amplified resists have been composed of polymers such as Novolac, PMMA, and polymers with acid-labile protecting groups on polar

functionalities. At sub-32 nm length scales however, polymer molecular weight/molecular weight distribution[19, 20] as well as the aggregation of small molecule additives such as PAGs[21], have been demonstrated to cause poor patterning performance and been a fundamental physical limitation to their use with NGL techniques such as EUV and EBL.

Molecular resists, also referred to as molecular glass resists, are photoresists that are composed of small, low-molecular weight molecules and have been proposed as an alternative to traditional polymeric resists for NGL.[22, 23] Some of their potential advantages over polymer resists include a significantly smaller molecular size and a much narrower molecular weight distribution (potentially even monodisperse) which should provide higher resolution and a lower line edge roughness, respectively.[24-26] Additionally they have smaller free volume which should limit photoacid diffusion (a source of resolution loss as previously discussed) and should have better mixing with other small molecule additives such as PAGs and base quenchers. Better mixing helps prevent additive aggregation and an inhomogeneous distribution of resist components.[27] Improving this homogeneity and decreasing additive aggregation has also been demonstrated as another means of improving LER.[28] A graphic illustration of some of these concepts is shown in Figure 1.7.

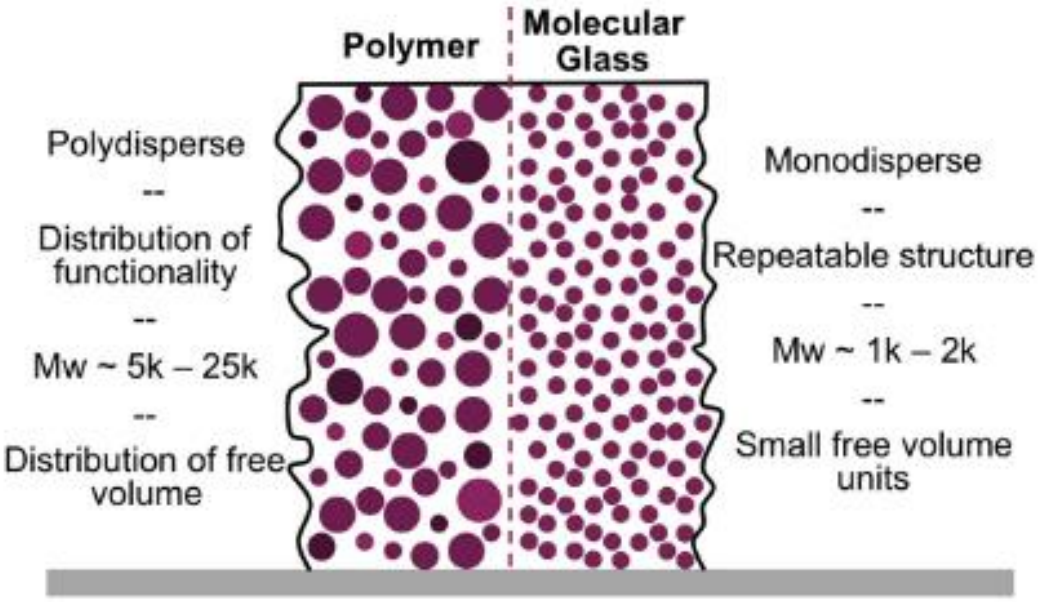

Figure 1.7 Comparison of the structural properties between polymer and molecular resists.[29]

Another aspect of molecular resists that have made them attractive candidates for high-resolution lithography is their tight chemical and structural control, which has allowed for the development of a wide variety of systems including fullerenes[30], polyphenols[31], and the cationic polymerization of epoxides.[32]

1.3.4 Negative Tone Epoxide Resists

A specific class of molecular resist, organic negative tone resists based on the photoacid initiated cationic polymerization of epoxides, are of particular interest for the following reasons. The cationic polymerization reaction is insensitive to oxygen and atmospheric base contaminants and consequently does not suffer from "t-topping" where ambient amines from sources such as processing chemicals interfere with the solubility switching mechanism at the surface of patterned features and distort its side profile. No volatile products are produced during solubility switching reactions (ring opening

polymerization), reducing the concerns of outgassing byproducts interfering with exposure optics. Another benefit of these resists is that the active species is a polymerizing chain end (which is inherently diffusion controlled as the extent of cross-linking increases) instead of a small free photoacid. One of their most significant advantages is their demonstrated improved resistance to a phenomenon known as pattern collapse.[33]

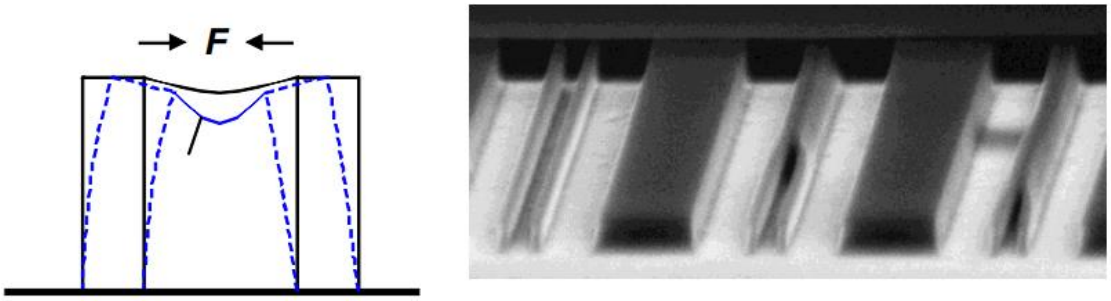

Figure 1.8 Graphical representation of pattern collapse of patterned features following development.[34]

Pattern collapse (the collapse of patterned features following exposure and development) occurs due to the physical capillary forces exerted by developer solvent onto the sidewalls of patterns as it dries (illustrated in Figure 1.8).[35] As described by Equation (1.4) (where σ is the capillary forces exerted on the resist, γ is the surface tension of the liquid, θ is the contact angle of the final rinse liquid on the resist feature side wall, H/W is the aspect ratio of the feature, and S_1 is the space between features), these forces scale with the size and density of features and thus pattern collapse will only become even more of an issue at future nodes.[36] [37]

$$\sigma = 6\gamma \cos\theta \left[\frac{H}{W}\right]^2 \left[\frac{1}{S_1}\right] \quad (1.4)$$

There has been significant research into different developing strategies to improve pattern collapse such as modifying the surface tension of the developing solvent with surfactants or selecting developers with inherently lower surface tensions such as perfluorohexane and supercritical carbon dioxide but these typically come with other drawbacks or require compatible resists that might not have the requirements necessary to be implemented at current nodes.[38-42] Other strategies such as the Dry Development Rinse Process (DDRP) seek to remove the need for a wet developer altogether but these generally require special equipment that dramatically increases the complexity and length of the lithographic process flow making them prohibitively expensive to implement in high-volume manufacturing.[43] It is instead preferable to design photoresists with inherent physical properties such as a higher mechanical modulus that make them more resistant to pattern collapse.[33]

Cross-linked polymeric resists have also been explored in the past as negative tone materials, but their tendency to swell during development due to their low cross-link density limited their usefulness. Epoxide-functionalized molecular resists can achieve much higher cross-link densities and have been demonstrated to have inherently higher moduli and resistance to pattern collapse making them attractive materials for next-generation lithography.[44, 45] Some of these materials have already demonstrated promising high-resolution patterning performance with low LER values and excellent resolution.[46] The major focus of this work has been to understand some of the fundamental structure-property relationships governing their performance, and developing novel additives to improve their performance even further.

1.4 Directed Self Assembly

Due to the complexity and cost of patterning dense, small features using optical lithography, several alternative lithography techniques have been investigated and are currently being developed. Some of these include ion beam lithography,[47] which writes patterns using a focused beam of ions (similar to e-beam lithography), scanning probe lithography[48] which uses a probe tip to chemically or physically pattern a substrate, and nanoimprint lithography[49] which uses a mold to define patterns in a liquid resist which is then optically or thermally cured followed by the removal of the mold. One method of particular interest is the directed self-assembly (DSA) of block copolymers (BCPs) which harnesses the natural ability of certain block copolymers to naturally microphase separate into ordered periodic domains.[50] The morphology and size of these domains is dependent on the volume fraction (f_i) of each block as well as the product χN.[51] The Flory-Huggins parameter (χ) describes the heat of mixing between the two blocks, or the degree to which one block prefers to interact with itself and N describes the degree of polymerization or size of the BCP.[52]

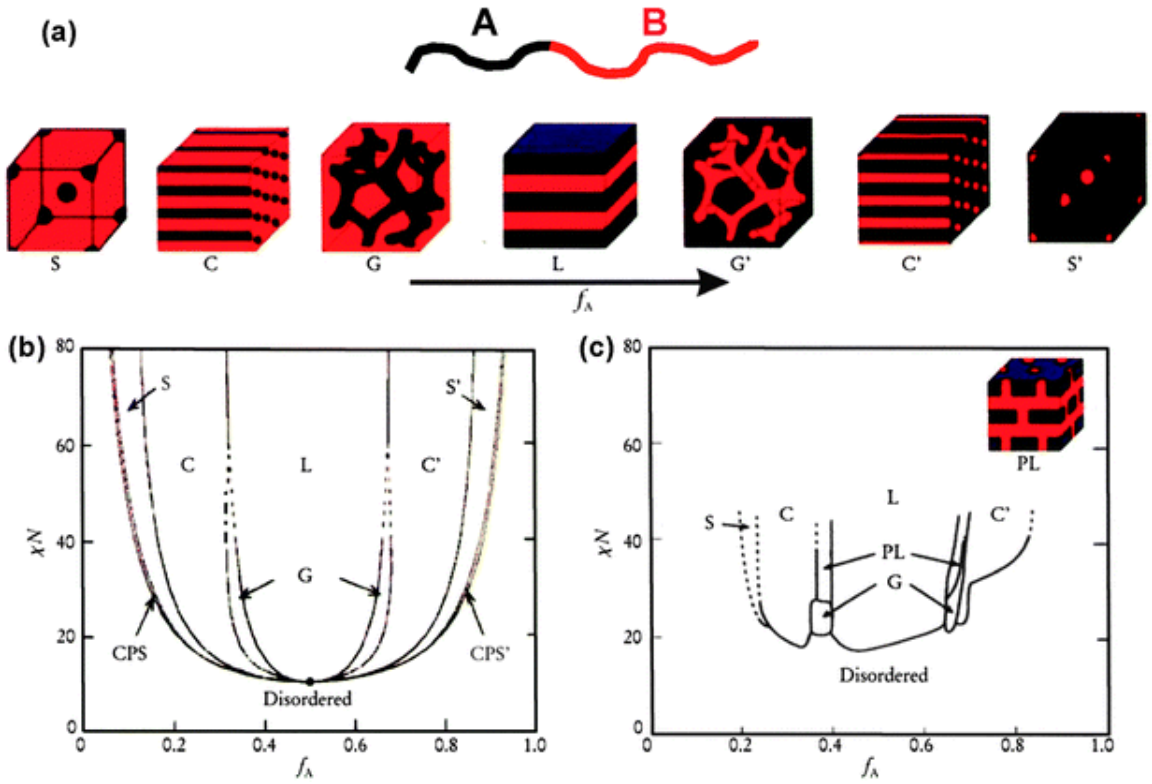

Figure 1.9 (a) Equilibrium morphologies of diblock copolymers as a function of the volume fraction of block A (f_A) (b) ideal and (c) experimental mean-field phase diagrams of PS-b-PIs showing the equilibrium morphology as a function of f_A and χN.[51]

Guiding patterns are required to impart long-range order in self-assembled films and ensure that domains are assembled perpendicularly to the surface of the substrate so as to be lithographically useful. A more detailed explanation of the role and means of manufacturing these guiding patterns is discussed in Chapter 5. DSA is an attractive alternative lithography technique chiefly due to the resemblance of two possible morphologies – hexagonally close-packed cylinders and lamellae – to traditional contact holes and line/space patterns used in semiconductor manufacturing respectively. Some notable advantages of DSA are that it offers a greatly simplified process flow by

eliminating the need for multiple patterning steps to achieve densely packed sub 20 nm domains, and that the pitch is naturally defined by the structure of the BCP. This means that guiding patterns can be written at relaxed pitches allowing for easy pitch multiplication.

1.5 References

1. Moore, G. E., Cramming more components onto integrated circuits, Reprinted from Electronics, volume 38, number 8, April 19, 1965, pp.114 ff. *IEEE Solid-State Circuits Society Newsletter* **2006,** *11* (3), 33-35.

2. IRDS, International Roadmap for Devices and Systems : Executive Summary. 2017.

3. IRDS, International Roadmap for Devices and Systems : Lithography. 2017.

4. Breaux, C. L. Investigation into obstacles to the implementation of the directed-self assembly of block copolymers. Dissertation, Georgia Institute of Technology, 2018.

5. Yoshio Nishi, R. D., Doering Doering, *Handbook of Semiconductor Manufacturing Technology, Second Edition / Edition 2*. REV ed.; Taylor & Francis: 2007.

6. Okazaki, S., Resolution limits of optical lithography. *Journal of Vacuum Science & Technology B: Microelectronics and Nanometer Structures Processing, Measurement, and Phenomena* **1991,** *9* (6), 2829-2833.

7. Manfrinato, V. R., Zhang, L., Su, D., Duan, H., Hobbs, R. G., Stach, E. A. and Berggren, K. K., Resolution Limits of Electron-Beam Lithography toward the Atomic Scale. *Nano Lett* **2013,** *13* (4), 1555-1558.

8. Mohammad, M. A., Muhammad, M., Dew, S. K. and Stepanova, M., Fundamentals of Electron Beam Exposure and Development. In *Nanofabrication: Techniques and Principles*, Stepanova, M. and Dew, S., Eds. Springer Vienna: Vienna, 2012; pp 11-41.

9. Groves, T. R., 3 - Electron beam lithography. In *Nanolithography*, Feldman, M., Ed. Woodhead Publishing: 2014; pp 80-115.

10. Ceglio, N. M., Hawryluk, A. M., Stearns, D. G., Gaines, D. P., Rosen, R. S. and Vernon, S. P., Soft x-ray projection lithography. *Journal of Vacuum Science & Technology B: Microelectronics Processing and Phenomena* **1990,** *8* (6), 1325-1328.

11. Tomie, T., *Tin laser-produced plasma as the light source for extreme ultraviolet lithography high-volume manufacturing: history, ideal plasma, present status, and prospects*. SPIE: 2012; Vol. 11, p 10.

12. Xiong, S., Bokor, J., Xiang, Q., Fisher, P., Dudley, I. M. and Rao, P., *Gate line edge roughness effects in 50-nm bulk MOSFET devices*. SPIE: 2002; Vol. 4689, p 9.

13. Lee, J.-Y., Shin, J., Kim, H.-W., Woo, S.-G., Cho, H.-K., Han, W.-S. and Moon, J.-T., *Effect of line-edge roughness (LER) and line-width roughness (LWR) on sub-100 nm device performance*. SPIE: 2004; Vol. 5376, p 8.

14. James D. Plummer, M. D., Peter D. Griffin, *Silicon VLSI Technology: Fundamentals, Practice, and Modeling*. 1 ed.; Pearson: 2001.

15. Gallatin, G. M., *Resist blur and line edge roughness*. SPIE: 2004; Vol. 5754, p 15.

16. Higgins, C. D., Szmanda, C. R., Antohe, A., Denbeaux, G., Georger, J. and Brainard, R. L., Resolution, Line-Edge Roughness, Sensitivity Tradeoff, and Quantum Yield of High Photo Acid Generator Resists for Extreme Ultraviolet Lithography. *Jpn J Appl Phys* **2011,** *50*, 036504.

17. Wallow, T., Higgins, C., Brainard, R., Petrillo, K., Montgomery, W., Koay, C.-S., Denbeaux, G., Wood, O. and Wei, Y., *Evaluation of EUV resist materials for use at the 32 nm half-pitch node*. SPIE: 2008; Vol. 6921, p 11.

18. Nagahara, S., Carcasi, M., Nakagawa, H., Buitrago, E., Yildirim, O., Shiraishi, G., Terashita, Y., Minekawa, Y., Yoshihara, K., Tomono, M., Mizoguchi, H., Estrella, J., Nagai, T., Naruoka, T., Dei, S., Hori, M., Oshima, A., Vockenhuber, M., Ekinci, Y., Meeuwissen, M., Verspaget, C., Hoefnagels, R., Rispens, G., Maas, R., Nakashima, H. and Tagawa, S., *Challenge toward breakage of RLS trade-off for EUV lithography by Photosensitized Chemically Amplified Resist (PSCAR) with flood exposure*. SPIE: 2016; Vol. 9776, p 18.

19. Shiraishi, H., Yoshimura, T., Sakamizu, T., Ueno, T. and Okazaki, S., Nanometer-Scale Imaging Characteristics of Novolak Resin-Based Chemical Amplification Negative Resist Systems and Molecular-Weight Distribution Effects of the Resin Matrix. *J Vac Sci Technol B* **1994,** *12* (6), 3895-3899.

20. Yoshimura, T., Shiraishi, H., Yamamoto, J. and Okazaki, S., Nano Edge Roughness in Polymer Resist Patterns. *Applied Physics Letters* **1993,** *63* (6), 764-766.

21. Yamaguchi, T., Namatsu, H., Nagase, M., Yamazaki, K. and Kurihara, K., Nanometer-scale linewidth fluctuations caused by polymer aggregates in resist films. *Applied Physics Letters* **1997,** *71* (16), 2388-2390.

22. Yoshiiwa, M., Kageyama, H., Shirota, Y., Wakaya, F., Gamo, K. and Takai, M., Novel class of low molecular-weight organic resists for nanometer lithography. *Applied Physics Letters* **1996,** *69* (17), 2605-2607.

23. Bratton, D., Ayothi, R., Felix, N., Cao, H., Deng, H. and Ober, C. K., *Molecular glass resists for next generation lithography*. SPIE: 2006; Vol. 6153, p 9.

24. Dai, J. Y., Chang, S. W., Hamad, A., Yang, D., Felix, N. and Ober, C. K., Molecular glass resists for high-resolution patterning. *Chem Mater* **2006,** *18* (15), 3404-3411.

25. Krysak, M., Silva, A. D., Sha, J., Lee, J.-K. and Ober, C. K., *Molecular glass resists for next-generation lithography*. SPIE: 2009; Vol. 7273, p 8.

26. De Silva, A., Felix, N. M. and Ober, C. K., Molecular Glass Resists as High-Resolution Patterning Materials. *Advanced Materials* **2008,** *20* (17), 3355-3361.

27. Drygiannakis, D., Patsis, G. P., Raptis, I., Niakoula, D., Vidali, V., Couladouros, E., Argitis, P. and Gogolides, E., Stochastic simulation studies of molecular resists. *Microelectron Eng* **2007,** *84* (5), 1062-1065.

28. Lawson, R. A. and Henderson, C. L., *Mesoscale kinetic Monte Carlo simulations of molecular resists: the effect of PAG homogeneity on resolution, LER, and sensitivity*. SPIE: 2009; Vol. 7273, p 10.

29. Lawson, R. A., Frommhold, A., Yang, D. X. and Robinson, A. P. G., Negative-tone organic molecular resists. *Front Nanosci* **2016,** *11*, 223-317.

30. Gibbons, F., Zaid, H. M., Manickam, M., Preece, J. A., Palmer, R. E. and Robinson, A. P. G., A chemically amplified fullerene-derivative molecular electron-beam resist. *Small* **2007,** *3* (12), 2076-2080.

31. Oizumi, H., Kumasaka, F., Tanaka, Y., Hirayama, T., Shiono, D., Hada, H., Onodera, J., Yamaguchi, A. and Nishiyama, I., Performance of molecular resist based on polyphenol in EUV lithography. *Microelectron Eng* **2006,** *83* (4), 1107-1110.

32. Li, L., Liu, X., Pal, S., Wang, S., Ober, C. K. and Giannelis, E. P., Extreme ultraviolet resist materials for sub-7 nm patterning. *Chemical Society Reviews* **2017,** *46* (16), 4855-4866.

33. Yeh, W.-M., Noga, D. E., Lawson, R. A., Tolbert, L. M. and Henderson, C. L., Comparison of positive tone versus negative tone resist pattern collapse behavior. *J Vac Sci Technol B* **2010,** *28* (6), C6S6-C6S11.

34. Yeh, W.-M. Pattern collapse in lithographic nanostructures: quantifying photoresist nanostructure behavior and novel methods for collapse mitigation. Dissertation, Georgia Institute of Technology, 2013.

35. Chini, S. F. and Amirfazli, A., Understanding Pattern Collapse in Photolithography Process Due to Capillary Forces. *Langmuir* **2010,** *26* (16), 13707-13714.

36. Noga, D. E., Lawson, R. A., Lee, C. T., Tolbert, L. M. and Henderson, C. L., Understanding Pattern Collapse in High-Resolution Lithography: Impact of Feature Width

on Critical Stress. *Advances in Resist Materials and Processing Technology Xxvi* **2009,** *7273*.

37. Namatsu, H., Kurihara, K., Nagase, M., Iwadate, K. and Murase, K., Dimensional limitations of silicon nanolines resulting from pattern distortion due to surface tension of rinse water. *Applied Physics Letters* **1995,** *66* (20), 2655-2657.

38. Noga, D. E., Yeh, W. M., Lawson, R. A., Tolbert, L. M. and Henderson, C. L., The Use of Surface Modifiers to Mitigate Pattern Collapse in Thin Film Lithography. *P Soc Photo-Opt Ins* **2010,** *7639*.

39. Brakensiek, N. L., Zhang, P., King, D. and Ghelli, C., *Advanced rinse process alternatives for reduction of photolithography development cycle defects*. SPIE: 2005; Vol. 5753, p 11.

40. Hoggan, E. N., Ke, W., Flowers, D., DeSimone, J. M. and Carbonell, R. G., "Dry" lithography using liquid and supercritical carbon dioxide based chemistries and processes. *IEEE Transactions on Semiconductor Manufacturing* **2004,** *17* (4), 510-516.

41. Zhang, X., Pham, J. Q., Ryza, N., Green, P. F. and Johnston, K. P., Chemical-mechanical photoresist drying in supercritical carbon dioxide with hydrocarbon surfactants. *Journal of Vacuum Science & Technology B: Microelectronics and Nanometer Structures Processing, Measurement, and Phenomena* **2004,** *22* (2), 818-825.

42. Goldfarb, D. L., Bruce, R. L., Bucchignano, J. J., Klaus, D. P., Guillorn, M. A. and Wu, C. J., *Pattern collapse mitigation strategies for EUV lithography*. SPIE: 2012; Vol. 8322, p 13.

43. Sakamoto, R., Sakaida, Y. and Ho, B.-C., *Dry development rinse process (DDRP) and material (DDRM) for novel pattern collapse free process*. SPIE: 2013; Vol. 8682, p 8.

44. Yeh, W. M., Noga, D. E., Lawson, R. A., Tolbert, L. M. and Henderson, C. L., Comparison of positive tone versus negative tone resist pattern collapse bahavior*. *J Vac Sci Technol B* **2010,** *28* (6), C6s6-C6s11.

45. Yeh, W.-M., Noga, D. E., Lawson, R. A., Tolbert, L. M. and Henderson, C. L., *Thin film buckling as a method to explore the effect of reactive rinse treatments on the mechanical properties of resist thin films*. SPIE: 2010; Vol. 7639, p 6.

46. Lawson, R. A., Lee, C. T., Tolbert, L. M., Younkin, T. R. and Henderson, C. L., High resolution negative tone molecular resist based on di-functional epoxide polymerization. *Microelectron Eng* **2009,** *86* (4-6), 734-737.

47. Tandon, U. S., An overview of ion beam lithography for nanofabrication. *Vacuum* **1992,** *43* (3), 241-251.

48. Garcia, R., Knoll, A. W. and Riedo, E., Advanced scanning probe lithography. *Nature Nanotechnology* **2014,** *9*, 577.

49. Barcelo, S. and Li, Z., Nanoimprint lithography for nanodevice fabrication. *Nano convergence* **2016,** *3* (1), 21-21.

50. Jeong, S.-J., Kim, J. Y., Kim, B. H., Moon, H.-S. and Kim, S. O., Directed self-assembly of block copolymers for next generation nanolithography. *Materials Today* **2013,** *16* (12), 468-476.

51. Mai, Y. and Eisenberg, A., Self-assembly of block copolymers. *Chemical Society Reviews* **2012,** *41* (18), 5969-5985.

52. Flory, P. J., Thermodynamics of High Polymer Solutions. *The Journal of Chemical Physics* **1942,** *10* (1), 51-61.

CHAPTER 2. CROSS-LINKABLE PHOTOACID GENERATORS FOR ULTRA-HIGH LOADING IN EPOXIDE FUNCTIONALIZED RESISTS

2.1 Introduction

Chemically amplified resists (CARs) are popular materials in the semiconductor manufacturing industry, but a CAR has yet to be developed which can simultaneously meet the resolution, line edge roughness (LER), and sensitivity requirements necessary for use in next-generation lithography technologies such as extreme ultraviolet (EUV) and electron-beam (e-beam) lithography. This inability to simultaneously meet all of these requirements is referred to as the RLS trade-off and has proved to be a fundamental limitation to CARs.[1, 2] Each of these requirements are intrinsically tied to the processes in which photoacids are generated and initiate reactions. The amount and distribution of PAG in the resist affects both the statistical probability that a photoacid is generated upon exposure (sensitivity) as well as the spatial distribution of de-protection in exposed regions (which affects LER). Ideally, sensitivity and LER could both be improved by simply increasing the amount of PAG in the resist, but in traditional blended polymeric CARs this has typically led to resolution loss due to photoacids diffusing into nominally unexposed regions, and an increase in LER due to microphase separation between the polymer and the PAG as well as inhomogeneity throughout the resist film.[3] One design strategy used to overcome these problems has been to covalently bind PAGs to the polymer chain in order to restrict photoacid diffusion lengths and improve homogeneity of acid distribution (enabling higher possible PAG loadings).[4-6] These materials demonstrated significantly

improved resolution, however they still suffer from problems intrinsic to polymeric resists at small size scales such as pattern collapse during wet development and a large LER due to the large size of the polymers relative to the desired feature size.

An alternative CAR design strategy of interest are molecular glass resists (low molecular-weight organic compounds capable of forming stable amorphous glasses) particularly those based on cationic epoxide polymerization[7, 8] Patterned features in these resists are covalently cross-linked networks and demonstrate superior resistance to pattern collapse (a greatly desired property at increasingly smaller feature sizes).[9] In traditional CARs, photoacids are generated in exposed regions, de-protect solubility-switching groups, and are subsequently re-generated. In epoxide resists however, the lifetime of the PAG is greatly reduced because once it initiates polymerization it is not regenerated (Figure 2.1 a) without the presence of a chain-transfer group such as an alcohol (Figure 2.1 c). Instead, the active site becomes the end of the growing polymer chain which is diffusion controlled as polymerization continues.[10-12] It should therefore theoretically be possible to use much higher PAG loadings in these resists and obtain the desired improvements in sensitivity and LER while (1) ensuring the homogeneity of the resist and (2) without significant resolution loss from photo-acid diffusion.

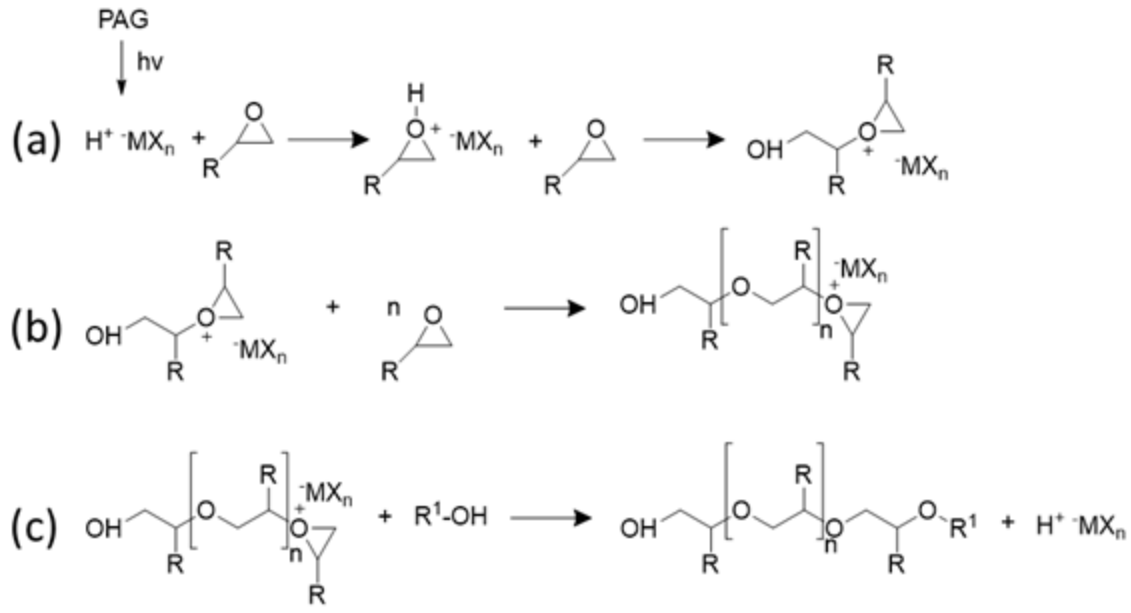

Figure 2.1 Overview of the potential polymerization mechanisms of epoxide containing resists starting with initiation (a) and followed by either epoxide-epoxide cross-linking (b) or epoxide-phenol cross-linking (c).

Initial studies showed that using higher PAG loadings actually had a negative effect on sensitivity (Figure 2.2) and LER (Figure 2.3) when using a model epoxide resist (4-Ep Figure 2.4) and a common onium salt PAG (TPS-SbF_6 Figure 2.4) . Similar results were observed when using a combination of additives, a PAG and a photo-decomposable nucleophile, where total additive loading beyond 30 mol. % decreased patterning performance.[13]

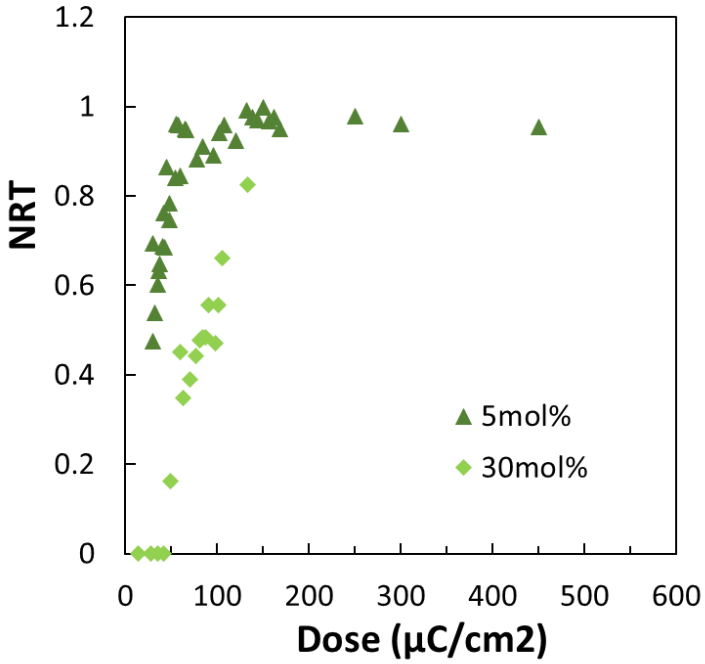

Figure 2.2 Contrast curves collected with 100 keV e-beam lithography using 4-Ep as the resists and either 5 or 30 mol. % TPS-SbF_6 as the PAG.

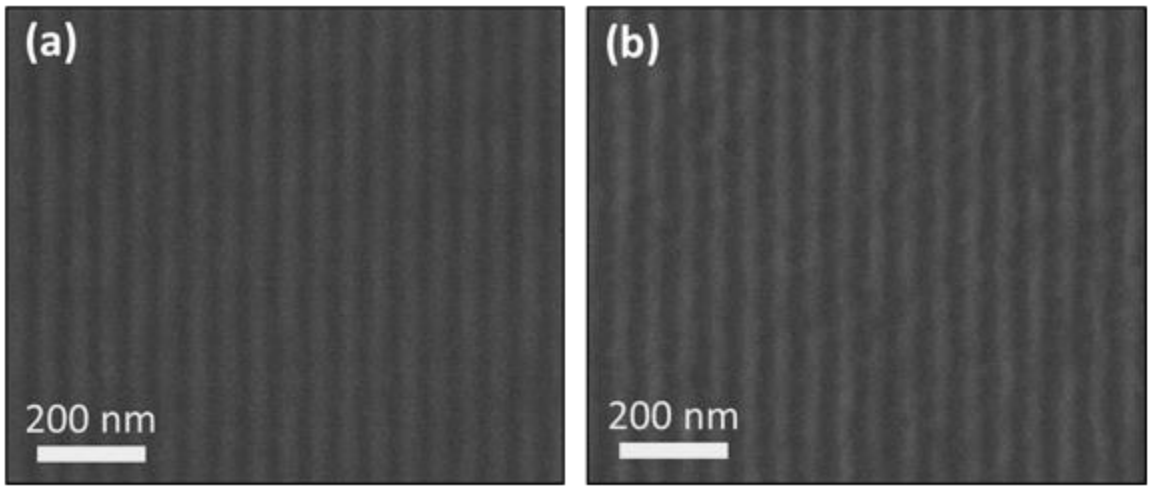

Figure 2.3 Line-space arrays patterned at 50 µC/cm2 using 100 keV e-beam lithography, with 4-Ep as the base resist and TPS-SbF6 as the PAG at 5 mol% (a) and 30 mol% (b).

The most likely cause of this behavior is that since these additives are not incorporated into the polymer network, they act as network diluents and reduce the cross-link density,

thereby degrading pattern quality at high loadings. Functionalizing additives with groups that can participate in epoxide cross-linking should therefore enable higher PAG/PDN loading and simultaneously improve resolution, LER, and sensitivity without inhibiting the resists' ability to form densely cross-linked features. The first generation of materials synthesized (Figure 2.4) were designed to be structurally analogous to the onium salt PAG TPS-SbF6 and were functionalized with groups that could participate in either epoxide-epoxide cross-linking (Figure 2.1 b) or epoxide-phenol cross-linking (Figure 2.1 c).

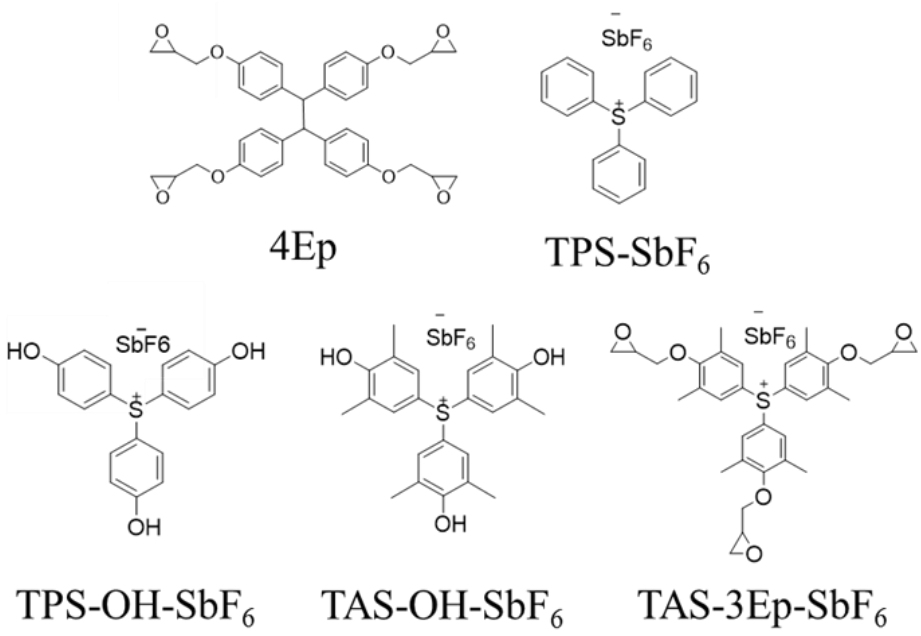

Figure 2.4 Chemical structure of the resist material (4-Ep) and PAGs used in this study (TPS-SbF6, TPS-OH-SbF6, TAS-OH-SbF6, TAS-3Ep-SbF6).

2.2 Experimental

2.2.1 Materials and Methods

All synthesis was performed in a laboratory equipped with UV-filters in order to prevent accidental exposure of the PAGs during synthesis and handling. Separate 4 wt%

solutions of 4-Ep, TAS-OH-SbF_6, TPS-OH-SbF_6, and TAS-3Ep-SbF_6 were prepared in ethyl lactate. A series of solutions at varying mol % PAG were then prepared by combining 4-Ep solution with the necessary amounts of PAG solution. Solutions were spin-coated at 2000 rpm onto silicon wafer pieces (wafers were ordered from University Wafer and cleaned with O_2 plasma for 5 min. immediately prior to use). Silicon wafers used for TAS-3Ep-SbF_6 blending studies were dehydrated by baking at 200 °C for 2 minutes prior to spin coating. All resists were processed with a post-apply bake (PAB) at 90 °C for 2 minutes to remove residual casting solvent and a 1-minute post-exposure bake (PEB) of 60 °C or 90 °C for cross-linking studies and 90 °C PEB for e-beam and DUV contrast curves.

Exposed films were developed in MIBK for 30 seconds followed by a 10 second IPA rinse. E-beam patterning was obtained using a JEOL JBX-9300FS electron-beam lithography system with a 100-keV acceleration voltage and a 2-nA current. DUV contrast curves were obtained using an Oriel Instruments 500W Hg-Xe arc lamp with a 248 nm bandpass filter as the light source and a M-2000 Woolam Ellipsometer to measure film thicknesses. E-beam contrast curves were obtained by exposing 50 x 50 μm squares at a variety of doses and measuring the remaining height following development with a Tencor KLA P15 Profilometer. UV-Visible spectra were collected with a Cary 5000 ultraviolet to near infrared spectrometer. Exposed wafers were imaged using a Carl Zeiss Ultra 60 scanning electron microscope (SEM) with 2 keV acceleration voltage.

2.2.2 Synthesis of TPS-OH-Cl

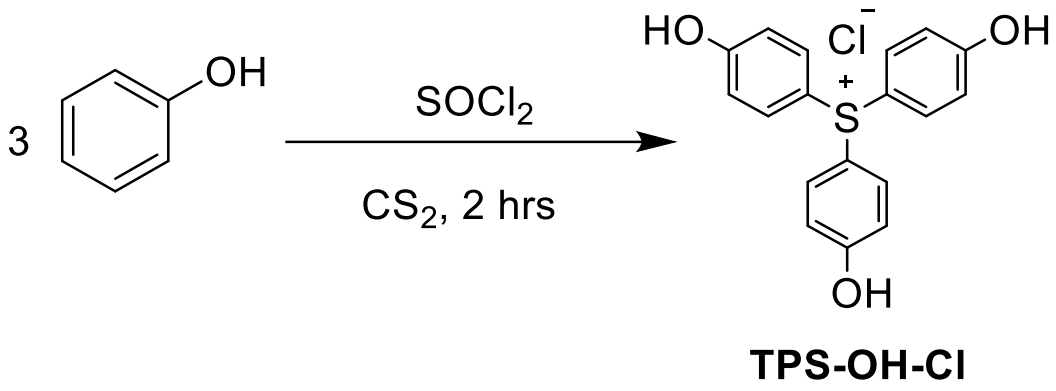

Figure 2.5 Synthetic scheme for TPS-OH-Cl.

Tris(4-hydroxyphenyl)sulfonium chloride (TPS-OH-Cl) was synthesized using a modified procedure described by Crivello and Lam.[14] Phenol (5.79 g, 66.52 mmol, 3.0 equiv.) and aluminum chloride ($AlCl_3$, 5.48 g, 44.10 mmol, 2.0 equiv.) were dissolved in 17.5 mL cold carbon disulfide (CS_2) in a 100 mL round bottom flask, which was then placed into an ice bath. Thionyl chloride ($SOCl_2$, 2.7 g, 22.6 mmol, 1 equiv.) was added dropwise over 45 minutes. The mixture was sealed with a needle-vented rubber septum and stirred for 2 hours, after which a solution of 4 mL HCl in 60 mL DI water was added to quench the reaction. The resulting solution was filtered to isolate the crude product, which was triturated twice in a 50/50 ethanol/ether mixture and dried overnight in a vacuum oven to give the product (TPS-OH-Cl), a light pink powder. ^{1}H NMR (300 MHz DMSO) δ (ppm): 7.52 (d, J = 9.0, 6H), 7.04 (d, J = 9.0, 6H). ESI-MS *m/z*: M^+ 311.0 (100.0%), 312.0 (19.5%), 313.0 (4.5%). Anal. Calcd for $C_{18}H_{15}O_3S^+Cl^-$: C, 62.34; H, 4.36; S, 9.24. Found: C, 62.40; H, 4.61; S, 9.02. Yield: 82 %.

2.2.3 Synthesis of TPS-OH-SbF6

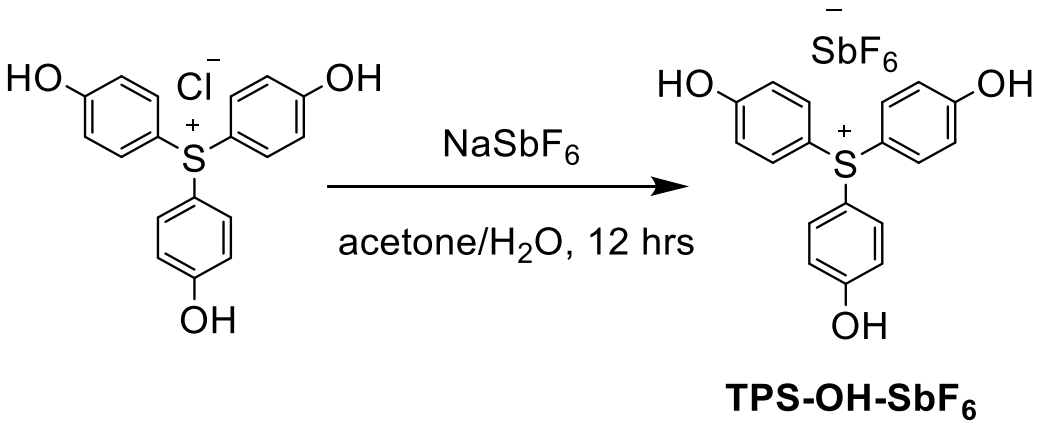

Figure 2.6 Synthetic scheme for TPS-OH-SbF_6.

TPS-OH-Cl (1.00 g, 2.88 mmol, 1 equiv.) and sodium hexafluoroantimonate (0.67 g, 2.88 mmol, 1 equiv.) were added to a vial containing 8 mL acetone and 2 mL water. The vial was capped and the solution was stirred vigorously overnight at room temperature. Precipitated solids were then filtered out of solution, re-dissolved in ethyl acetate, and washed three times with distilled water to remove any remaining sodium salts. The combined organic layers were dried over $MgSO_4$ and excess solvent was removed using rotary evaporation to give the product tris(4-hydroxyphenyl)sulfonium hexafluoroantimonate (TPS-OH-SbF_6), a viscous liquid. ^{1}H NMR (300 MHz DMSO) δ (ppm): 7.53 (d, J = 8.7, 6H), 7.05 (d, J = 8.7, 6H). ESI-MS *m/z*: M^+ 311.0 (100.0%), 312.0 (19.5%), 313.0 (4.5%) M^- 234.7.0 (100.0%) 236.90 (74.8%). Anal. Calcd for $C_{18}H_{15}O_3S^+SbF_6^-$: C, 39.52; H, 3.12; S, 5.84. Found: C, 40.19; H, 3.43; S, 5.30. Yield: 55 %.

2.2.4 Synthesis of TAS-OH-Cl

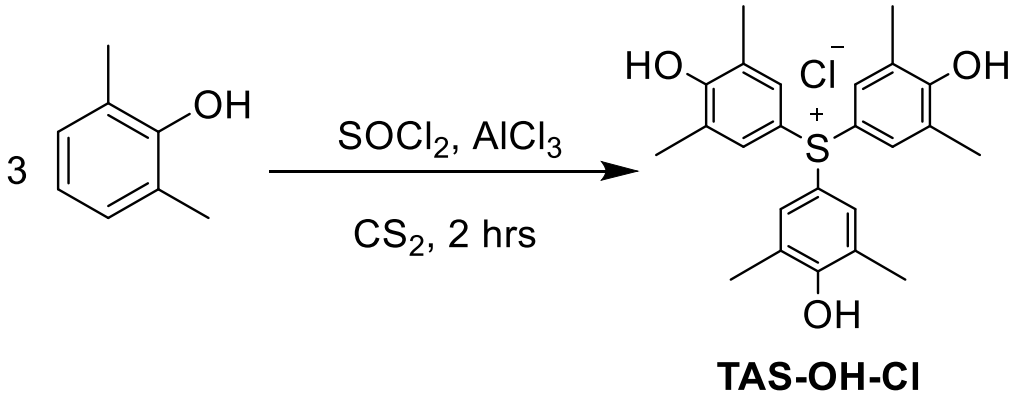

Figure 2.7 Synthetic scheme for TAS-OH-Cl.

2,6-dimethylphenol (15.0 g, 122.8 mmol, 3.0 equiv.) was dissolved in 35 mL of cold CS_2 in a 250 mL round bottom flask and placed into an ice bath. $AlCl_3$ (10.9 g, 81.9 mmol, 2 equiv.) was added to the reaction mixture, turning it a dark green color. Thionyl chloride (2.98 mL, 40.9 mmol, 1.0 equiv.) was added dropwise over 45 minutes, after which the reaction was sealed with a needle-vented rubber septum and stirred for 2 hours until a purple solid had formed. A solution of 8 mL HCl in 120 mL DI water was added to terminate the reaction, and the solution was filtered to isolate the crude product (a lumpy yellow-pink solid). The crude product was recrystallized twice from a 50/50 ethanol/ether mixture and dried overnight in a vacuum oven to give the product tris(4-hydroxy-3,5-dimethylphenyl)sulfonium chloride (TAS-OH-Cl), a white powder. MP: 248-250 (Li.t. 250-252). ^{1}H NMR (300 MHz DMSO-d6) δ (ppm): 7.35 (s, 6H), 2.19 (s, 18H). ESI-MS *m/z*: M^+ 395.4 (100.0%), 396.4 (26.0%), 397.4 (4.5%). Anal. Calcd for $C_{24}H_{27}O_3S^+Cl^-$: C, 66.88; H, 6.31; S, 7.44. Found: C, 64.39; H, 6.50; S, 7.04. Yield: 70 %.

2.2.5 Synthesis of TAS-OH-SbF_6

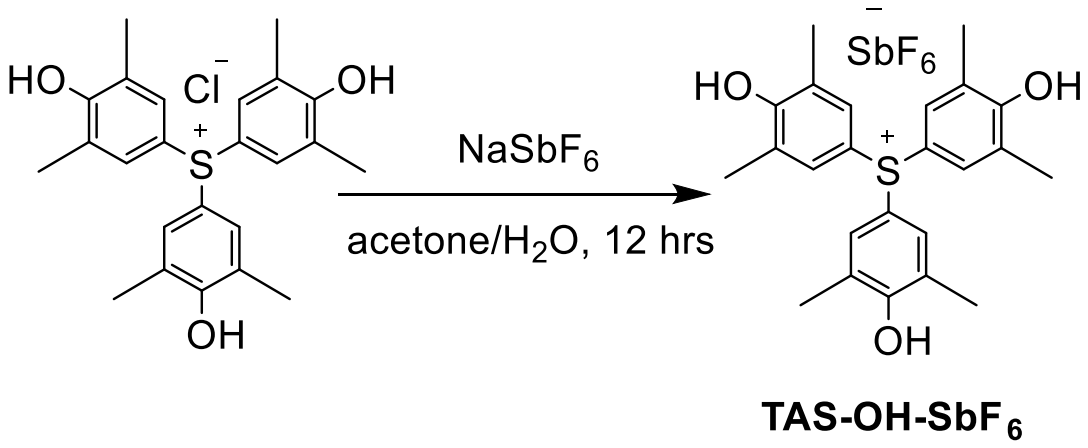

Figure 2.8 Synthetic scheme for TAS-OH-SbF_6.

TAS-OH-Cl (0.5 g, 1.2 mmol, 1.0 equiv.) and sodium hexafluoroantimonate (0.28 g, 1.2 mmol, 1 equiv.) were added to a vial containing 7 mL acetone and 0.5 mL water. The vial was capped, and the solution was stirred vigorously overnight at room temperature. Precipitated solids were then filtered out of solution, re-dissolved in ethyl acetate, and washed three times with DI water to remove any remaining sodium salts. The combined organic layers were dried over $MgSO_4$ and excess solvent was removed using rotary evaporation to give the product tris(4-hydroxy-3,5-dimethylphenyl)sulfonium hexafluoroantimonate (TAS-OH-SbF_6), a white powder, which was dried overnight in a vacuum oven. ^{1}H NMR (300 MHz DMSO-d6) δ (ppm): 7.35 (s, 6H), 2.18 (s, 18H). ESI-MS *m/z*: M^+ 395.4 (100.0%), 396.4 (26.0%), 397.4 (4.5%) M^- 234.8 (100.0%), 236.8 (74.8%). Anal. Calcd for $C_{24}H_{27}O_3S^+SbF_6^-$: C, 45.66; H, 4.31; S, 5.08. Found: C, 47.43; H, 4.85; S, 4.73. Yield: 31 %.

2.2.6 Synthesis of TAS-3Ep-I

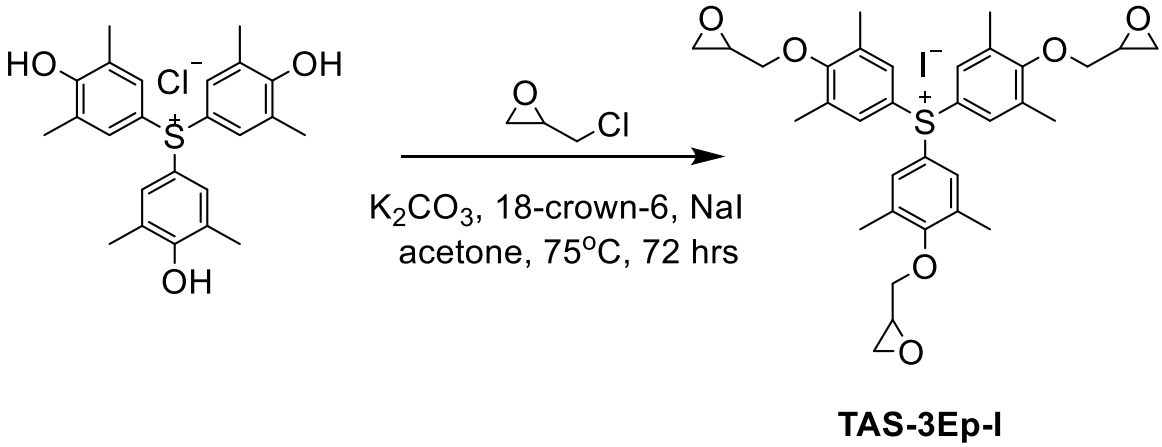

Figure 2.9 Synthetic scheme for TAS-3Ep-I.

TAS-OH-Cl (1.5 g, 3.5 mmol, 1 equiv.), sodium iodide (0.6 g, 4.0 mmol, 1.1 equiv.), K_2CO_3 (1.8 g, 13.2 mmol, 3.8 equiv.), and a catalytic amount of 18-crown-6 (0.05 g, 0.2 mmol) were added to 30 mL acetone in a round bottom flask. Epichlorohydrin (2.5 mL, 30.6 mmol) was added drop wise and the reaction was refluxed at 70 °C for 3 days. The reaction was cooled to room temperature, and 15 mL each of DCM and DI water were added while stirring. The product was extracted twice with DCM and the combined organic layers were washed three times with DI water. The organic layer was dried over $MgSO_4$ and solvent was removed using a rotary evaporator to yield crude tris(3,5-dimethyl-4-(oxiran-2-ylmethoxy)phenyl)sulfonium iodide (TAS-3Ep-I), a dark yellow viscous liquid. TAS-3Ep-I was purified using silica gel column chromatography and a 95:5 mixture of DCM:MeOH. The presence of the iodide anion was confirmed with negative ion ESI-MS and with a silver nitrate precipitation test. ^{1}H NMR (300 MHz Acetone-d_6) δ (ppm): 7.62 (s, 6H), 4.37 (dd, J = 11.4, 3H), 3.77 (dd, J = 11.1, 3H), 3.38 (m, 3H), 2.84 (dd, J = 5.1, 3H), 2.68 (dd, J = 5.1, 3H), 2.36 (s, 18H). ESI-MS *m/z*: M^+ 563.5 (100.0%), 564.4 (35.7%), 565.4 (4.5%) M^- 126.6 (100.0%). Yield: 44 %.

2.2.7 *Synthesis of TAS-3Ep-SbF_6*

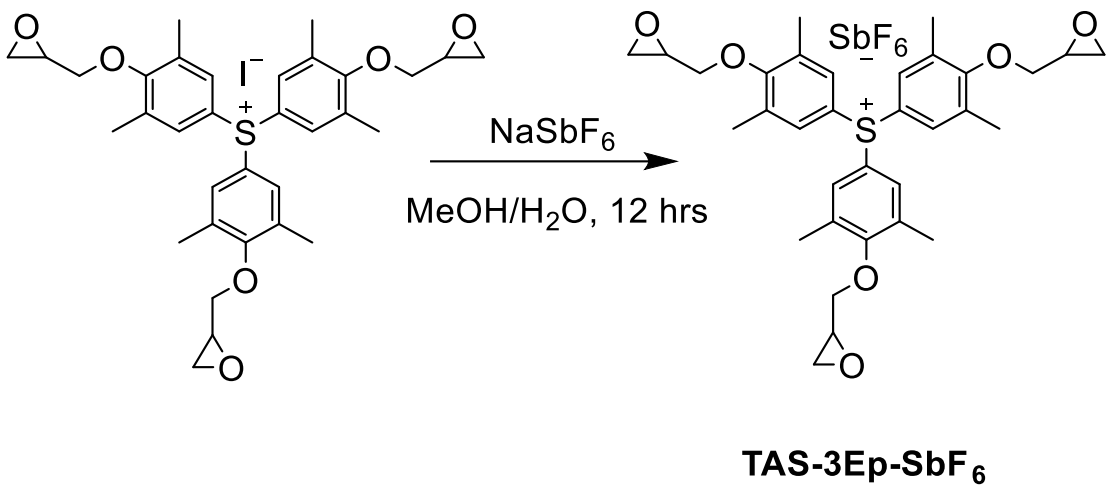

Figure 2.10 Synthetic scheme for TAS-3Ep-SbF_6.

TAS-3Ep-I (0.04 g, 0.06 mmol, 1 equiv.) and sodium hexafluoroantimonate (0.67 g, 2.88 mmol, 1 equiv.) were added to a vial containing 0.4 mL methanol and 0.4 mL water. The vial was capped and the solution was stirred vigorously overnight at room temperature. Precipitated solids were then filtered out of solution, re-dissolved in ethyl acetate, and washed three times with distilled water to remove any remaining sodium salts. The combined organic layers were dried over $MgSO_4$ and excess solvent was removed using rotary evaporation to give the product tris(3,5-dimethyl-4-(oxiran-2-ylmethoxy)phenyl)sulfonium hexafluoroantimonate (TAS-3Ep-SbF_6). The presence of the correct hexafluoroantimonate anion was confirmed using ESI-MS. ^{1}H NMR (300 MHz CD_2Cl_2) δ (ppm): 7.20 (s, 6H), 4.29 (dd, J = 11.4, 3H), 3.72 (dd, J = 11.3, 3H), 3.37 (m, 3H), 2.89 (dd, J = 4.5, 3H), 2.69 (dd, J = 4.8, 3H), 2.37 (s, 18H). ESI-MS *m/z*: M^+ 563.5 (100.0%), 564.5 (35.7%), 565.4 (4.5%) M^- 234.8 (100.0%), 236.8 (74.8%). Yield: 23 %.

2.3 Results and Discussion

2.3.1 Effect of PAG Loading on the Extent of Cross-linking

Previous work has shown that the extent of cross-linking/conversion in epoxide resists is linearly related to the normalized remaining film thickness (NRT) in a dose-response curve.[15] Therefore, the maximum or "plateau" NRT of dose-response curves of 4-Ep with different amounts of PAG can be compared to determine the relative extent of cross-linking as a function of mol. % PAG. Plotting this and comparing the curves collected using different PAGs allowed for an examination of the effect that the different PAGs have on the extent of cross-linking of 4-Ep and whether or not the PAG is incorporated into the network or acting as a network diluent.

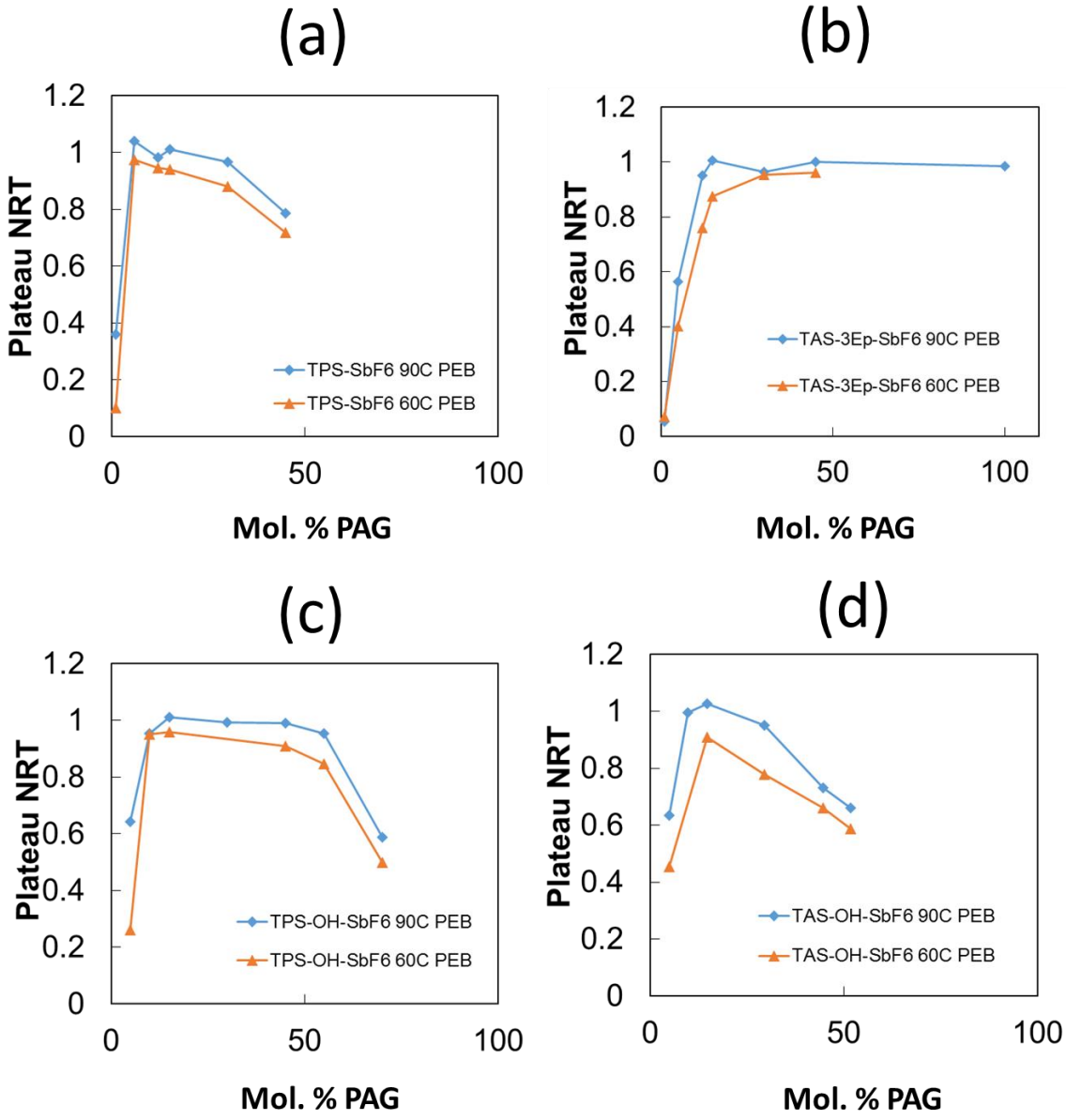

Figure 2.11 Cross-linking studies from DUV exposures of blends of 4-Ep with (a) TPS-SbF_6, (b) TAS-3Ep-SbF_6, (c) TPS-OH-SbF_6, and (d) TAS-OH-SbF_6 coated on silicon and developed with MIBK using either a 90 °C or 60 °C PEB.

The first studies collected were with the original unfunctionalized PAG TPS-SbF_6 (Figure 2.11 a) and showed a decrease in plateau NRT once PAG loading exceeded approximately 10 mol. %. This suggests that as theorized, additives that are not

incorporated into the network act as a diluent above a certain loading and hinder the ability of the resist to form a highly cross-linked network. This is undesirable as it not only decreases the thickness of a photoresist following development but may also reduce its mechanical strength, resistance to pattern collapse, and could potentially result in solvent swelling. Blends containing epoxide-functionalized TAS-3Ep-SbF_6 did not show a decrease in the plateau NRT at any PAG loading studied (Figure 2.11 b) which is to be expected as TAS-3Ep-SbF_6 can cross-link with itself as well as the base resist, 4-Ep. This suggests that TAS-3Ep-SbF_6 can be used at extremely high loadings, even up to 100 mol. % where it would act as a single component resist.

In blends containing TPS-OH-SbF_6, the extent of cross-linking doesn't noticeably decrease until the PAG loading exceeds 50 mol. % (Figure 2.11 c). This is not a surprising result since there is no phenol:phenol cross-linking mechanism and once the phenol:epoxide ratio exceeds 1:1, any additional phenol-functionalized PAG will only act as a diluent. Despite small structural differences, TAS-OH-SbF_6 showed cross-linking behaviour that was very different than that of TPS-OH-SbF_6 (Figure 2.11 d). NRT in blends using TAS-OH-SbF_6 began to decrease after approximately 20 mol. % PAG loading, which was only slightly higher than when using the totally un-crosslinkable TPS-SbF_6. Since the glass transition temperature (T_g) of the resist should influence the rate/extent of cross-linking due to its effect on the mobility of active chain-ends during cross-linking, it was initially thought that the differences in behaviour between the two phenol-functionalized PAGs might have been caused by differences in their T_g values, especially as additive loading approached 50 % of the total resist makeup.[12, 13] This seemed to be supported by values measured using Modulated Differential Scanning Calorimetry (MDSC) (Table 1)

which showed that TAS-OH-SbF_6 had a significantly greater T_g than that of TPS-OH-SbF_6 and 4-Ep while TPS-OH-SbF_6 had a much lower T_g than both. However, it was shown that using 50 mol. % of a phenol-functional PAG in 4-Ep only had a moderate effect (6 °C) on the T_g of the resist so this is unlikely to be the major contributing source of the large deviation in cross-linking behaviour between the two.

Table 1. T_g values of some of the resist (4-Ep) and the two phenol-functionalized PAGs used in this study (measured using MDSC).

Compound	Tg (°C)
4-Ep	48
TAS-OH-SbF_6	68
TPS-OH-SbF_6	-15

This deviation in cross-linking behaviour can most likely be attributed to the major structural difference between the two molecules; the two methyl groups adjacent to the phenol group on TAS-3Ep-SbF_6 (Figure 2.12). These groups are likely sterically hindering the hydroxyl reaction site and as a result TAS-OH-SbF_6 is not able to efficiently cross-link into the network. This would explain the decrease in the plateau NRT of 4-Ep as a function of total loading as it is acting as a network diluent in a similar fashion to the totally un-functionalized TPS-SbF_6. This explanation is further supported by research conducted by Gibson et al. who reported that the presence of a single methyl group ortho to a hydroxyl group on cresol reduced the rate of reaction between it and an epoxy resin.[16] Due to its inability to efficiently cross-link with 4-Ep, TAS-OH-SbF_6 was not investigated further.

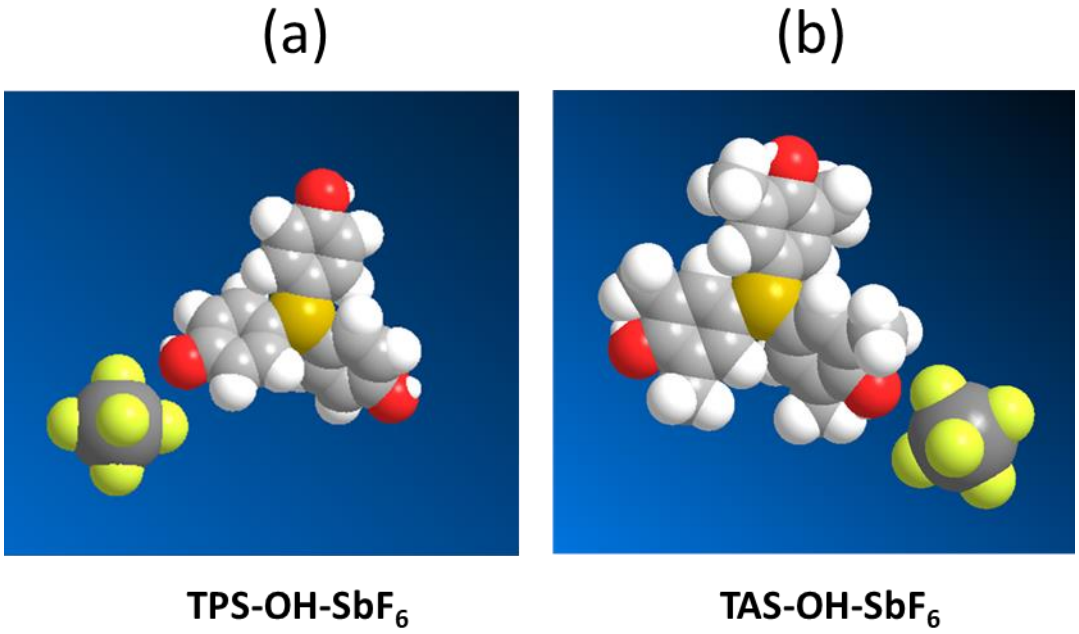

Figure 2.12 Space-filling models of (a) TPS-OH-SbF_6 and (b) TAS-OH-SbF_6 (generated using ChemDraw 3D).

2.3.2 UV-Vis Spectroscopy

UV-Vis absorption spectra were obtained using solutions of TAS-SbF_6, TPS-OH-SbF_6, and TAS-OH-SbF_6 in ethanol (Figure 2.13). The λ_{max} of the phenol functionalized TPS-OH-SbF_6 was largely unchanged from un-functionalized TAS-SbF_6 (from 266 to 261 nm), but the methyl functionalization onto the aromatic ring blueshifts the λ_{max} of TAS-OH-SbF_6 to 235 nm. This indicates that the phenol functionalization of TAS-SbF_6 should not dramatically impact its sensitivity using DUV (298 nm) light.

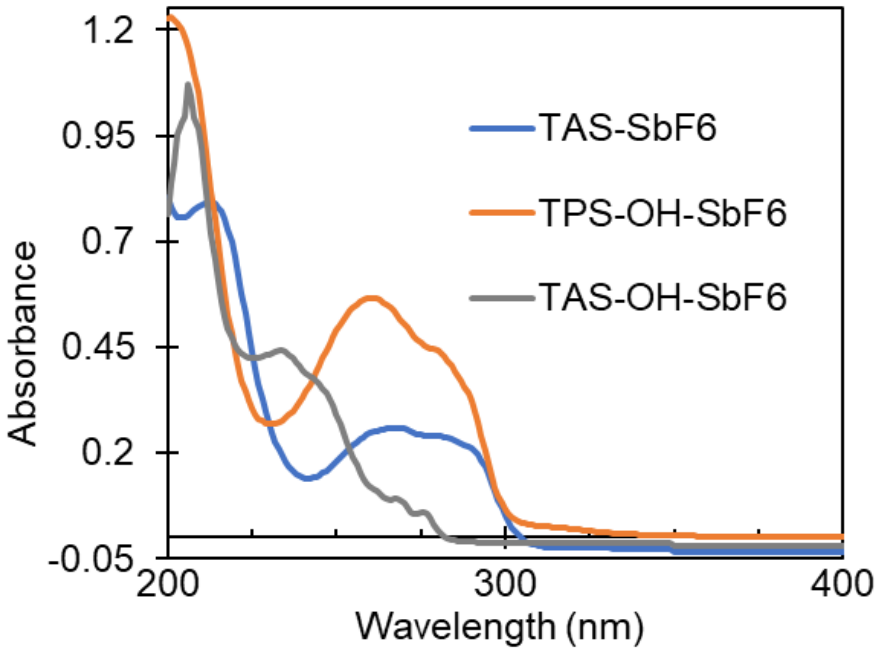

Figure 2.13 UV-Vis Absorption Spectra of PAGs in ethanol.

2.3.3 Ultra-High Loading of Cross-linkable PAGs

Once it was established (using the previously discussed results) that two PAGs (TAS-3Ep-SbF_6 and TPS-OH-SbF_6) had been synthesized which would not reduce the extent of cross-linking in 4-Ep at high loadings (generally speaking PAG loading would be considered to be high at or above 15 mol. %), the effect of using these PAGs at high loadings was investigated. As discussed previously, it was expected that higher PAG loadings would improve sensitivity and LER.

TPS-3Ep-SbF_6

Contrast curves were collected using DUV (Figure 2.14) and 100 keV e-beam (Figure 2.15) as exposure sources. Under DUV when the amount of PAG was increased from 45 mol. % to 100 mol. % E_{100} was shifted from approximately 20 mJ/cm^2 to 9 mJ/cm^2.

This behavior was expected as more PAG would typically result in more photoacids and crosslinking events being generated, leading to a higher extent of crosslinking at lower doses. Dose-response curves collected with e-beam lithography however showed the opposite behavior presenting an E_{100} of 112 μC/cm^2 at 55 mol. % and 309 μC/cm^2 at 100 mol. % PAG.

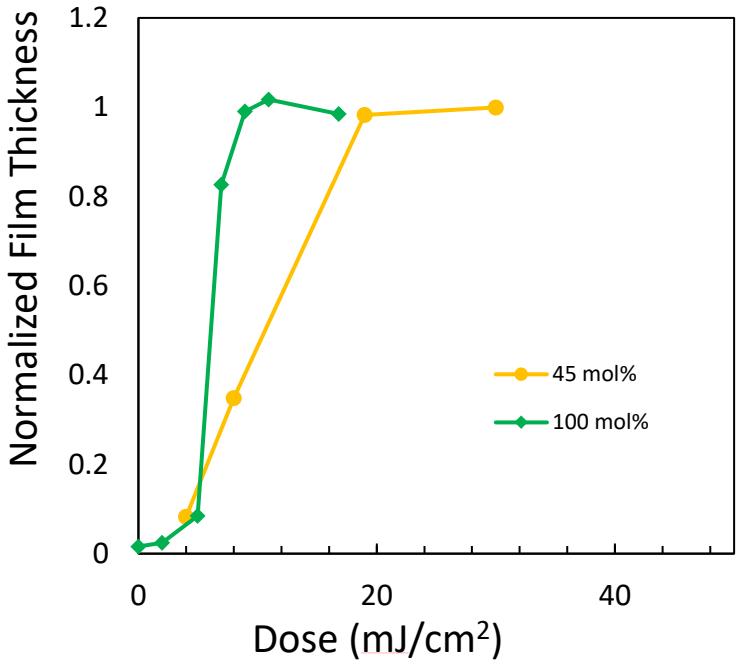

Figure 2.14 DUV contrast curves of 4-Ep containing TAS-3Ep-SbF_6 at 45 mol. % and 100 mol. %.

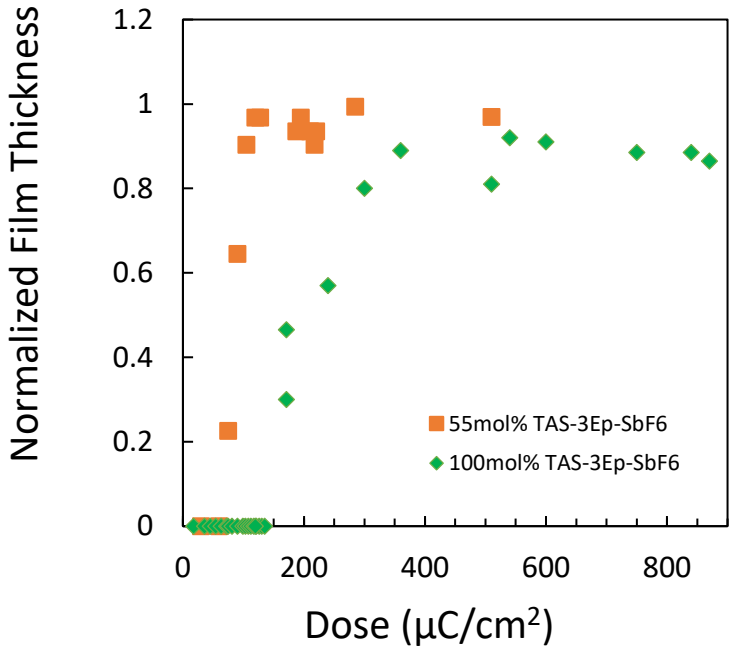

Figure 2.15 100 keV e-beam lithography contrast curves of 4-Ep containing TAS-3Ep-SbF_6 at 55 mol. % and 100 mol. %.

This is surprising behaviour as typically sensitivity is increased or saturated with additional PAG loading, not decreased.[17-20] Also surprising is that the sensitivity/loading relationship differs than that observed under a low energy exposure source (DUV). One possibility is that by increasing the amount of antimony and fluorine in the resist, the electron absorption cross-section is increased thereby decreasing the effective electron penetration depth and requiring higher doses to ensure that cross-linking can diffuse to the substrate.[21, 22] This is unlikely to be the case however, as EBL electrons are highly energetic (100 eV) and research by Onodera et al. demonstrated that acid concentration by depth in fluorinated polymer films did not vary greatly until film thicknesses exceeded 100 nm, well above the 40 nm thick films used in this study.[23] Another possibility is that the sensitivity is being affected by shifting the average degree of functionality of the resist from 4 (4-Ep)

to 3 (TPS-3Ep-SbF_6)[15] or shifting the T_g[12, 24] of the resists with the increasing amount of TPS-3Ep-SbF_6. While it is certainly possible that these are affecting the sensitivity to some degree, they should be equally influencing the DUV dose-response curves and do not explain the divergence in behaviour between the two exposure sources. It is most likely that the change in sensitivity is due to the change in photoacid generation method between the two exposure sources. Under DUV, photoacids are generated via the direct excitation of the PAG by a photon (Figure 2.16).

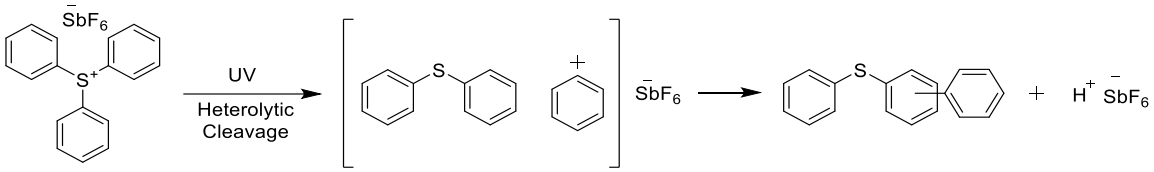

Figure 2.16 DUV acid generation mechanism of TPS-SbF_6.

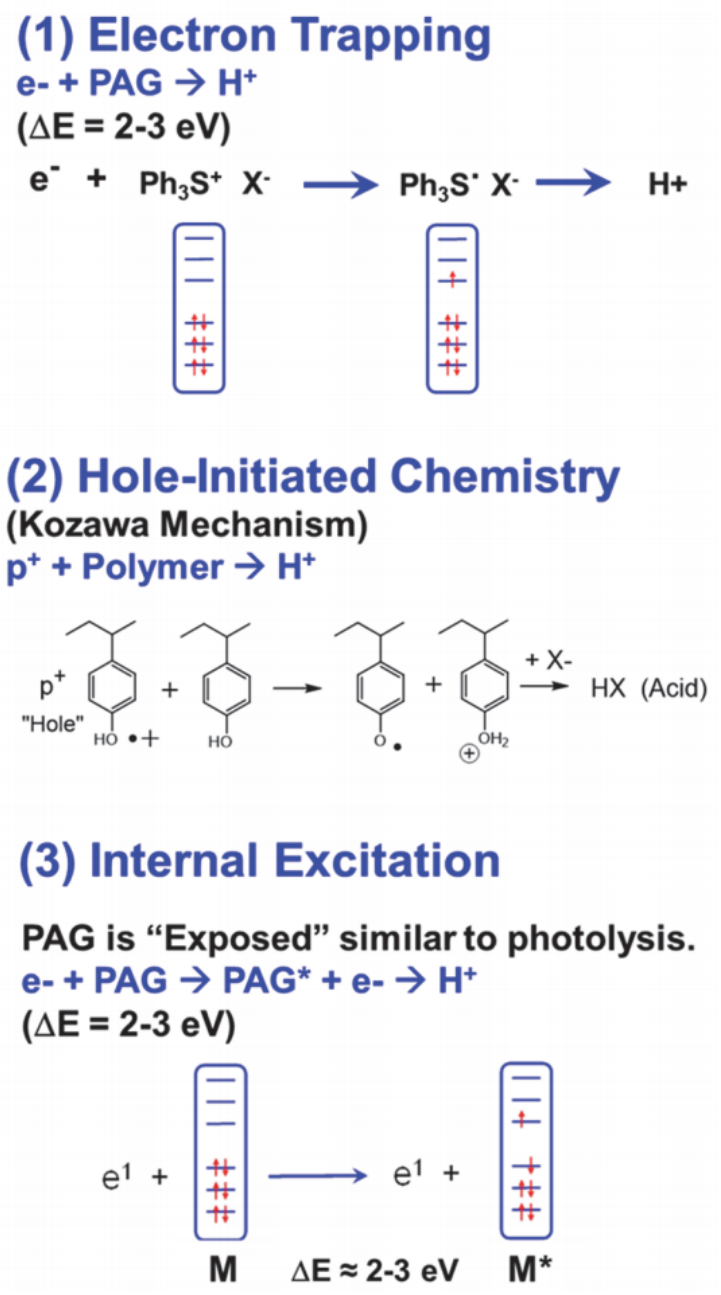

Figure 2.17 Three mechanisms involved in acid generation under high energy sources.(Figure adapted from Narasimhan, 2017 #588)

Under high energy sources such as e-beam and EUV lithography however, photoacids are typically generated following a complicated series of secondary electron-resist interactions that are not well understood but it is believed that the dominant chemical

mechanism responsible for acid generation is the transfer of a low energy electron (0 – 5 eV) onto the PAG from the resist matrix (Figure 2.17 1).[17, 25-27]. The secondary electron yield is critical in determining the number of photoacids generated and is dependent on properties of the resist material including its absorption coefficient and ionization potential.[28] TPS-3Ep-SbF_6 might have a lower secondary electron yield than 4-Ep, thus as the composition of the resist matrix is shifted from 4-Ep to TPS-3Ep-SbF_6 less photoacids are generated at the same dose. Another possibility is that at ultra-high PAG loadings, there is a competing mechanism caused by the direct excitation of PAGs by high energy electrons that is less efficient at acid generation. This is supported by previous work which showed that increasing PAG loading in a positive-tone molecular resist from 7.5 wt. % to 30 wt. % reduced the photoacid yield per mole of PAG by nearly 60 % under e-beam.[29] Direct interactions between high energy electrons and PAGs are not well studied as they are not typically the dominant reaction mechanism in chemically amplified resists where PAGs are only 5 mol. % of the resist composition.

Figure 2.18 shows lines nominally patterned at 50 nm of 4-Ep and TAS-3Ep-SbF_6 at both 55 mol. % and 100 mol. % using 100 keV e-beam lithography. At 100 mol. %, lines appear to have broadened slightly. As the films were patterned on bare silicon and thus are likely to have electrons backscattered into the resist, it difficult to accurately judge the LER of the material, and whether the line broadening observed at 100 mol. % PAG loading was due to propagation of polymerization outside of exposed regions or simply due to large amounts of electron backscattering at the high doses required for imaging. Even if pattern quality remained the same or was improved, the high doses required limit the usefulness of TPS-3Ep-SbF_6 as a single component resist for high-volume manufacturing.

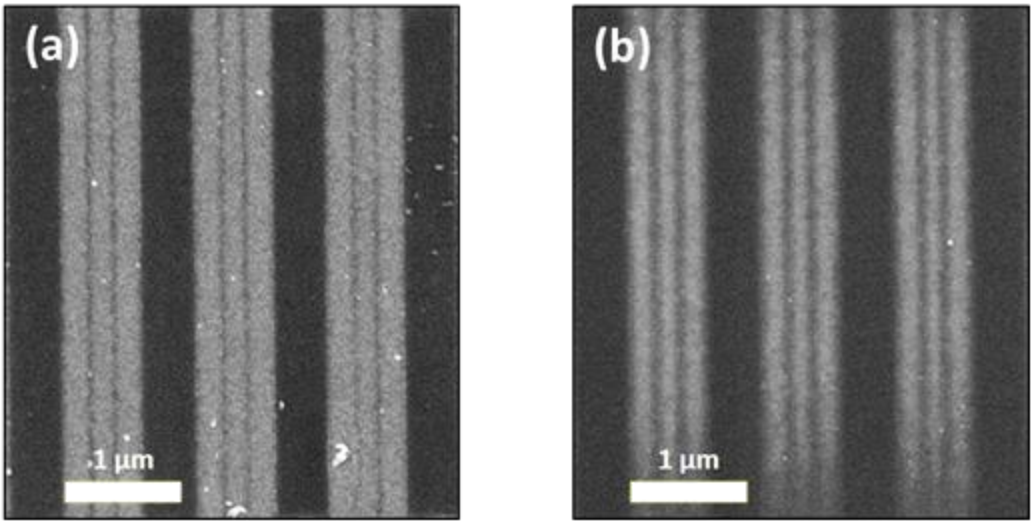

Figure 2.18 SEM images of lines nominally patterned at 50 nm at 55 mol. % (a) and 100 mol. % (b) TAS-3Ep-SbF_6 using 100 keV e-beam lithography.

TPS-OH-SbF_6

Contrast curves collected using DUV (Figure 2.19) and e-beam (Figure 2.20) of 4-Ep and TPS-OH-SbF_6 blends showed a similar divergence in behavior between the two exposure sources. DUV dose-response curves showed an increase in sensitivity from 5 mol. % to 15 mol.%, and a saturation in sensitivity up to 55 mol. % PAG, with a slight decrease in NRT between 30 and 55 mol. % PAG expected from the slight molar excess of a functional group with no homo-polymerization mechanism. In e-beam contrast curves, increasing PAG loading from 5 to 30 mol. % also improved sensitivity with a similar saturation up to 30 mol. % PAG. Increasing PAG loading to 55 mol. % decreased both sensitivity and NRT, unlike DUV. This is consistent with behavior observed using TPS-3Ep-SbF_6 and provides further evidence that there is indeed a decrease in photoacid yield above a certain PAG loading when using high energy exposure sources.

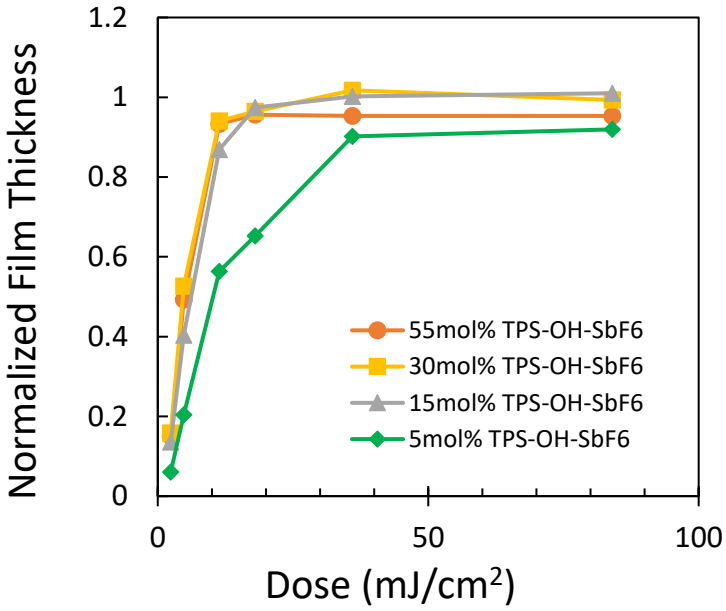

Figure 2.19 DUV contrast curves of 4-Ep containing TPS-OH-SbF_6 at various loadings.

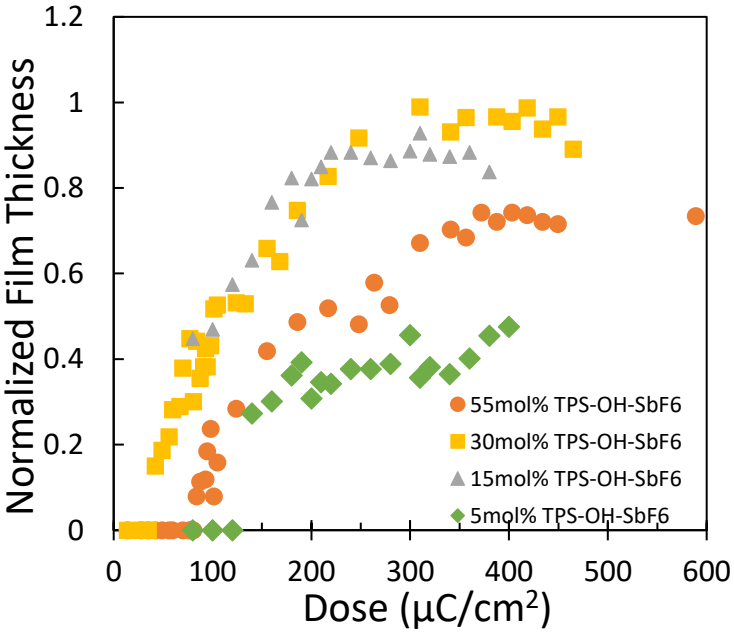

Figure 2.20 100 keV e-beam lithography contrast curves of 4-Ep containing TPS-OH-SbF_6 at 30 mol. % and 55 mol. %.

Figure 2.21 shows lines nominally patterned using 100 keV e-beam lithography at 50 nm of 4-Ep and TPS-OH-SbF_6 at both 30 and 55 mol. % with no immediately discernable difference in pattern quality 30 nm half-pitch lines . Dense 30 nm line:space patterns were also patterned and increasing PAG loading from 30 to 55 mol. % appeared to improve LER without a loss in resolution. These results are promising and suggest that these crosslinkable PAGs can be used at higher loadings to improve patterning performance of epoxide resists so long as loadings are not excessively high so as not to negatively impact sensitivity.

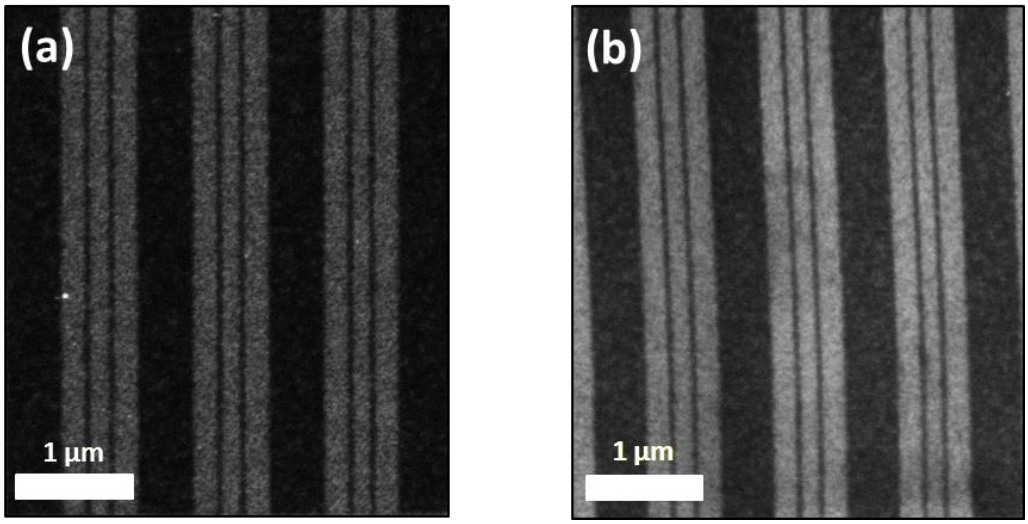

Figure 2.21 SEM images of lines nominally patterned at 50 nm at 30 mol. % (a) and 55 mol. % (b) TPS-OH-SbF_6 using 100 keV e-beam lithography.

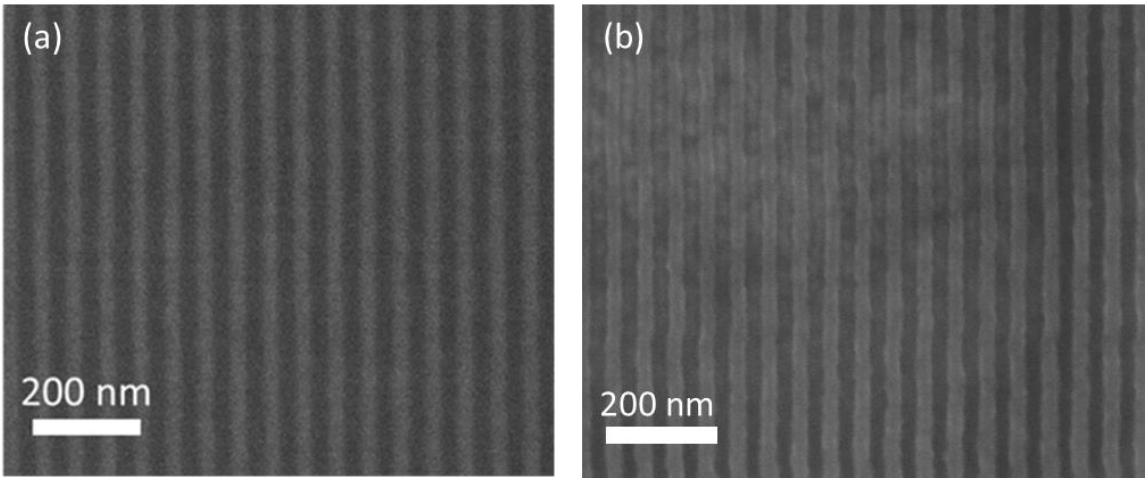

Figure 2.22 SEM images of 30 nm hp lines of 4-Ep and (a) 30 mol. % and (b) 55 mol. % TPS-OH-SbF_6 using 100 keV e-beam lithography.

2.3.4 Comparison of Methods of Crosslinking

The effect of the method of resist cross-linking at high PAG loadings (epoxide-epoxide for TAS-3Ep-SbF_6 and epoxide-phenol for TPS-OH-SbF_6) was examined by comparing contrast curves of 4-Ep and 55 mol. % of each PAG. Under DUV exposures (Figure 2.23) there was almost no difference in performance between the two PAGs except perhaps a small decrease in film thickness when using TPS-OH-SbF_6 which can be explained by the slight excess of phenols. The e-beam contrast curves were quite different however, and using the phenolic TPS-OH-SbF_6 PAG decreased both sensitivity and NRT. Because this behavior was exclusive to the high energy source, it is likely that it is caused by a difference in secondary electron trapping efficiency (the primary means of photoacid generation). This would imply that epoxide functionalized PAGs are preferable for use at high loadings in photoresists for EUV and e-beam lithography.

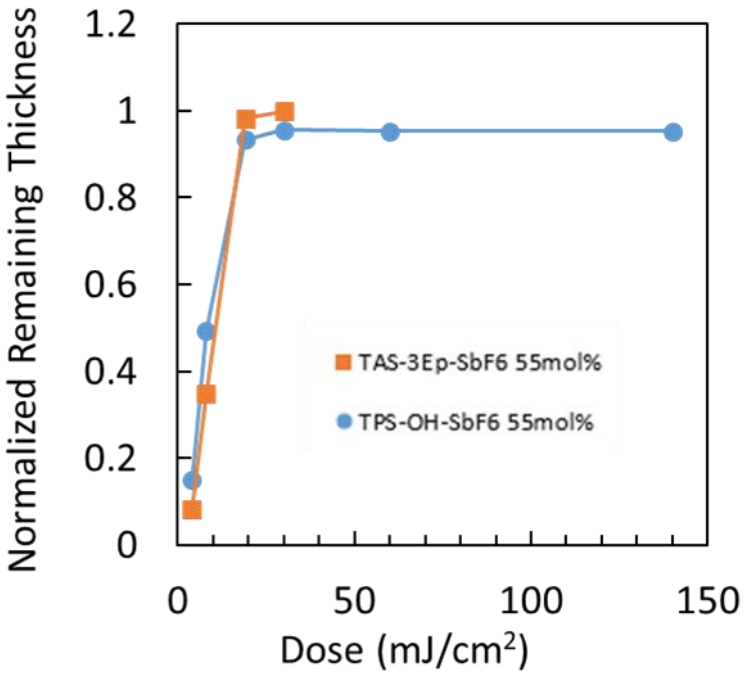

Figure 2.23 DUV contrast curves of 4-Ep containing 55 mol. % of TAS-3Ep-SbF_6 or TPS-OH-SbF_6.

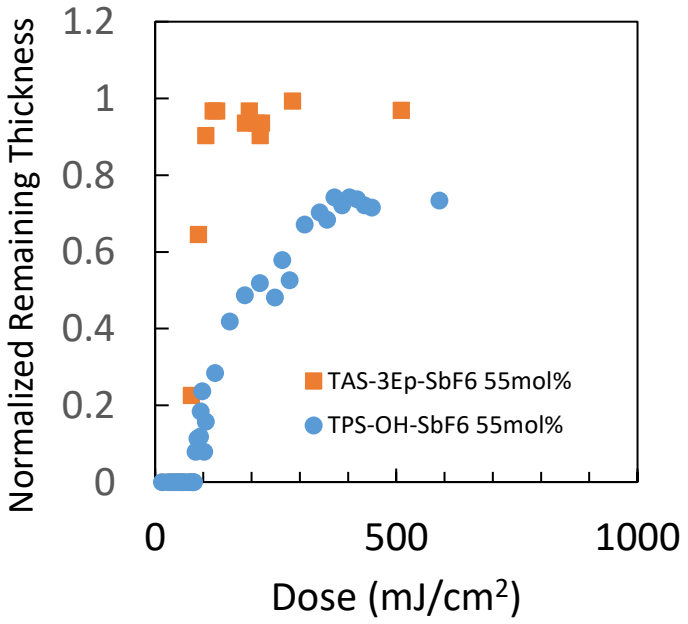

Figure 2.24 100 keV e-beam lithography contrast curves of 4-Ep containing 55 mol. % of TAS-3Ep-SbF_6 or TPS-OH-SbF_6.

2.4 Summary and Conclusions

A series of photoacid generators functionalized with groups capable of participating in cationic epoxide polymerization through epoxide-epoxide (TAS-3Ep-SbF_6) or epoxide-phenol crosslinking (TAS-OH-SbF_6 and TPS-OH-SbF_6) have been synthesized and examined for use at high loadings in a model epoxide resist (4-Ep) using DUV and e-beam lithography. It was confirmed that using un-functionalized PAG (TPS-SbF_6) at high loadings (above 10 mol. %) acted as a network diluent and decreased the extent of cross-linking of a negative tone epoxide resist (4-Ep). TAS-OH-SbF_6 was found to not cross-link efficiently with epoxides due to steric hindrance of the hydroxyl group and was not investigated further.

TAS-3Ep-SbF_6 and TPS-OH-SbF_6 were both identified as additives that could be used at higher loadings without decreasing the extent of cross-linking, TAS-3Ep-SbF_6 up to 100 mol. % and TPS-OH-SbF_6 up to 50 mol. %. Using these PAGs at moderately high loadings improved sensitivity under DUV and e-beam exposure sources, but was found to decrease sensitivity about 30 - 55 mol. % under e-beam but not DUV. The exact mechanism behind this behavior is unknown but is likely linked to differences in secondary electron yield between the resist (4-Ep) and the two PAGs. TAS-3Ep-SbF_6 was able to resolve 50 nm lines as both an ultra-high loaded PAG at 55 mol. % and as a single-component 100 mol. % resist with sensitivities of ~127.5 $\mu C/cm^2$ and ~480 $\mu C/cm^2$ respectively, but the effect of high PAG loading on line edge roughness could not be determined due to electron backscattering from the silicon substrate. TPS-OH-SbF_6 was also able to resolve 50 nm lines as well as 30 nm half-pitch lines at 30 mol. % and 55 mol. % when used as an ultra-high loaded PAG. Increasing TPS-OH-SbF_6 loading from 30 mol. % to 55 mol. % was

found to improve roughness and sensitivity without a noticeable increase in the spatial extent of polymerization.

Under DUV, little difference was seen in dose-response behavior between an epoxide functionalized and a phenol functionalized PAG when used in a resist at the same mol. %. Under e-beam however, resist blends using the phenol functionalized PAG was observed to have worse sensitivity and a lower degree of polymerization which was attributed to differences in secondary electron trapping efficiency between the two molecules. A more detailed discussion of the lower photoacid yields of TPS-OH-SbF_6 can be seen in Chapter 3. These molecules show promise for a new set of additives that can further optimize the performance of negative-tone molecular resists based on cationic polymerization, but further research is needed to better understand the mechanisms responsible for photoacid generation at ultra-high PAG loadings under high-energy exposure sources where the PAG is the major component in the resist.

2.5 References

1. Bristol, R. L., *The tri-lateral challenge of resolution, photospeed, and LER: scaling below 50nm?* SPIE: 2007; Vol. 6519, p 11.

2. Gallatin, G. M., *Resist blur and line edge roughness*. SPIE: 2004; Vol. 5754, p 15.

3. Lee, C.-T., Lawson, R. A. and Henderson, C. L., Understanding the effects of photoacid distribution homogeneity and diffusivity on critical dimension control and line edge roughness in chemically amplified resists. *Journal of Vacuum Science & Technology B: Microelectronics and Nanometer Structures Processing, Measurement, and Phenomena* **2008,** *26* (6), 2276-2280.

4. Yan, M., Choi, S., Subramanian, K. R. V. and Adesida, I., The effects of molecular weight on the exposure characteristics of poly(methylmethacrylate) developed at low temperatures. *Journal of Vacuum Science & Technology B: Microelectronics and Nanometer Structures Processing, Measurement, and Phenomena* **2008,** *26* (6), 2306-2310.

5. Yoo, J. B., Park, S.-W., Kang, H. N., Mondkar, H. S., Sohn, K., Kim, H.-M., Kim, K.-B. and Lee, H., Triphenylsulfonium salt methacrylate bound polymer resist for electron beam lithography. *Polymer* **2014,** *55* (16), 3599-3604.

6. Jung, J. H., Kim, M. J., Sohn, K. H., Kang, H. N., Kang, M. K. and Lee, H., Enhanced Acid Diffusion Control by Using Photoacid Generator Bound Polymer Resist. *Journal of Nanoscience and Nanotechnology* **2015,** *15* (2), 1764-1766.

7. De Silva, A., Felix, N. M. and Ober, C. K., Molecular Glass Resists as High-Resolution Patterning Materials. *Advanced Materials* **2008,** *20* (17), 3355-3361.

8. Krysak, M., Silva, A. D., Sha, J., Lee, J.-K. and Ober, C. K., *Molecular glass resists for next-generation lithography*. SPIE: 2009; Vol. 7273, p 8.

9. Yeh, W.-M., Noga, D. E., Lawson, R. A., Tolbert, L. M. and Henderson, C. L., Comparison of positive tone versus negative tone resist pattern collapse behavior. *J Vac Sci Technol B* **2010,** *28* (6), C6S6-C6S11.

10. Dušek, K. and Havlíček, I., Diffusion controlled kinetics of crosslinking. *Prog Org Coat* **1993,** *22* (1), 145-159.

11. Matsuoka, S., Quan, X., Bair, H. E. and Boyle, D. J., A model for the curing reaction of epoxy resins. *Macromolecules* **1989,** *22* (10), 4093-4098.

12. Narcross, H., Lawson, R. A., Sharp, B., Chun, J. S., Neisser, M., Tolbert, L. M. and Henderson, C. L., Effect of Molecular Resist Structure on Glass Transition Temperature and Lithographic Performance in Epoxide Functionalized Negative Tone Resists. *Proc Spie* **2015,** *9425*.

13. Lawson, R. A., Chun, J. S., Neisser, M., Tolbert, L. M. and Henderson, C. L., Methods of controlling cross-linking in negative-tone resists. *Advances in Patterning Materials and Processes Xxxi* **2014,** *9051*.

14. Crivello, J. V., Photoinitiated cationic polymerization with triarylsulfonium salts - Reflections. *J Polym Sci Pol Chem* **1996,** *34* (16), 3227-3228.

15. Lawson, R. Molecular Resists for Advanced Lithography - Design, Synthesis, Characterization, and Simulation. Georgia Institute of Technology, 2011.

16. Lin-Gibson, S., Baranauskas, V., Riffle, J. S. and Sorathia, U., *Cresol novolac-epoxy networks: Properties and processability*. 2002; Vol. 43, p 7389-7398.

17. Grzeskowiak, S., Narasimhan, A., Rebeyev, E., Joshi, S., Brainard, R. L. and Denbeaux, G., Acid Generation Efficiency of EUV PAGs via Low Energy Electron Exposure. *J Photopolym Sci Tec* **2016,** *29* (3), 453-458.

18. Narasimhan, A. K., Grzeskowiak, S., Srivats, B., Herbol, H. C., Wisehart, L., Schad, J. L., Kelly, C., Earley, W., Ocola, L. E., Neisser, M., Denbeaux, G. H. and

Brainard, R. L., *Studying thickness loss in extreme ultraviolet resists due to electron beam exposure using experiment and modeling*. SPIE: 2015; Vol. 14, p 1-6, 6.

19. Hassanein, E., Higgins, C., Naulleau, P., Matyi, R., Gallatin, G., Denbeaux, G., Antohe, A., Thackeray, J., Spear, K., Szmanda, C., Anderson, C. N., Niakoula, D., Malloy, M., Khurshid, A., Montgomery, C., Piscani, E. C., Rudack, A., Byers, J., Ma, A., Dean, K. and Brainard, R., Film quantum yields of EUV & ultra-high PAG photoresists. *Emerging Lithographic Technologies Xii, Pts 1 and 2* **2008,** *6921*.

20. Fallica, R. and Ekinci, Y., Photoacid generator-polymer interaction on the quantum yield of chemically amplified resists for extreme ultraviolet lithography. *J Mater Chem C* **2018,** *6* (27), 7267-7273.

21. Furutani, H., Shirakawa, M., Nihashi, W., Sakita, K., Oka, H., Fujita, M., Omatsu, T., Tsuchihashi, T., Fujimaki, N. and Fujimori, T., Novel EUV resist materials for 7 nm node and beyond. *Advances in Patterning Materials and Processes Xxxv* **2018,** *10586*.

22. Grzeskowiak, S., Narasimhan, A., Ostrander, J., Schad, J., Earley, W., Brainard, R. L., Denbeaux, G., Ocola, L. E. and Neisser, M., Cross sections of photoacid generators at low electron energies. *J Vac Sci Technol B* **2015,** *33* (6), 06FH01.

23. Yamamoto, H., Kozawa, T., Tagawa, S., Yukawa, H., Sato, M. and Onodera, J., Enhancement of Acid Production in Chemically Amplified Resist for Extreme Ultraviolet Lithography. *Appl Phys Express* **2008,** *1*, 047001.

24. Sharp, B. L., Narcross, H. L., Ludovice, P., Tolbert, L. M. and Henderson, C. L., Structural effects on the performance of epoxide-based negative-tone molecular resists. *J Vac Sci Technol B* **2019,** *37* (1).

25. Ameixa, J., Arthur-Baidoo, E., Meißner, R., Makurat, S., Kozak, W., Butowska, K., Silva, F. F. d., Rak, J. and Denifl, S., Low-energy electron-induced decomposition of 5-trifluoromethanesulfonyl-uracil: A potential radiosensitizer. *The Journal of Chemical Physics* **2018,** *149* (16), 164307.

26. Kozawa, T. and Tagawa, S., Radiation Chemistry in Chemically Amplified Resists. *Jpn J Appl Phys* **2010,** *49* (3).

27. Nakano, A., Okamoto, K., Yamamoto, Y., Kozawa, T., Tagawa, S., Kai, T. and Nemoto, H., Dependence of Acid Yield on Acid Generator in Chemically Amplified Resist for Post-Optical Lithography. *Jpn J Appl Phys* **2005,** *44* (7B), 5832-5835.

28. Mack, C. A., Thackeray, J. W., Biafore, J. J. and Smith, M. D., Stochastic Exposure Kinetics of EUV Photoresists: A Simulation Study. *Extreme Ultraviolet (Euv) Lithography Ii* **2011,** *7969*.

29. Lawson, R. A., Tolbert, L. M. and Henderson, C. L., Single-component molecular resists containing bound photoacid generator functionality. *J Micro-Nanolith Mem* **2010,** *9* (1).

CHAPTER 3. PHENOL-FUNCTIONALIZED POLYMERIZATION CONTROL ADDITIVES

3.1 Introduction

As previously discussed, negative tone molecular resists based on the photoacid catalyzed polymerization of groups such as epoxides have shown promise as candidate photoresists for next generation lithography techniques such as e-beam or EUV due to their resistance to pattern collapse, environmental stability, and little to no outgassing. Additionally, as the growing chain ends lose mobility as the network polymerizes, these resists should theoretically have some intrinsic level of resolution/diffusion control which varies based on the glass transition temperature of the system.

One such resist 1,1,2,2-tetrakis(4-(oxiran-2-ylmethoxy)phenyl)ethane (4-Ep) demonstrated promising patterning results but was initially resolution limited to 35 nm due to resist blur where patterned features were larger than the exposed area.[1] This was attributed to propagation of polymerization outside of exposed regions during the post exposure bake step before the resist had cross-linked enough to immobilize the active chain ends. Line blur is a common problem in chemically amplified resists where photoacids can diffuse outside of exposed regions and increase the spatial extent of whatever chemistry is responsible for the local change in solubility. Traditionally, an additive called a base quencher is used to improve resolution by acting as a buffer and neutralizing photoacids that diffuse into nominally unexposed regions (Figure 3.1).[2]

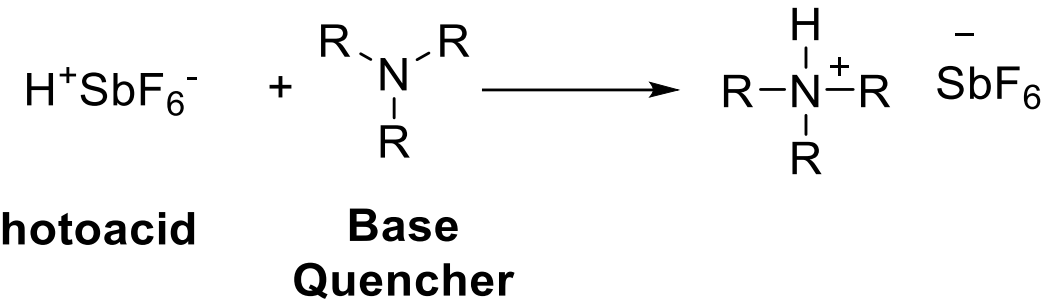

Figure 3.1 Sample neutralization reaction between a photoacid and a tertiary amine base quencher.

While the addition of base quencher to a CAR is often commensurate to a loss in sensitivity (as photoacids are neutralized in both exposed and unexposed regions) it can be worth it due to the improvements to resolution, LER, and contrast between high and low-dose areas. Unfortunately, base quenchers were demonstrated to be ineffective at improving the resolution of resists such as 4-Ep which was attributed to the difference in imaging mechanisms.[3] Traditionally in CARs, the photoacid initiates a solubility switching mechanism such as a deprotection reaction and is regenerated, thus catalyzing multiple reactions. In resists based on the cationic homo-polymerization of groups such as epoxides however, photoacids have a short lifetime before initiating polymerization and are not regenerated unless a chain-transfer agent is present (Figure 3.2). The predominate reactive species are the cationic chain ends which have little reactivity towards the base and are not terminated by the addition of base quencher. Therefore, any additive that works analogously to a base quencher in these systems must control the rate and extent of cross-linking and not the photoacid.

Our group has previously examined two methods of controlling the acid-catalyzed polymerization of epoxides, the first being a photo-decomposable nucleophile (PDN)

triphenylsulfonium triflate (TPS-Tf). This is an onium salt with a stronger nucleophile than hexafluoroantimonate that in exposed regions is converted into triflic acid which acts as a chain-transfer agent and (to a lesser extent) can initiate polymerization but in unexposed regions (Figure 3.2).[3] In unexposed regions, the triflic anion reacts with active chain ends and effectively quenches polymerization.

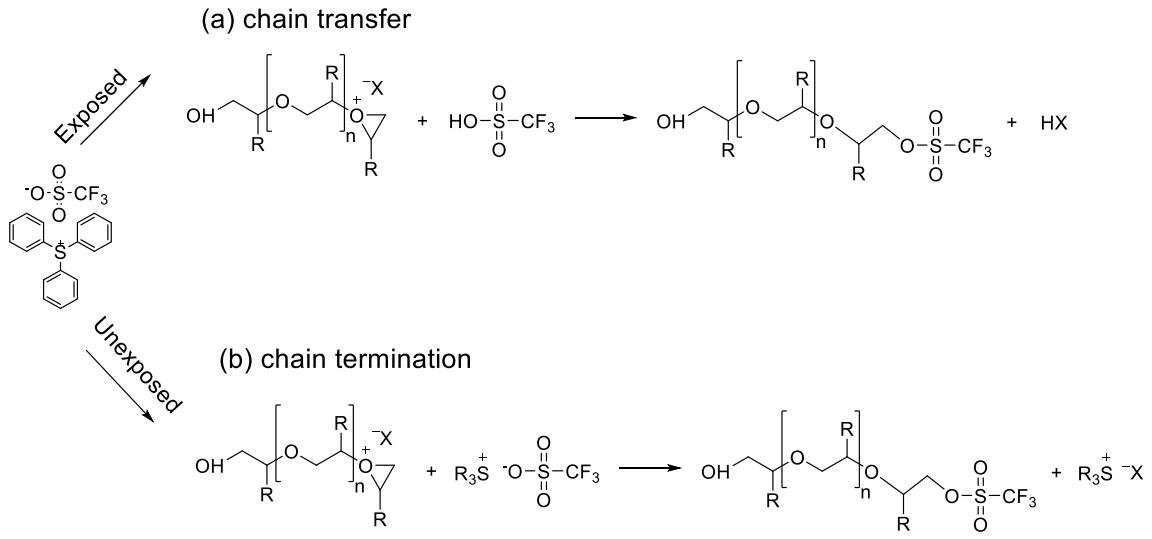

Figure 3.2 Reactions of an active epoxide chain end with a PDN in both unexposed and exposed regions.

Another method investigated was the introduction of phenols onto a resist structure, which was demonstrated to slow/control the rate of cross-linking by some combination of increasing the glass transition temperature (T_g) of the resist film (thus decreasing the mobility of active chain ends) and the introduction of a new reaction pathway (Figure 3.3 c), which terminates a growing chain-end and regenerates the photoacid that then must react with another epoxide for cross-linking to continue.[3-5] Both methods were promising, but required either the use of an additive which cannot be cross-linked into the network (limiting the total possible loading) or structural modification of the resist itself. In order to probe the ultimate resolution of negative tone epoxide resists, it would therefore be

useful to combine both methods of cross-linking control into additives that could be added to a wide variety of epoxide cross-linking resists.

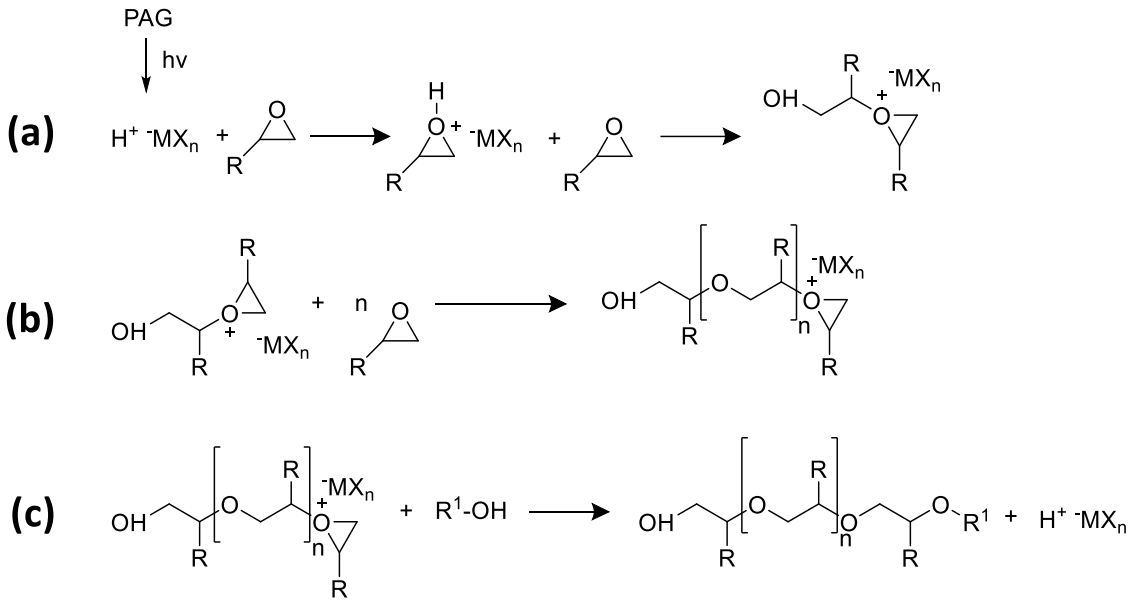

Figure 3.3 Possible cross-linking reactions of epoxide resists: initiation (a) epoxide-epoxide cross-linking (b) or epoxide-phenol cross-linking if a phenol functionalized species is present (c).

To this end, both a photo-decomposable nucleophile (TPS-Tf) and a photo-acid generator (TPS-SbF_6) were functionalized with phenolic groups with the expectation that their phenol functionalized equivalents (TPS-OH-Tf and TPS-OH-SbF_6) could be blended into any negative tone epoxide resist and improve polymerization control/resolution without requiring structural modification of the resist itself and could be used at higher loadings than their un-functionalized analogues without decreasing the extent of conversion of the network. Additionally, if the phenol-functionalized PAG provides enough control over cross-linking in unexposed regions, it might eliminate the need for a PDN entirely.

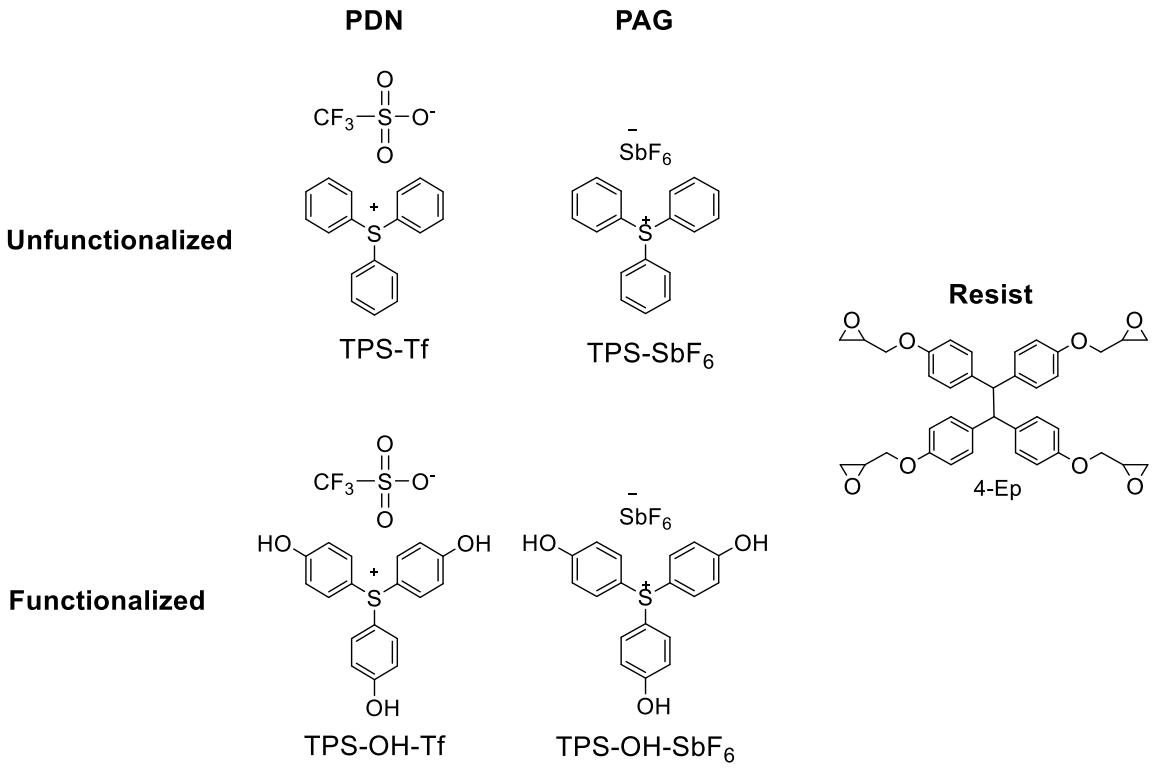

Figure 3.4 Structures of the resist (4-Ep) and additives investigated in this study.

3.2 Experimental

3.2.1 Materials and Methods

All reagents unless otherwise noted were purchased from TCI America, Alfa-Aesar, or Sigma-Aldrich and used without further purification. TPS-SbF_6 was purchased from Midori-Kagura. All synthesis was performed in a laboratory equipped with UV-light filters in order to prevent accidental exposure of the PAGs/PDNs during synthesis and handling. Resist solutions were prepared using 2 wt. % solids in ethyl lactate. Formulations used in exposures were prepared by blending together solutions of 4-Ep with the appropriate amounts of PAG and/or PDN solution to achieve the desired mol. % of PAG and/or PDN. Each solution was cast onto a silicon wafer piece (ordered from

University Wafer and cleaned with oxygen plasma for 5 min immediately prior to use) by spin-coating at 2000 rpm for 1 minutes. All wafers were subjected to a post-apply bake (PAB) at 60 ^{o}C for 2 min and a 90 ^{o}C post-exposure bake (PEB) for 1 min. This was followed by development in methyl isobutyl ketone (MIBK) for 30 seconds and a 10 second rinse with isopropyl alcohol (IPA). ^{1}H NMR spectra were collected with a Varian Mercury Vx 300 spectrometer. Deep Ultraviolet (DUV) exposures were performed with an Oriel Instruments 500 W Hg-Xe arc lamp using a 248 nm bandpass filter, and the resulting film thicknesses were measured using a M-2000 Woolam Ellipsometer. Film thickness measurements collected using ellipsometry were also used to calculate the glass transition temperatures of different resist blends. E-beam exposures and patterning were performed with a JEOL JBX-9300FS electron beam lithography system, using an acceleration voltage of 100 keV, a 100 pA current, and a 2 nm shot pitch. Film thicknesses for e-beam contrast curves were measured using a Tencor KLA P15 Profilometer. E-beam patterns were imaged using a Carl Zeiss Ultra 60 scanning electron microscope (SEM) with a 2 keV acceleration voltage.

3.2.2 Synthesis of TPS-OH-Cl

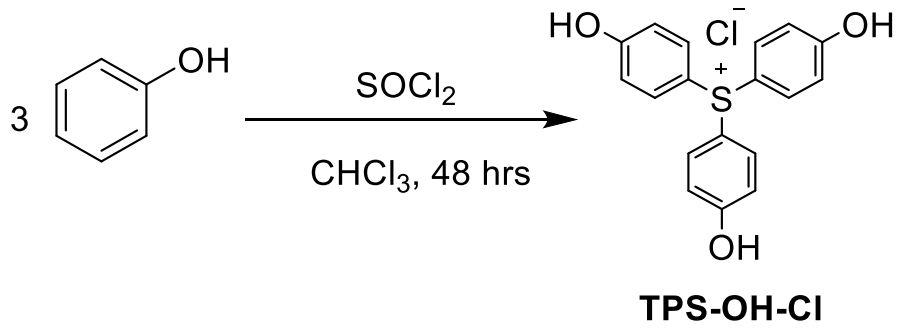

Figure 3.5 Synthetic scheme for TPS-OH-Cl.

Tris(4-hydroxyphenyl)sulfonium chloride (TPS-OH-Cl) synthesis is described in Chapter 1. ^{1}H NMR (300 MHz DMSO) δ (ppm): 7.52 (d, J = 9.0, 6H), 7.04 (d, J = 9.0, 6H). ESI-MS *m/z*: M^{+} 311.0 (100.0%), 312.0 (19.5%), 313.0 (4.5%). Anal. Calcd for $C_{18}H_{15}O_3S^{+}Cl^{-}$: C, 62.34; H, 4.36; S, 9.24. Found: C, 62.40; H, 4.61; S, 9.02. Yield: 82 %.

3.2.3 Synthesis of TPS-OH-Tf

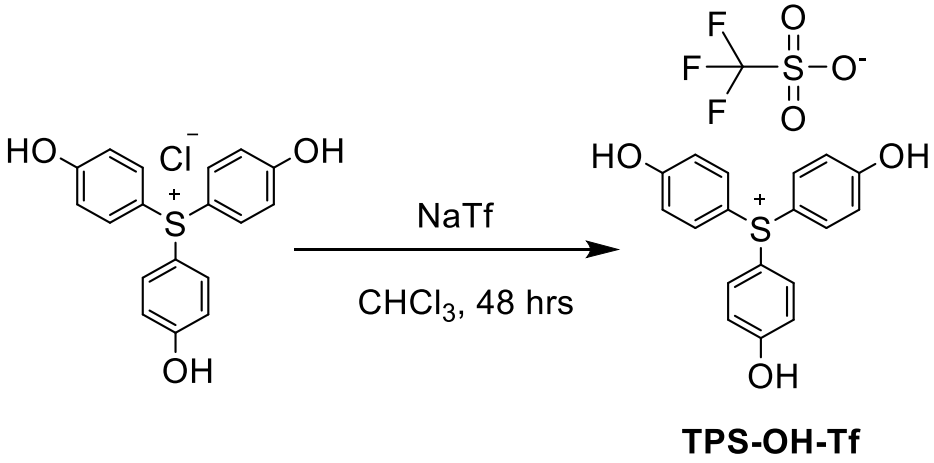

Figure 3.6 Synthetic scheme for TPS-OH-Tf.

TPS-OH-Cl (1.00 g, 2.88 mmol, 1 equiv.) and sodium triflate (0.50 g, 2.88 mmol, 1 equiv.) were added to a vial containing 7 mL acetone and 0.5 mL deionized (DI) water. The vial was capped and the solution was stirred vigorously overnight at room temperature. Precipitated solids were then filtered out of solution, re-dissolved in ethyl acetate, and washed three times with DI water to remove any remaining sodium salts. The combined organic layers were dried over magnesium sulfate ($MgSO_4$) and excess solvent was removed using rotary evaporation to give the product tris(4-hydroxyphenyl)sulfonium triflate (TPS-OH-Tf), a white powder. ^{1}H NMR (300 MHz DMSO-d6) δ (ppm): 7.53 (dd, J = 8.7, 6H), 7.04 (dd, J = 9.0, 6H). ESI-MS *m/z*: M^{+} 311.2 (100.0%), 312.2 (19.5%), 313.3

(4.5%) M^- 149.0 (100.0%) 150.9 (4.5%). Anal. Calcd for $C_{18}H_{15}O_3S^+CF_3SO_3^-$: C, 49.56; H, 3.28; S, 13.93. Found: C, 50.24; H, 3.81; S, 12.81. Yield: 47 %.

3.2.4 Synthesis of TPS-OH-SbF_6

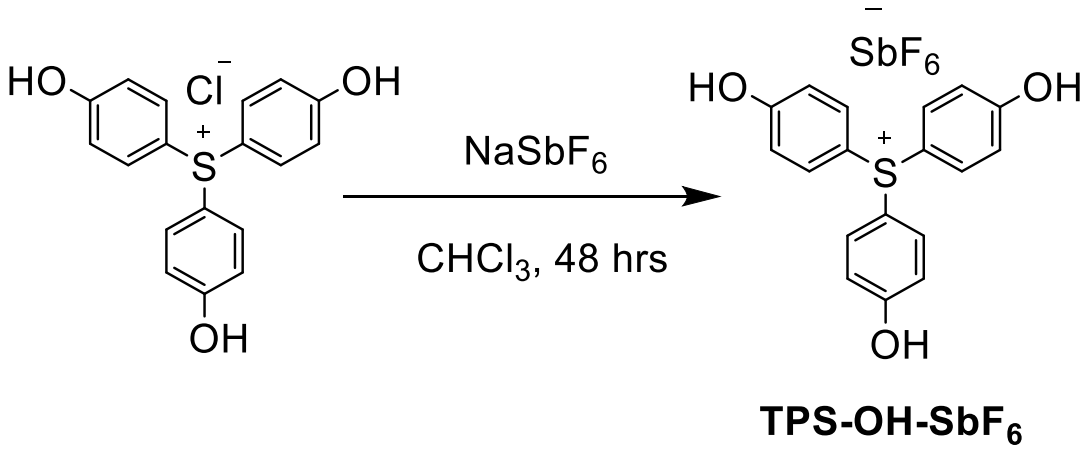

Figure 3.7 Synthetic scheme for TPS-OH-SbF_6.

Tris(4-hydroxyphenyl)sulfonium hexafluoroantimonate (TPS-OH-SbF_6) synthesis is discussed in Chapter 1. ^{1}H NMR (300 MHz DMSO) δ (ppm): 7.53 (d, J = 8.7, 6H), 7.05 (d, J = 8.7, 6H). ESI-MS *m/z*: M^+ 311.0 (100.0%), 312.0 (19.5%), 313.0 (4.5%) M^- 234.7.0 (100.0%) 236.90 (74.8%). Anal. Calcd for $C_{18}H_{15}O_3S^+SbF_6^-$: C, 39.52; H, 3.12; S, 5.84. Found: C, 40.19; H, 3.43; S, 5.30. Yield: 55 %.

3.3 Results and Discussion

3.3.1 Effect of Phenol Functionalization on Cross-linking

Initial DUV contrast curves of 4-Ep were collected using 5 mol. % of either un-functionalized or phenol functionalized additives in order to investigate the effect of the additive functionalization on resist cross-linking behavior (Figure 3.8). Resist blends

containing the functionalized additives showed an increase in E_1 (the exposure dose at which the normalized remaining film thickness or NRT has reached 1) away from 0 mJ/cm^2 but no change in the maximum NRT. These results indicate that the rate of cross-linking in resists containing the functionalized additives is slower, as at an identical PEB time (during which cross-linking occurs) resists with the functionalized additives demonstrate a lower NRT/extent of cross-linking at the same dose until E_1, at which point enough acid/cross-linking events are generated such that the resist film is rendered insoluble despite the slower rate of reaction. This is consistent with the predicted effect of phenols slowing/controlling cross-linking by either increasing the T_g and/or introducing an additional chain-transfer like cross-linking pathway.

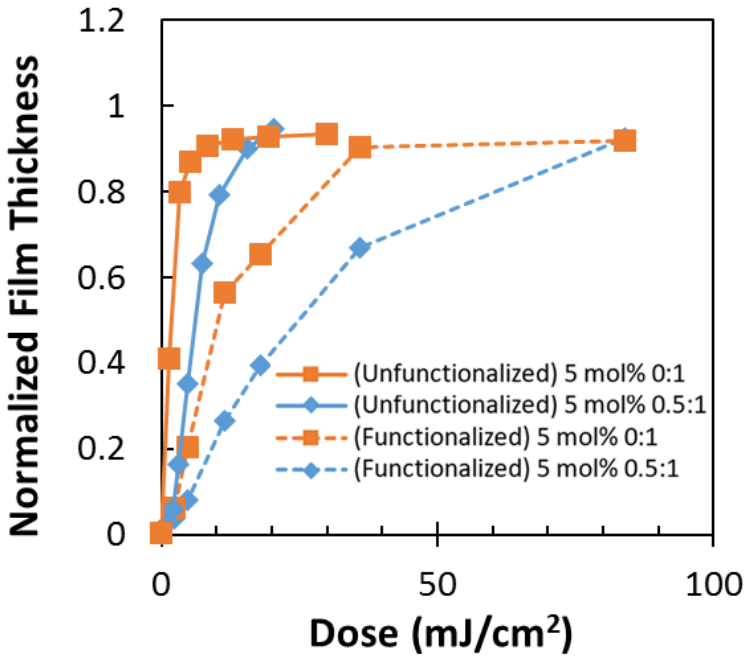

Figure 3.8 DUV contrast curves showing the differences in cross-linking behavior when using 5 mol. % of phenol functionalized or unfunctionalized PAG. Amount of functionalized/unfunctionalized PDN reported as a molar ratio relative to PAG (PDN:PAG).

The extent to which the addition of a phenol functionalized additive affected the T_g (and subsequently the cross-linking kinetics) of the resist was investigated by measuring the T_g of 4-Ep as a function of mol. % TPS-OH-SbF_6 (Figure 3.10) using ellipsometry and a heating stage. 4-Ep solutions with different mol. % PAG were prepared and spin-coated onto clean silicon wafer pieces. Thickness measurements were collected every 10 seconds while heating the wafer at a rate of 8 °C/min. The T_g was determined to be the point at which the coefficient of thermal expansion (CTE) changed during the third heating cycle, as seen in Figure 3.9.

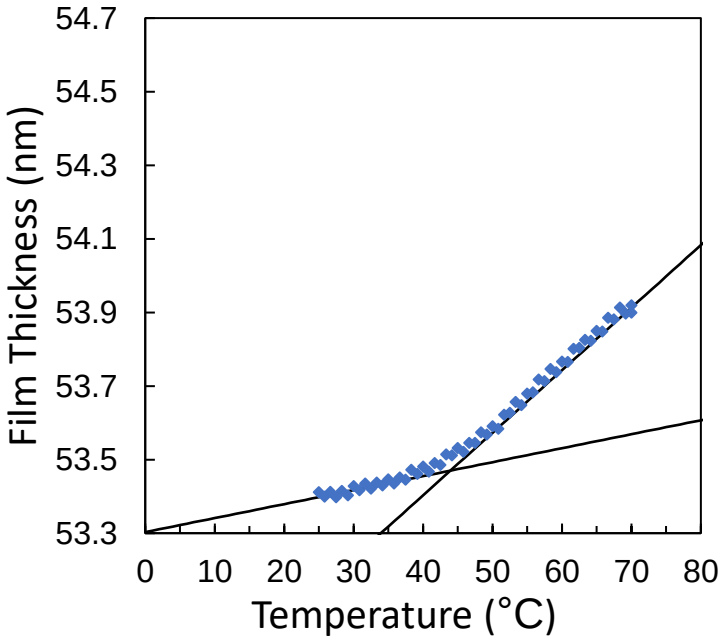

Figure 3.9 Hot stage ellipsometry curve for the third heating cycle of 4-Ep.

At 10 mol. % TPS-OH-SbF_6 (representing a resist blend containing 5 mol. % each of functionalized PAG and PDN) the T_g was only increased by roughly a single degree, and only by 3 degrees at the highest additive loading investigated in this chapter (15 mol. % each functionalized PAG and PDN represented by 30 mol. % TPS-OH-SbF_6). This alone

is unlikely to significantly affect the diffusion coefficient of the active chain ends in the un-crosslinked or cross-linked resist and the rate of cross-linking. The decrease in the rate of cross-linking can therefore be primarily attributed to the additional epoxide-phenol cross-linking mechanism which slows the overall rate of epoxide conversion (Figure 3.3 c).

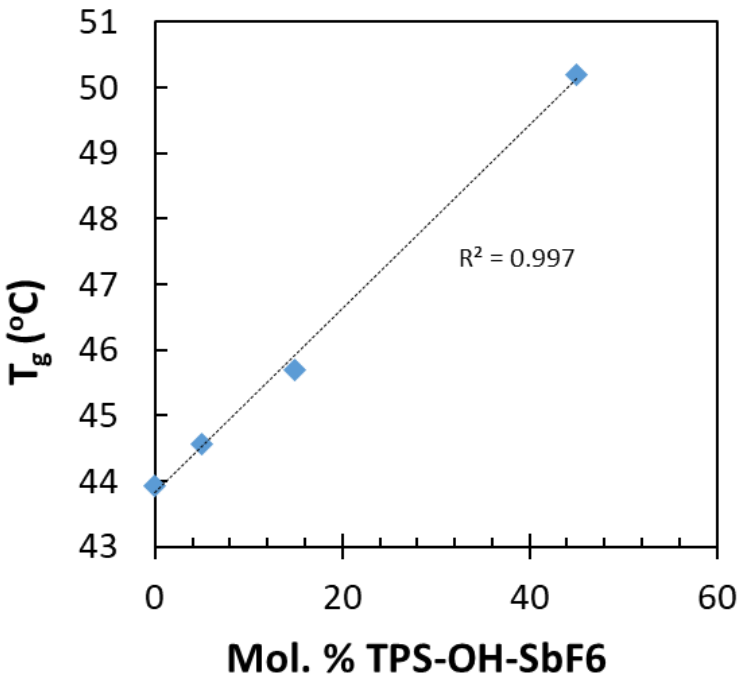

Figure 3.10 T_g of 4-Ep films as a function of mol. % phenol-functionalized PAG.

Contrast curves of 4-Ep with either 5 mol. % of TPS-SbF_6 or TPS-OH-SbF_6 collected using e-beam demonstrated markedly different behavior than DUV contrast curves (Figure 3.11). The resist blend using TPS-OH-SbF_6 showed the same shift in the dose-response curve attributed to a slower rate of cross-linking but was unable to reach the same NRT as the resist blend using TPS-SbF_6 at any dose.

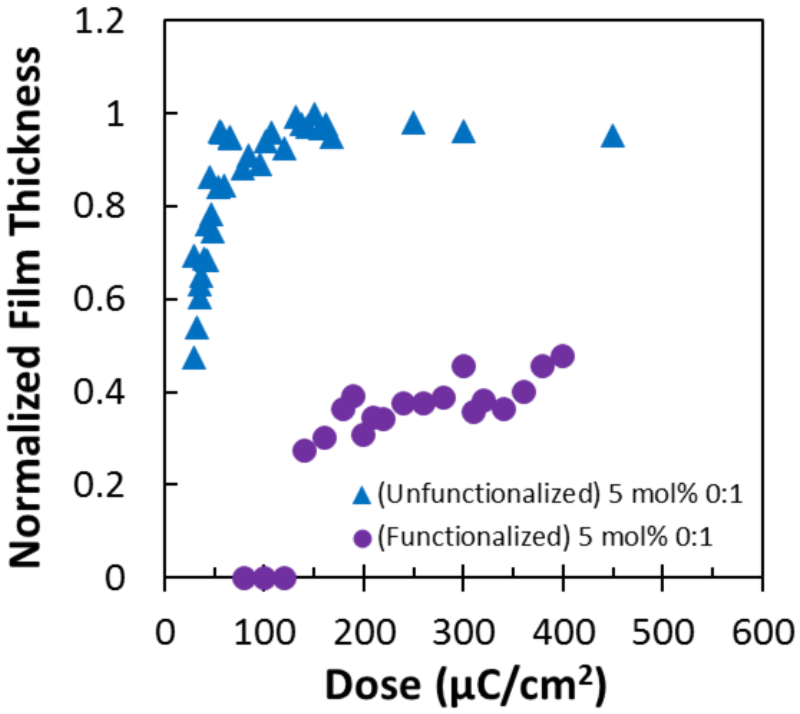

Figure 3.11 100 keV e-beam contrast curves of 4-Ep using 5 mol. % of either the phenol-functionalized (TPS-OH-SbF_6) or unfunctionalized (TPS-SbF_6) PAG.

This is likely due to the difference in the radiation chemistry between the two exposure sources and how photoacids are generated; under DUV acids are generated primarily by the direct absorption of DUV photons by the PAG whereas under e-beam photoacids are primarily generated via a series of excited state electron transfers requiring the transfer of a secondary electron from the resist material onto the PAG.[6] It has been observed that PAG electron affinity has good correlation with acid generation efficiency under high energy exposure sources, which was attributed to the ability of PAGs with high electron affinities to more efficiently capture secondary electrons (the primary means of acid generation under high-energy sources).[7, 8] It has also been reported that the incorporation of electron withdrawing groups onto the aromatic rings in sulfonium salt

PAGs increased their electron affinity; therefore it is reasonable to assume that the incorporation of the electron donating phenolic groups could decrease its electron affinity and thus their acid generation efficiency.[9, 10] If this is the case than higher loadings of TPS-OH-SbF_6 will be required to generated the same amount of photoacid as TPS-SbF_6 at the same dose. Previous work confirms that phenol functionalization allows for TPS-OH-SbF_6 to be used at higher loading without affecting the cross-link density of 4-Ep, so blends with higher amounts of phenol functionalized PAG and PDN were investigated in the hopes that this would improve both sensitivity and NRT.[11]

3.3.2 Additive Loading Effects

Contrast curves of 4-Ep were collected using DUV (298 nm) light and the TPS-OH-SbF_6 photoacid generator at "typical" (5 mol. %) and "high" (15 mol. %) loadings, and a varying amount of the TPS-OH-Tf photodecomposable nucleophile reported as a molar ratio relative to the PAG (PDN:PAG) (Figure 3.12). Resist blends using high PAG loadings demonstrated greater sensitivity and higher NRT values than those using typical loadings at all amounts of PDN added, as would be expected. Increasing the amount of PDN reduced sensitivity and NRT which is consistent with previous results indicating that it is much slower initiator of polymerization and acts as a chain transfer agent to slow the rate of cross-linking even more.

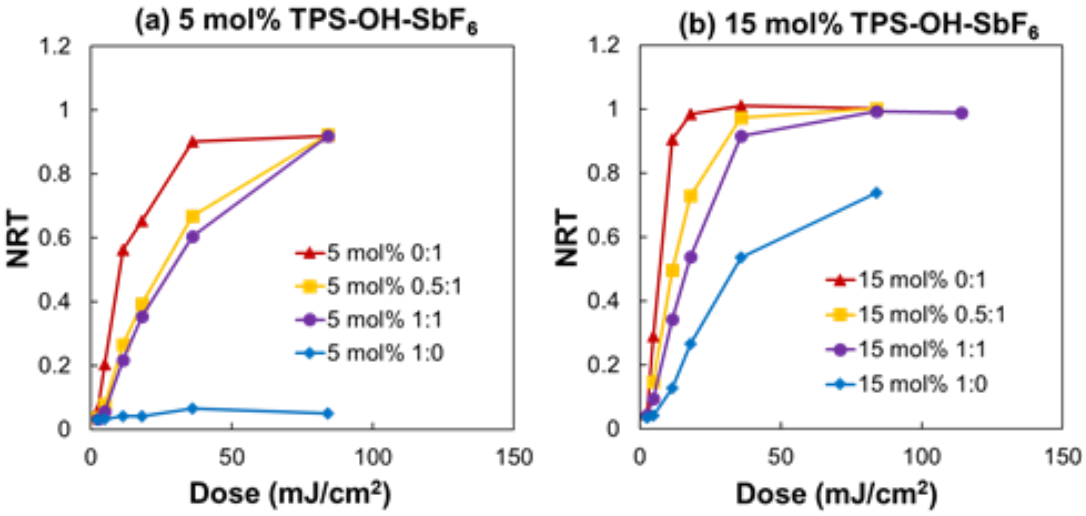

Figure 3.12 DUV contrast curves of 4-Ep with 5 mol. % (a) or 15 mol. % (b) of the TPS-OH-SbF_6 PAG and different amounts of the TPS-OH-Tf PDN reported as a molar ratio relative to the amount of PAG (PDN:PAG).

Contrast curves of 4-Ep were collected using 100 keV e-beam lithography showed similar trends, but most importantly demonstrated that by moving to higher PAG loadings the sensitivity and NRT could be improved.

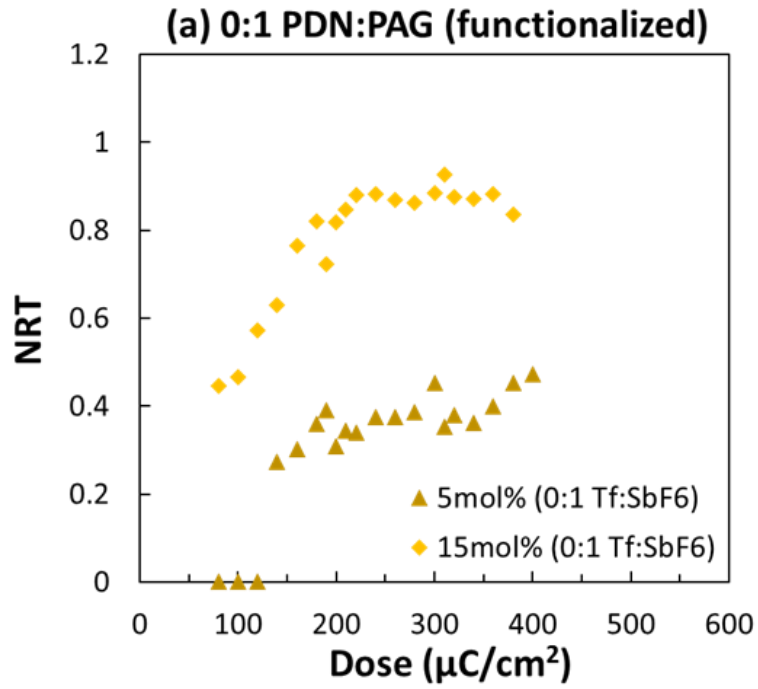
(a) 0:1 PDN:PAG (functionalized)
NRT
Dose (μC/cm²)
5mol% (0:1 Tf:SbF6)
15mol% (0:1 Tf:SbF6)

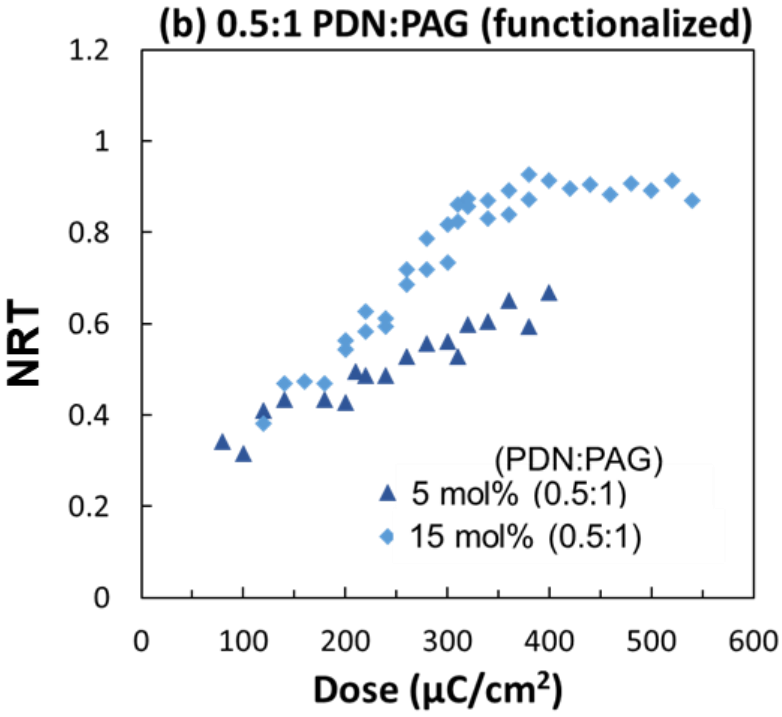
(b) 0.5:1 PDN:PAG (functionalized)
NRT
Dose (μC/cm²)
(PDN:PAG)
5 mol% (0.5:1)
15 mol% (0.5:1)

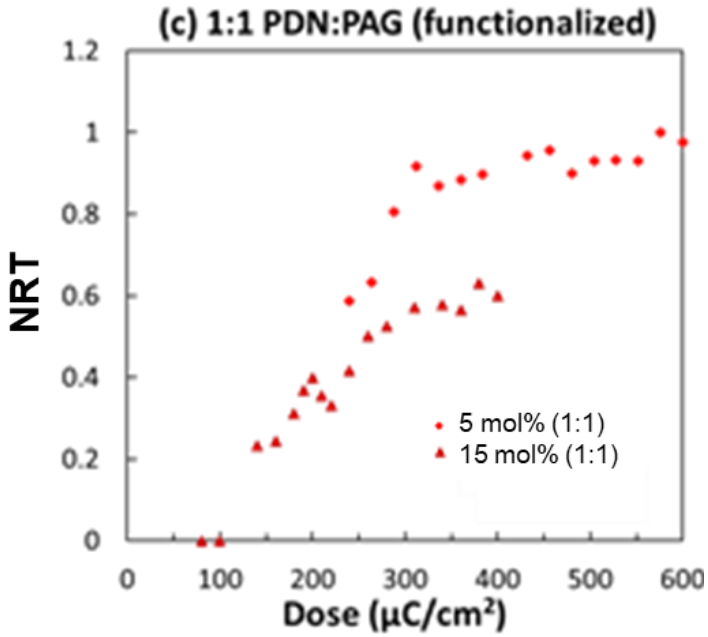

Figure 3.13 100 keV e-beam contrast curves of 4-Ep using 5 or 15 mol. % phenol-functionalized PAG (TPS-OH-SbF_6) and PDN:PAG molar ratios of (a) 0:1 (b) 0.5:1 or (c) or 1:1.

3.3.3 E-Beam High Resolution Patterning

Initial 30 nm 1:1 line/space patterns were imaged using 100 keV e-beam lithography to quickly compare the imaging performance of 4-Ep at a variety of PAG and PDN loadings (Figure 3.14). At "typical" 5 mol. % PAG loading, no pattern collapse was observed in any of the resist blends. With no PDN, line broadening and bridging defects caused by low cross-link density and/or the propagation of polymerization outside of exposed regions were observed. The addition of PDN at a ratio of 0.5:1 PDN:PAG eliminated these bridging defects, but not line broadening. Increasing the amount of PDN further to a ratio of 1:1 appears to successfully resolve lines at the correct line widths.

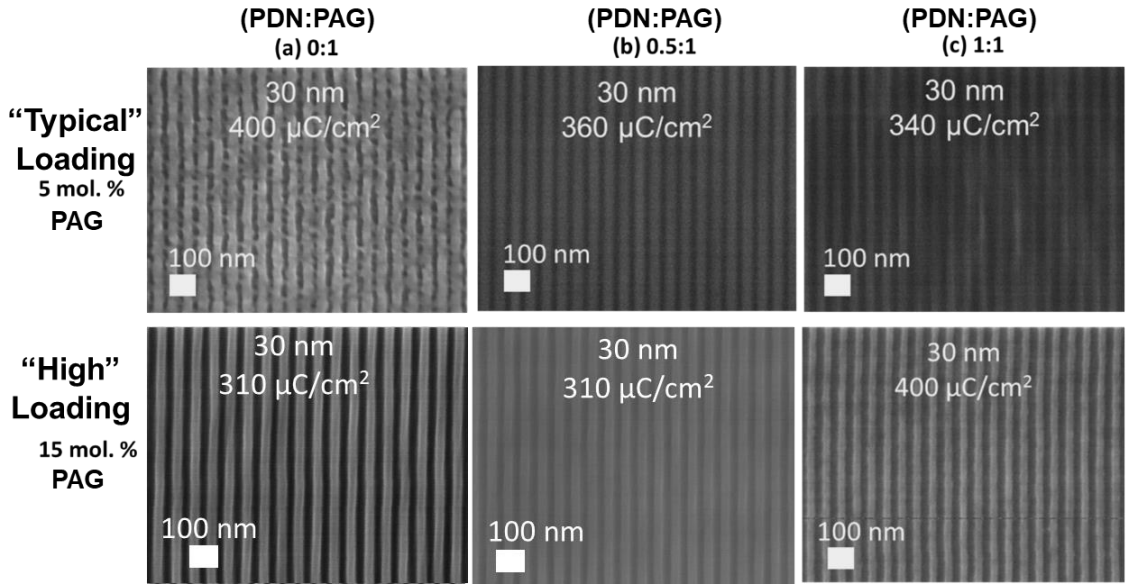

Figure 3.14 30 nm line:space patterns imaged using 5 or 15 mol. % TPS-OH-SbF_6 (PAG) and varying amounts of TPS-OH-Tf, (PDN) reported as a molar ratio of PDN to PAG (PDN:PAG).

At "high" 15 mol. % PAG loading and no PDN, bridging defects were eliminated and no pattern collapse was observed despite having an aspect ratio twice that of the blend containing 5 mol. % PAG. Line broadening was also eliminated at all amounts of PDN added including in the blend with just 15 mol. % PAG. These results suggest that functionalizing the PAG with phenols can provide enough inherent crosslinking control when used at high loadings to improve the resolution of 4-Ep and other epoxide resists without the need for an additional PDN additive. Two of these "high" loading resist blends (0:1 and 0.5:1 PDN:PAG) were chosen for further patterning studies to investigate their ultimate resolution by patterning small 1:1 line/space patterns with line widths ranging from 5-100 nm in 5 nm increments (Figure 3.15).

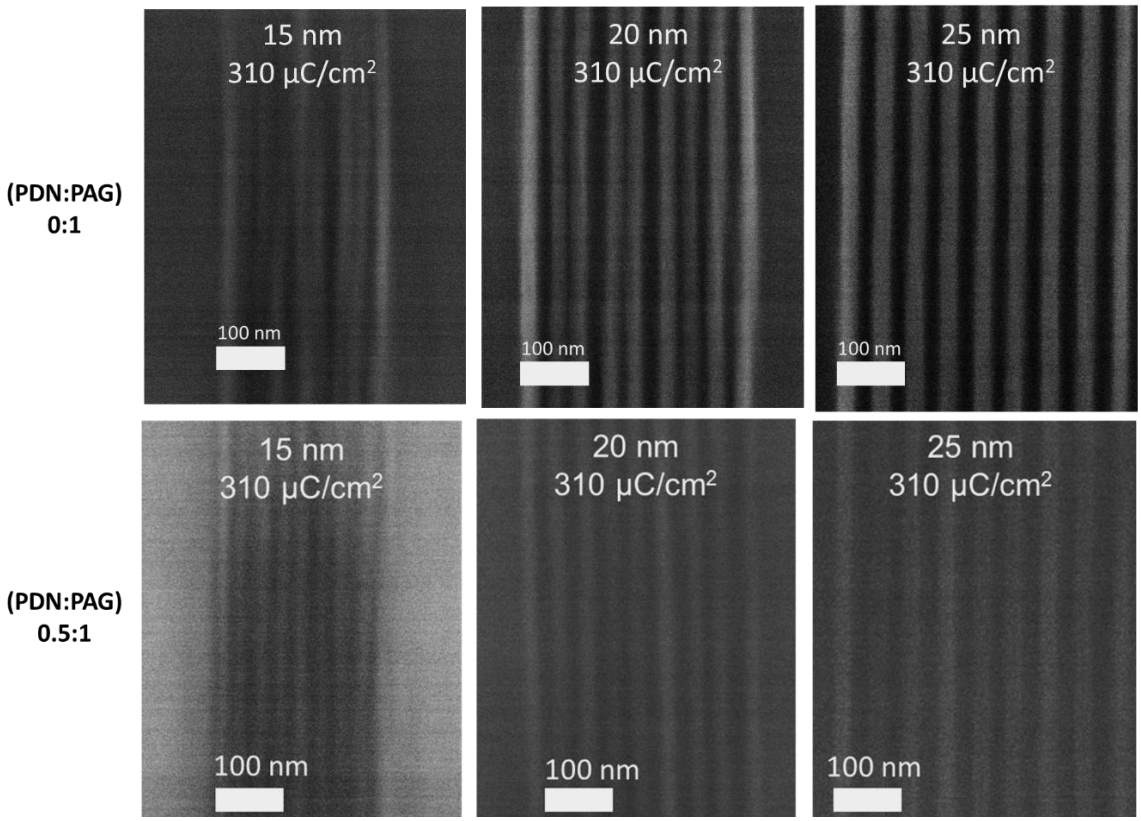

Figure 3.15 100 keV e-beam lithography high resolution 1:1 (line:space) patterns of 4-Ep using 15 mol. % TPS-OH-SbF_6 PAG and 0:1 or 0.5:1 PDN:PAG.

Resist blends without PDN successfully imaged 25 nm lines, but patterns at 20 nm and below failed apparently due to pattern collapse. The addition of a small amount of PDN (0.5:1 PDN:PAG) improved resolution and features down to 15 nm were resolved with no observed pattern collapse or bridging defects. It is extremely interesting that pattern collapse was mitigated simply through the addition of PDN. Previous work by Crivello and Ortiz reported that phenols could be used to increase the extent of conversion of a photopolymerized epoxide network, as the chain-transfer mechanism mobilized the propagating species which would have otherwise been trapped in the glassy matrix of the cross-linked network.[12] A higher extent of conversion could increase the mechanical

modulus of the patterned features which would explain the greater resistance to pattern collapse. If this is in fact the explanation for the change in behavior, then phenol-functionalized additives can potentially be used to simultaneously improve resistance to pattern collapse and resolution in epoxide molecular resists.

3.4 Summary and Conclusions

Two additives, a photoacid generator (TPS-OH-SbF_6) and a photodecomposable nucleophile (TPS-OH-Tf), were synthesized with phenol functional groups in the expectation that they could be used to improve the resolution of chemically amplified negative tone epoxide resists by some combination of 1) slowing the rate of cross-linking in unexposed regions via the introduction of a new polymerization pathway and 2) slowing the rate of cross-linking in unexposed regions by increasing the film T_g without requiring the structural modification of the resists themselves. These additives were found to slow the overall rate of cross-linking and reduce the sensitivity of a model epoxide resist (4-Ep) when using both DUV (298 nm) and 100 keV e-beam exposure sources, and demonstrated reduced acid generation efficiency when using 100 keV e-beam lithography. Phenol functionalized additives were not found to significantly affect the T_g of the resist at any of the loadings investigated, and the slower rate of cross-linking was attributed to the addition of the additional phenol-epoxide chain-transfer like cross-linking mechanism. E-beam sensitivity and NRT improvements were achieved by increasing the PAG loading to 15 mol. %.

At 5 mol. % loading, simply functionalizing the PAG with phenolic groups did not provide enough polymerization control to resolve 30 nm lines which failed due to bridging

defects. At 15 mol. % loading the resolution of 4-Ep was improved down to 25 nm half-pitch features without the use of PDN, but smaller features were unable to be resolved due to pattern collapse. The addition of PDN at a ratio of 1:2 PDN:PAG improved the resolution down to 15 nm half-pitch features while 10 nm half-pitch features failed to resolve either due to pattern collapse and/or line broadening. This improved pattern collapse behavior was attributed to a greater extent of conversion/cross-linking in the resist enabled by the high concentration of phenols. These additives show promise in improving the resolution in a variety of resists base on the photoacid initiated polymerization of epoxides.

3.5 References

1. Lawson, R. A., Lee, C. T., Yueh, W., Tolbert, L. and Henderson, C. L., Epoxide functionalized molecular resists for high resolution electron-beam lithography. *Microelectron Eng* **2008,** *85* (5-6), 959-962.

2. Pawloski, A. R., Christian and Nealey, P. F., The multifunctional role of base quenchers in chemically amplified photoresists. *Chem Mater* **2002,** *14* (10), 4192-4201.

3. Lawson, R. A., Chun, J. S., Neisser, M., Tolbert, L. M. and Henderson, C. L., Methods of controlling cross-linking in negative-tone resists. *Advances in Patterning Materials and Processes Xxxi* **2014,** *9051*.

4. Dusek, K., Diffusion control in the kinetics of cross-linking. *Polym Gels Netw* **1996,** *4* (5-6), 383-404.

5. Sharp, B., Lawson, R. A., Fralick, A., Narcross, H., Chun, J. S., Neisser, M., Tolbert, L. M. and Henderson, C. L., Base developable negative-tone molecular resist based on epoxide cross-linking. *Proc Spie* **2015,** *9425*.

6. Kozawa, T. and Tagawa, S., Radiation Chemistry in Chemically Amplified Resists. *Jpn J Appl Phys* **2010,** *49* (3).

7. Lawson, R. A., Noga, D. E., Tolbert, L. M. and Henderson, C. L., Nonionic photoacid generator behavior under high-energy exposure sources. *J Micro-Nanolith Mem* **2009,** *8* (4).

8. Grzeskowiak, S., Narasimhan, A., Rebeyev, E., Joshi, S., Brainard, R. L. and Denbeaux, G., Acid Generation Efficiency of EUV PAGs via Low Energy Electron Exposure. *J Photopolym Sci Tec* **2016,** *29* (3), 453-458.

9. Endo, M. and Tagawa, S., Theoretical Study of Photoacid Generators for Extreme Ultraviolet Resist. *Jpn J Appl Phys* **2011,** *50* (6).

10. Endo, M. and Tagawa, S., Calculated reactivity analysis of photoacid generators for EUV resist. *Advances in Resist Materials and Processing Technology Xxviii* **2011,** *7972*.

11. Narcross, H., Sharp, B. L., Tolbert, L. M. and Henderson, C. L., Crosslinkable photoacid generators for ultrahigh loading in epoxide functionalized molecular resists. *J Vac Sci Technol B* **2017,** *35* (6).

12. Crivello, J. V. and Ortiz, R. A., Benzyl alcohols as accelerators in the photoinitiated cationic polymerization of epoxide monomers. *J Polym Sci Pol Chem* **2002,** *40* (14), 2298-2309.

CHAPTER 4. EFFECT OF RESIST STRUCTURE ON GLASS TRANSITION TEMPERATURE AND LITHOGRAPHIC PERFORMANCE OF NEGATIVE TONE EPOXIDE RESISTS

4.1 Introduction

The diffusion of photoacids generated during exposure in chemically amplified resists (CARs) is a process that affects almost all patterning metrics including line edge roughness (contributed to by the statistical distribution of photoacids during and after diffusion) and perhaps most critically resolution.[1] Resolution loss due to photoacid diffusion is caused by the catalysis of solubility switching reactions outside of exposed areas and is a critical issue for next-generation lithography techniques such as e-beam and extreme ultraviolet (EUV) lithography.

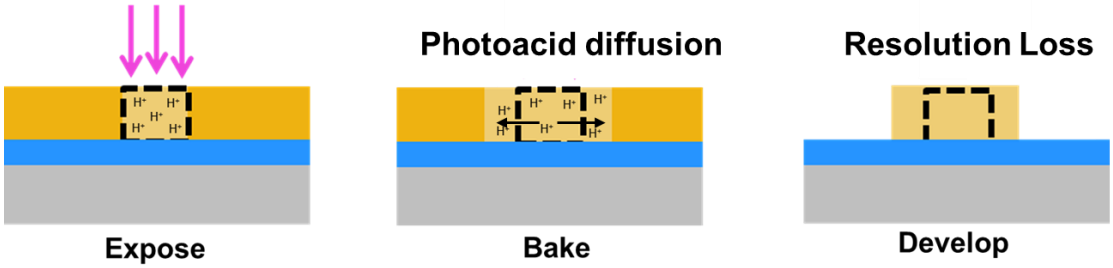

Figure 4.1 Illustration of resolution loss caused by photoacid diffusion where resolved features are larger than the original exposed area.

Significant research has been conducted to develop methods of controlling the photoacid diffusion length, including polymer bound photoacid generators (PBPs) and the use of photoacids with bulkier anions.[2-4] One of the potential benefits of negative tone

epoxide resists is their intrinsic diffusion control of the spatial extent of the solubility switching mechanism (cross-linking) as unlike conventional CARs, the active species is the cationic oxonium ion on the end of the growing polymer chain instead of a small-molecule photoacid.[5] This is due to the short lifetime of the photoacid which initiates polymerization and is typically not regenerated (Figure 4.2).

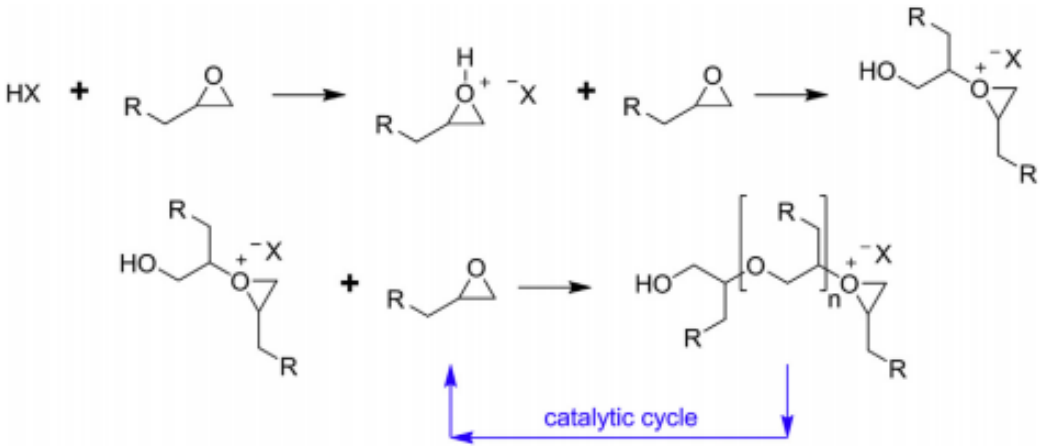

Figure 4.2 Cationic ring-opening polymerization mechanism of an epoxide functionalized resist.

The extent of polymerization is controlled by the ability of the active chain ends to diffuse through the resist as it undergoes cross-linking, As polymerization precedes, the mobility of the chain ends rapidly decreases and the rate of reaction becomes controlled by the ability of the active site to diffuse into a reaction volume.[6] Despite this inherent diffusion control, the polymerization front can still propagate outside of exposed regions while chain mobility is still high and cause line broadening or bridging defects.[7] Controlling the diffusion rate of cross-linking is just as critical to the resolution of these resists as controlling the photoacid diffusion length is to conventional CARs, but as previously discussed in Chapter 2, established methods of controlling photoacid diffusion

such as base quencher do not necessarily apply to negative tone epoxide resists.[5] In CARs, increasing the T_g of the resin has been found to decrease the acid diffusion length. The diffusion rate of chain ends during the cross-linking of epoxides should similarly be affected by the T_g of the resist. Some previous work has suggested that epoxide resists with higher glass transition temperatures had lower diffusion rates, but these results were complicated by the fact that this T_g increase was caused by the introduction of phenols onto the resist which can affect the rates of cross-linking by the addition of an additional chain-transfer like phenol-epoxide cross-linking pathway. Additionally, the degree of functionalization was changed which can also affect the network structure and cross-linking behavior making it difficult to determine the effect of just the resist T_g on cross-linking.[5, 8, 9]

The goal of this chapter was to investigate how the T_g of a resist could be influenced structurally without introducing any other variables such as the degree of functionality or alternative cross-linking pathways and how strong (if any) of an effect T_g had on cross-linking behavior and high-resolution patterning. This information would be extremely useful when attempting to rationally design second-generation resists. A set of 2-functional epoxide resists were proposed, systematically replacing methyl groups on the resist core with aromatic rings with the intent that this would restrict molecular motion and increase the T_g (Figure 4.3). A resist was also investigated where two of the aromatic rings on the resist core were covalently bonded together in the expectation that this would also restrict molecular motion and raise the T_g. Based on previous results, the changes in molecular weight resultant from the proposed structural modifications is not expected to meaningfully contribute towards changes in the T_g.[10]

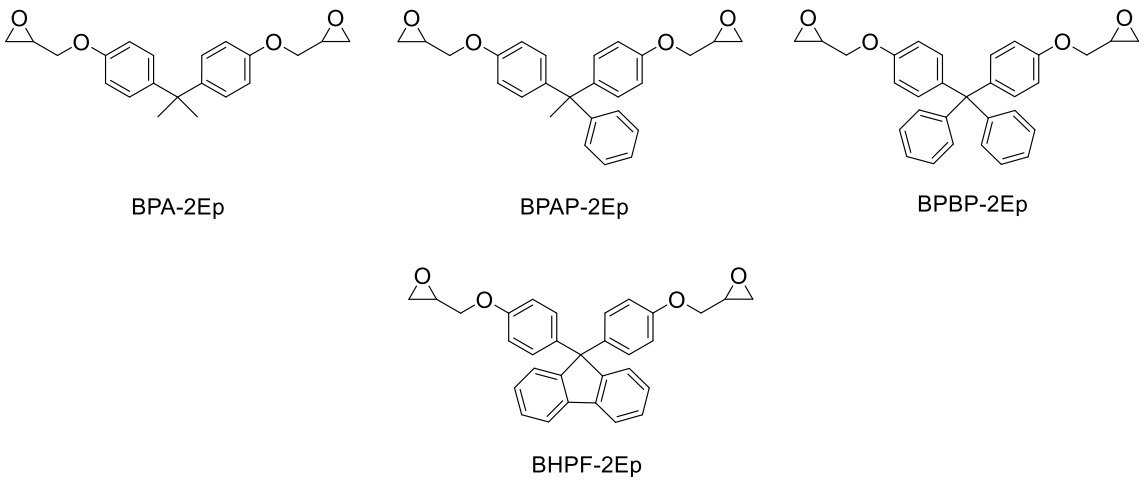

Figure 4.3 Structures of the 2-functional resists investigated in this study.

All of these resists (with the exception of BHPF-2Ep) were unable to form high quality smooth, pinhole free films making it difficult to truly determine trends in cross-linking and patterning behavior, so a second series of 4-functionalized compounds were investigated. It was previously observed that the incorporation of methyl groups onto the aromatic rings of a small organic molecule photoacid generator (PAG) increased its glass transition temperature significantly[11] which was attributed to the restriction of rotational motion of the molecule[12], so a similar analogue to a previously studied epoxide resist (TPOE-4Ep) was synthesized and studied (Figure 4.4).

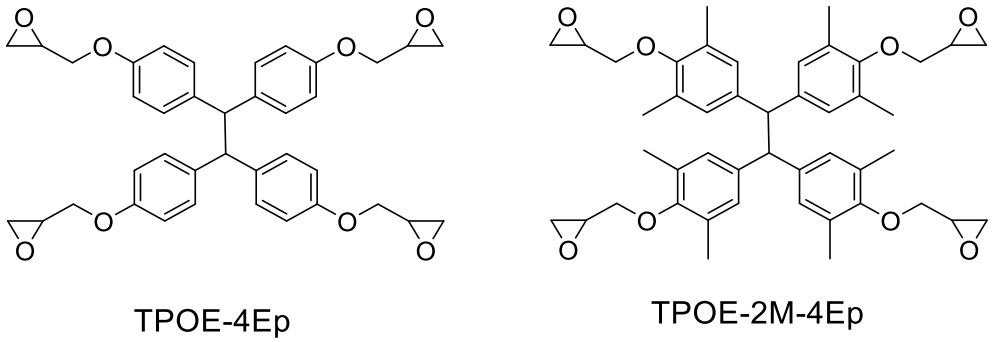

Figure 4.4 Structures of the 4-functional resists investigated in this study.

4.2 Experimental

4.2.1 Materials and Methods

All reagents unless otherwise noted were purchased from TCI America, Alfa-Aesar, or Sigma-Aldrich and used without further purification. TPS-SbF_6 was purchased from Midori-Kagura. Film thicknesses and glass transition temperatures were measured using a M-2000 Woolam Ellipsometer along with a TA Instruments DSC Q2000. Contact angle measurements were taken with an AST VCA-2500XE contact angle system. Resist solutions were prepared using 2 wt. % solids and 5 mol. % TPS-SbF_6 in ethyl lactate. ^{1}H NMR spectra were collected with a Varian Mercury Vx 300 spectrometer. Deep Ultraviolet (DUV) exposures were performed with an Oriel Instruments 500 W Hg-Xe arc lamp using a 248 nm bandpass filter. EUV evaluation was performed using the Micro Exposure Tool (MET) at the Lawrence Berkeley National Lab Advanced Light Source. E-beam exposures and patterning were performed with a JEOL JBX-9300FS and an Elionix ELS-G100 electron beam lithography system, using an acceleration voltage of 100 keV, a 100 pA current, and a 2 nm shot pitch. Film thicknesses for e-beam contrast curves were measured

using a Tencor KLA P15 Profilometer. Exposed wafers were imaged using a Carl Zeiss Ultra 60 scanning electron microscope (SEM) with 2 keV acceleration voltage.

4.2.2 Synthesis of BPA-2Ep

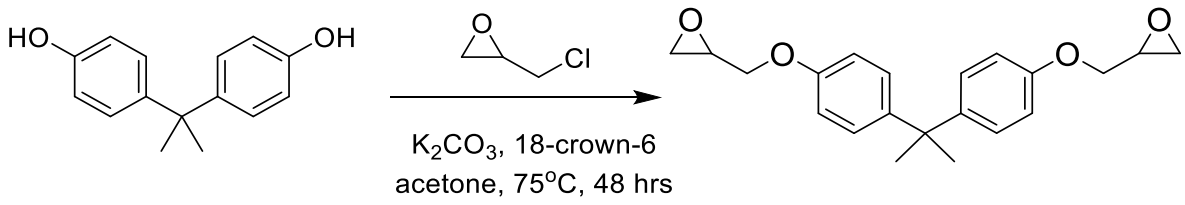

Figure 4.5 Synthetic scheme for BPA-2Ep.

4,4'-(propane-2,2-diyl)diphenol (5.00 g, 21.90 mmol, 1.00 equiv.), K_2CO_3 (9.08 g, 65.7 mmol, 3.00 equiv.), and a catalytic amount of 18-crown-6 (0.10 g, 0.38 mmol) were added to a 100 mL round bottom flask containing 50 mL of acetone. Epichlorohydrin (20.26 g, 219.2 mmol, 10.0 equiv.) was added dropwise, and the reaction was refluxed while stirring at 75 °C for 48 hours. The reaction was then cooled to room temperature and 25 mL each of dichloromethane (DCM) and deionized (DI) water were added and stirred. The organic layer was separated and washed three times with DI water, dried over $MgSO_4$, and excess solvent was removed via rotary evaporation. The product was purified via silica gel chromatography to give BPA-2Ep, a white viscous liquid. ^{1}H NMR (300 MHz $CDCl_3$) δ (ppm): 7.12 (d, J = 6.6, 4H), 6.83 (d, J = 6.6, 4H), 4.18 (dd, J = 11.1, 2H), 3.95 (dd, J = 11.1, 2H), 3.35 (m, 2H), 2.90 (dd, J = 4.5, 2H), 2.74 (dd, J = 4.9, 2H), 1.63 (s, 6H). Yield: 69 %.

4.2.3 Synthesis of BPAP-2Ep

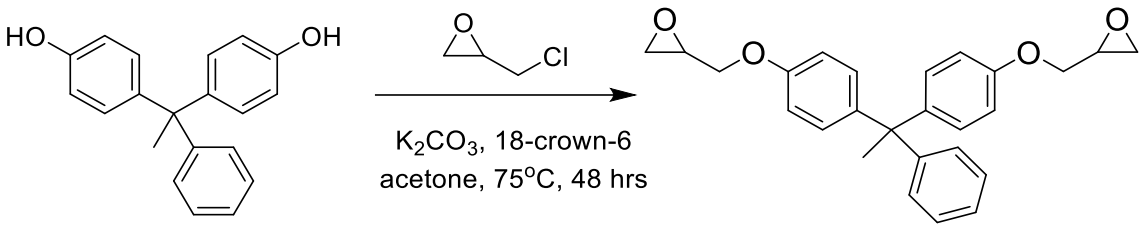

Figure 4.6 Synthetic scheme for BPAP-2Ep.

4,4'-(1-phenylethane-1,1-diyl)diphenol (5.00 g, 17.22 mmol, 1.00 equiv.), K_2CO_3 (7.14 g, 51.66 mmol, 3.00 equiv.), and a catalytic amount of 18-crown-6 (0.10 g, 0.38 mmol) were added to a 100 mL round bottom flask containing 50 mL of acetone. Epichlorohydrin (15.93 g, 172.20 mmol, 10.0 equiv.) was added dropwise, and the reaction was refluxed while stirring at 75 °C for 48 hours. The reaction was then cooled to room temperature and DCM and deionized DI water were added and stirred. The organic layer was separated and washed three times with DI water, dried over $MgSO_4$, and excess solvent was removed via rotary evaporation. The product was purified via silica gel chromatography to give BPAP-2Ep, a white viscous liquid. ^{1}H NMR (300 MHz $CDCl_3$) δ(ppm): 7.22 (m, 3H), 7.09 (d, J = 1.5, 2H), 6.99 (d, J = 9.0, 4H), 4.19 (dd, J = 11.1, 2H), 3.95 (dd, J = 11.0, 2H), 3.34 (m, 2H), 2.90 (dd, J = 4.8, 2H), 2.75 (dd, J = 4.8, 2H), 2.172 (s, 3H). Anal. Calcd for $C_{26}H_{26}O_4$: C, 77.59; H, 6.51. Found: C, 76.89; H, 6.62. Yield: 53 %.

4.2.4 Synthesis of BPBP-2Ep

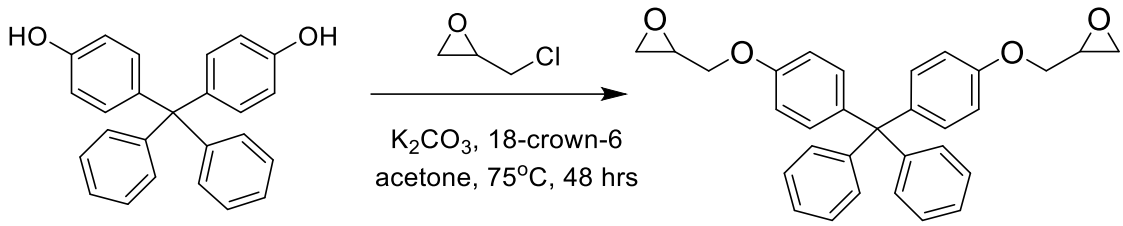

Figure 4.7 Synthetic scheme for BPBP-2Ep.

4,4'-(diphenylmethylene)diphenol (5.00 g, 14.19 mmol, 1.00 equiv.), K_2CO_3 (5.88 g, 42.56 mmol, 3.00 equiv.), and a catalytic amount of 18-crown-6 (0.10 g, 0.38 mmol) were added to a 100 mL round bottom flask containing 50 mL of acetone. Epichlorohydrin (13.13 g, 141.87 mmol, 10.0 equiv.) was added dropwise, and the reaction was refluxed while stirring at 75 °C for 48 hours. The reaction was then cooled to room temperature and DCM and DI water were added and stirred. The organic layer was separated and washed three times with DI water, dried over $MgSO_4$, and excess solvent was removed via rotary evaporation. The product was purified via two successive re-precipitations in a 2:1 ethanol/DI water solution to give BPBP-2Ep, a white powder. ^{1}H NMR (300 MHz $CDCl_3$) δ (ppm): 7.22 (m, 10H), 7.08 (d, J = 8.7, 4H), 6.79 (d, J = 8.7, 4H), 4.18 (dd, J = 11.1, 2H), 3.94 (dd, J = 10.8, 2H), 3.34 (m, 2H), 2.90 (dd, J = 4.5, 2H), 2.74 (dd, J = 4.8, 2H). MS *m/z* (relative intensity): 464.2 (100.0%), 465.2 (33.7%), 466.21 (5.6%). Anal. Calcd for $C_{31}H_{28}O_4$: C, 80.15; H, 6.08. Found: C, 78.40; H, 6.25. Yield: 59 %.

4.2.5 Synthesis of BHPF-2Ep

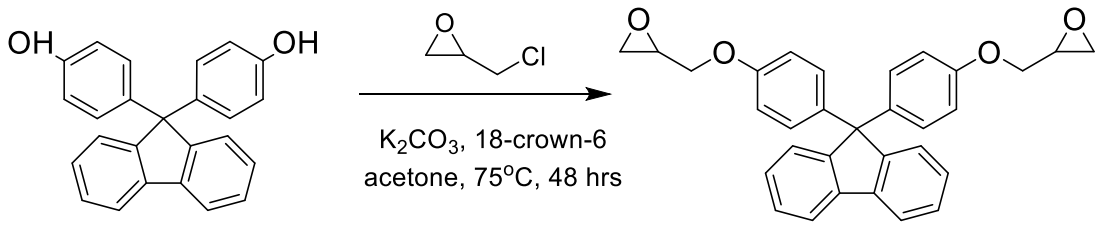

Figure 4.8 Synthetic scheme for BHPF-2Ep.

4,4'-(9H-fluorene-9,9-diyl)diphenol (5.0 g, 14.3 mmol, 1.0 equiv.), K_2CO_3 (5.9 g, 42.8 mmol, 3.0 equiv.), and a catalytic amount of 18-crown-6 (0.1 g, 0.4 mmol) were added to a 100 mL round bottom flask containing 50 mL of acetone. Epichlorohydrin (13.2 g, 142.7 mmol, 10.0 equiv.) was added dropwise, and the reaction was refluxed while stirring at 75 °C for 48 hours. The reaction was then cooled to room temperature and 25 mL each of DCM and DI water were added and stirred. The organic layer was separated and washed three times with DI water, dried over $MgSO_4$, and excess solvent was removed via rotary evaporation. The product was purified via two successive re-precipitations in a 3:1 methanol/DI water solution to give 2,2'-((((9H-fluorene-9,9-diyl)bis(4,1-phenylene))bis(oxy))bis(methylene))bis(oxirane) (BHPF-2Ep), a white powder. ^{1}H NMR (300 MHz $CDCl_3$) δ (ppm): 7.74 (dd, J = 7.1, 2H), 7.30 (m, 6H), 7.10 (d, J = 9.0, 4H), 6.76 (d, J = 9, 4H), 4.14 (dd, J = 10.8, 2H), 3.90 (dd, J = 10.9, 2H), 3.30 (m, 2H), 2.87 (dd, J = 4.8, 2H), 2.71 (dd, J = 5.1, 2H). Anal. Calcd for $C_{31}H_{26}O_4$: C, 80.05; H, 5.67. Found: C, 79.34; H, 5.80. Yield: 61 %.

4.2.6 Synthesis of TPOE-2M-4Ep

4.2.6.1 Synthesis of TPOE-2M-4OH

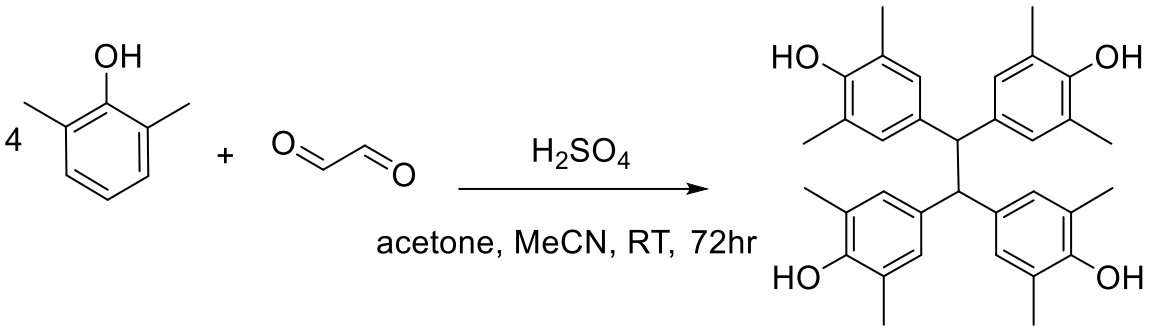

Figure 4.9 Synthetic scheme for TPOE-2M-4OH.

2,6-xylenol (25.0 g, 204.6 mmol, 5.2 equiv.), acetone (3.1 g, 53.4 mmol, 0.5 equiv.) and glyoxal (5.8 g, 100.0 mmol, 1.0 equiv.) were added to a 100 mL round bottom flask with 10 mL of acetonitrile (MeCN). Sulfuric acid (4.7 g, 4.7.9 mmol, 1.2 equiv.) was added drop-wise and the reaction was stirred vigorously at room temperature for 72 hours. The solution was precipitated into 50 mL of methanol and gravity filtered to isolate the solid crude product which washed an additional three times with methanol and dried under vacuum overnight to yield the product 4,4',4",4"'-(ethane-1,1,2,2-tetrayl)tetrakis(2,6-dimethylphenol), a white powder. ^{1}H NMR (300 MHz CD_3OD) δ (ppm): 6.71 (s, 8H), 4.37 (s, 2H), 3.34 (s, 24H). Yield: 67 %.

4.2.6.2 Synthesis of TPOE-2M-4Ep

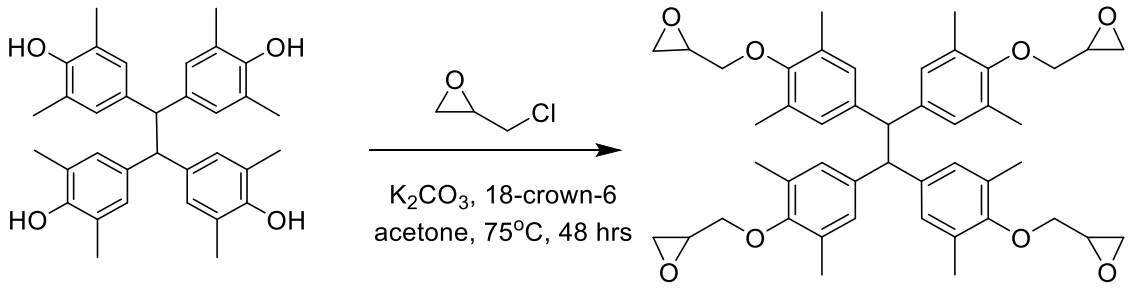

Figure 4.10 Synthetic scheme for TPOE-2M-4Ep.

TPOE-2M-4Ep (5.0 g, 9.8 mmol, 1.0 equiv.), K2CO3 (10.8 g, 78.3 mmol, 8.0 equiv.), and a catalytic amount of 18-crown-6 (0.1 g, 0.4 mmol) were added to a 100 mL round bottom flask containing 50 mL of acetone. Epichlorohydrin (18.1 g, 196.0 mmol, 20.0 equiv.) was added dropwise, and the reaction was refluxed while stirring at 75 °C for 48 hours. The reaction was then cooled to room temperature and 25 mL each of dichloromethane (DCM) and deionized (DI) water were added and stirred. The organic layer was separated and washed three times with DI water, dried over MgSO4, and excess solvent was removed via rotary evaporation. The product was purified via silica gel chromatography to give TPOE-2M-4Ep, a light yellow crystalline powder. 1H NMR (300 MHz CDCl3) δ (ppm): 6.70 (s, 8H), 4.37 (s, 2H), 3.89 (dd, J = 11.4, 4H), 3.63 (dd, J = 11.1, 4H), 3.28 (m, 4H), 2.84 (dd, J = 4.2, 4H), 2.63 (dd, J = 4.2, 4H), 2.11 (s, 24H). $[M + Na]^+$ calcd. for $C_{46}H_{54}O_8Na^+$ 757.380; found, 757.373. Yield: 2 %.

4.3 Results and Discussion

4.3.1 Effect of Structure on Glass Transition Temperature

Modulated Differential Scanning Calorimetry (MDSC) was used to measure the T_g of the 2-Functionalized compounds. This method was chosen over standard DSC as it has improved sensitivity for detecting weak signals (which is often the case for small molecules in DSC). The T_g for these uncrosslinked compounds was determined using the peak of the first derivative of the reversing heat flow signal in the third heat/cool cycle (an example of this calculation from the MDSC signal of BHPF-2Ep can be seen in Figure 4.11) and are summarized in Figure 4.12. As predicted, adding aromatic rings onto the resist resulted in an increase in T_g which was attributed to the restriction of molecular motion. Introducing

a covalent bond between two of the aromatic rings which should restrict the molecular motion even further was also found to increase the T_g of the resist, supporting this theory.

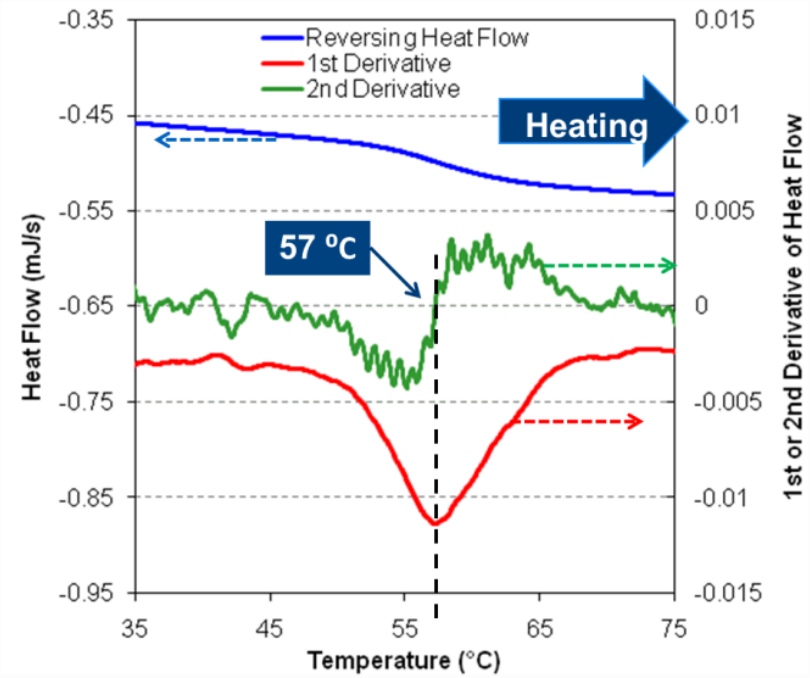

Figure 4.11 The first and second derivative to the reversing heat flow signal from MDSC used to determine the T_g of BHPF-2Ep.

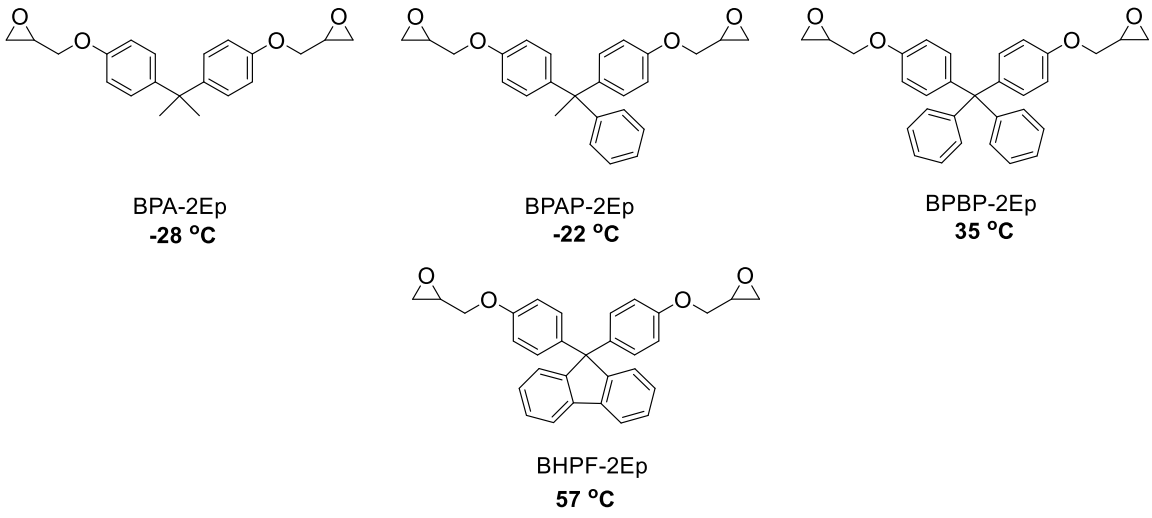

Figure 4.12 The 2-functionalized resists investigated and their uncrosslinked T_g values as measured by MDSC.

Due to the small amount of pure TPOE-2M-4Ep isolated, thin film ellipsometry was used to determine the T_g of TPOE-4Ep and TPOE-2M-4Ep. This method is described in more detail in Chapter 2, but briefly the film thickness is tracked over time as a function of temperature using a fixed heating rate of 8 °C/min. The temperature at which the coefficient of thermal expansion changes (indicated by a change in slope) is taken as the glass transition temperature. As predicted, methyl groups placed adjacent to the phenol/epoxide site on the aromatic rings increased the T_g of TPOE-4Ep from 43°C to 50 °C.

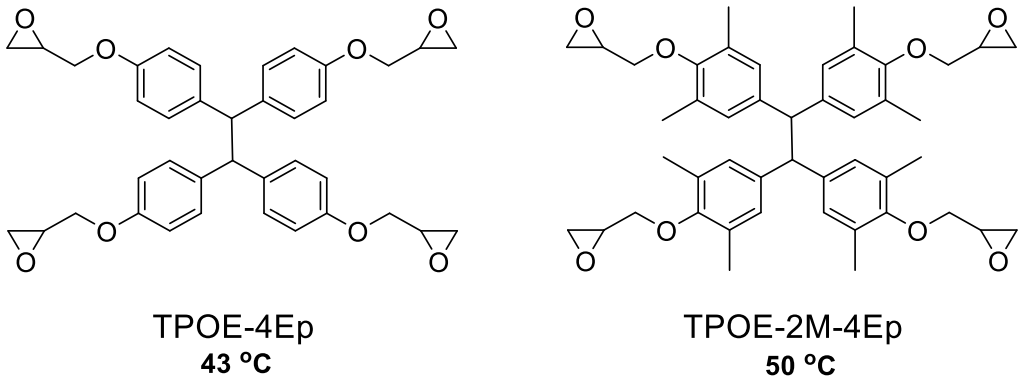

Figure 4.13 The 4-functionalized resists investigated and their T_g values as measured by thin film ellipsometry.

4.3.2 Film Quality

Being able to form smooth, even, defect-free films on substrates is a critical requirement of any photoresist. The most common application method of depositing photoresist is spin-coating. Solutions are made of photoresist in a volatile solvent, which is deposited in the centre of a wafer or wafer piece and spun rapidly. This spreads the liquid towards the edges and the casting solvent evaporates to leave a film of photoresist behind. If the photoresist has a poor surface energy match with the substrate, it can de-wet either

during spin-coating or when thermal energy is applied during the post apply or post exposure bake. Particles or capillary wave forces during coating can cause a break in the surface of the film to the substrate which is then pinned into place forming a so call pinhole defects. Films that de-wet completely from the substrate obviously cannot be used as photoresists, and films that have poor adhesion to the surface might have patterns that are more likely to de-wet during post-exposure processing or collapse due to a lack of adhesion. Unfortunately, all of the 2-functionalized resists with the exception of BHPF-2Ep de-wet to some extent from the silicon wafer substrates, which could be seen either as patchy or uneven films immediately following spin-casting and the formation of pinholes during the PAB. Water contact angle measurements (Table 2) do not appear to show any dramatic mismatch between the 2-functional materials and the silicon dioxide bare surface of the silicon wafer, and there was no correlation observed between contact angle and film quality. Indeed, the compound that de-wet to the greatest extent (BPBP-2Ep) did not have the highest contact angle mismatch with the naturally occurring silicon dioxide surface which forms on the surface of silicon wafers. Additionally, BHPF-2Ep coated far better than any of the other resists studied (BPAP-2Ep and BPA-2Ep) that had similar contact angles.

Table 2. Water contact angles of the compounds and substrates examined in this study.

Compound	Water Contact Angle (°)
BPA-2Ep	64
BPAP-2Ep	76
BPBP-2Ep	88
BHPF-2Ep	69
GT1 Underlayer	72
SO_2 Substrate	62

The number of pinhole defects have been shown to increase in thinner films due to the greater likelihood of capillary wave forces on the surface of the film during spinning making contact with the substrate to form a point of localized de-wetting. Resists with extremely low T_g values might contribute to the likelihood of this happening, which could help explain why BPAP-2Ep which is a viscous liquid at room temperature at room temperature coated so poorly. This cannot be the only explanation however, as BPA-2Ep had a lower T_g but had less dewetting/pinhole defects, and furthermore other small molecule epoxide photoresists have been functionalized with similar T_g values to BPBP-2Ep that were able to form high quality defect free films. A traditional adhesion promoter (HMDS) was applied to the silicon wafer in an attempt to improve adhesion but did not notably improve dewetting behaviour for any of the resists. An alternative underlayer design (Figure 4.14) was proposed that could directly cross-link with the epoxides in the resist during the PEB and improve film adhesion.

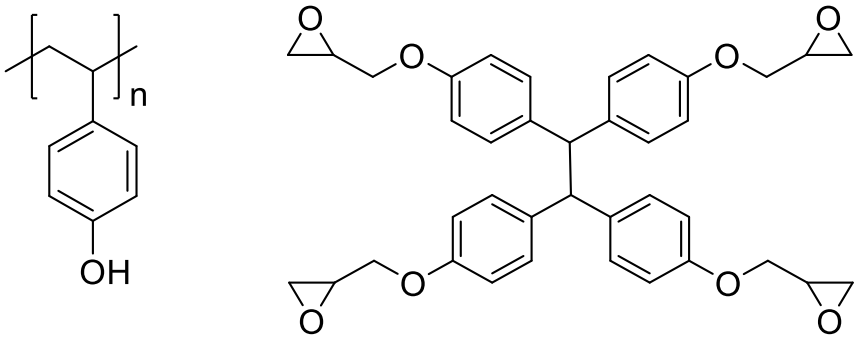

Figure 4.14 Cross-linkable (GT1) underlayer designed to promote adhesion of 2-functionalized resists.

Coating onto this underlayer improved adhesion issues, although some pinhole defects were still observed and BPAP-2Ep was patterned without a PAB as it would catastrophically dewet even on top of the GT1 underlayer. Since BHPF-2Ep coated with no issues, no underlayer was required.

Figure 4.15 Picture of BPAP-2Ep films coated on untreated silicon wafer piece (left) and adhesion promoting underlayer (right).

Both 4-functional materials naturally formed high quality defect free films. This might be attributed to their higher T_g values, but since there was no trend between T_g and

film quality in the 2-functionalized resists this is more likely caused by structural differences.

4.3.3 Effect of Glass Transition Temperature on Cross-linking Behaviour.

Before discussing the relationship between glass transition temperature and contrast curve behaviour for the synthesized resists, it is helpful to review the underlying kinetics of crosslinking in epoxide negative tone materials. Unlike conventional chemically amplified resists, the active species is the cationic oxonium ion on the end of the growing chain instead of a small molecule photoacid.[5] This is due to the short lifetime of the photoacid which initiates polymerization and is typically not regenerated. As polymerization proceeds, the mobility of the chain ends rapidly decreases and the rate of reaction becomes controlled by the ability of the active site to diffuse into a reaction volume.[6] This diffusion can be described by the diffusion coefficient (D_{eff}) as defined by Equation (4.1) where m is a constant which is fit to each resist material, T is the reaction temperature (or in this case the PEB temperature), $T_g(\alpha)$ is the T_g of the resist as a function of the extent of crosslinking or epoxide conversion, and T' is a constant of 50 K.[13]

$$D_{eff} = \exp\left[-\frac{m}{T \ln\left[\frac{T}{T_g(\alpha) - T'}\right]}\right] \tag{4.1}$$

$T_g(\alpha)$ can be further described by Equation

(4.2), where α is the extent of conversion of epoxides, T_{g0} is the T_g of the un-crosslinked resist, T_{g1} is the T_g of the fully cross-linked resist, and C is a constant of 2000 K.[13]

$$\frac{1}{T_g(\alpha)} = \frac{1-\alpha}{T_{g0}} + \frac{\alpha}{T_{g1}} + \frac{\alpha(1-\alpha)}{C} \tag{4.2}$$

Assuming that a higher T_{g0} value for a resist will result in a higher T_{g1} value, it can be observed that resists with higher T_{g0} values will have higher $T_g(\alpha)$ values at a given extent of conversion and subsequently a lower coefficient of diffusion. As polymerization proceeds the diffusivity of the active chain end should decrease due to the increase in the T_g of the resist as it crosslinks. Additionally, the lower the T_{g0} value of a resist is, the lower its bulk T_g will likely be at a given PEB temperature and subsequently the active chain ends should have a higher D_{eff}. The difference between the PEB temperature and the T_g of the un-crosslinked resists will be referred to as ΔT (ΔT = T – T_{g0}).

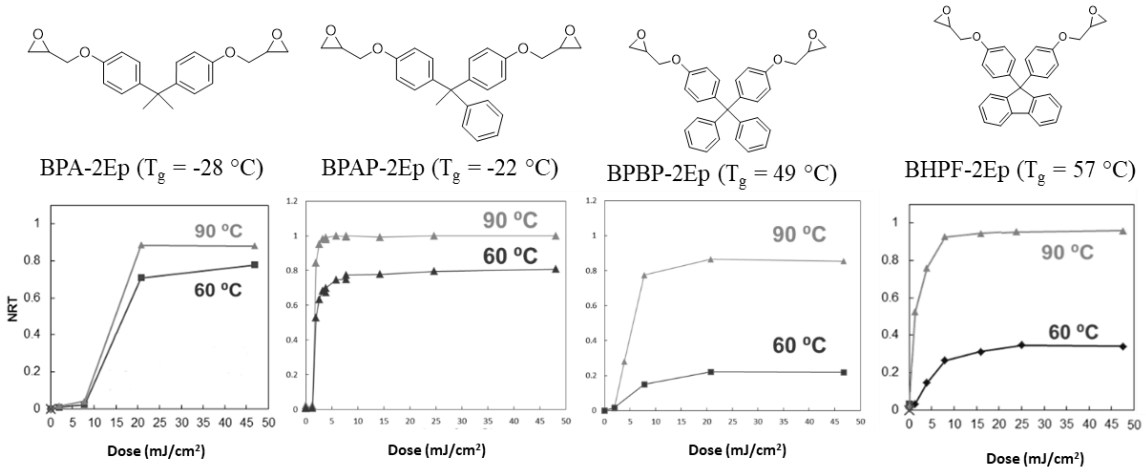

Figure 4.16 DUV contrast curves of the 2-functional resists on GT1 underlayer. All curves were collected using 5 mol.% TPS-SbF_6 as the PAG, a 2 minute 60 °C PAB and a 1 minute PEB at either 90 °C or 60 °C.

The effect of ΔT on cross-linking behaviour of the 2-functional resists can be seen in the difference between the DUV contrast curves of BPA-2Ep, BPAP-2Ep, and BPBP-2Ep in Figure 4.16. As the T_g of each resist increases, the ΔT at a given PEB temperature will decrease. Because a lower ΔT value generally leads to a lower diffusion coefficient, polymerization should propagate to a lesser degree in a given time frame due to the reduced mobility of the active sites. Accordingly, the NRT values for BPA-2Ep at both 90 ºC and 60 ºC PEB temperatures are lower than the NRT values of BPAP-2Ep which in turn had lower NRT values than BPBP-2Ep. BHPF-2Ep did not follow this trend and had a higher NRT, contrast, and sensitivity despite having a higher T_g. This indicates that T_g is not the only factor governing cross-linking behaviour. Since some previous results have shown that epoxide resists have better high-resolution patterning using higher doses and processed at lower temperatures, the data so far seemed to suggest that low T_g resists might be favourable for high-resolution patterning especially due to their excellent contrast.[14]

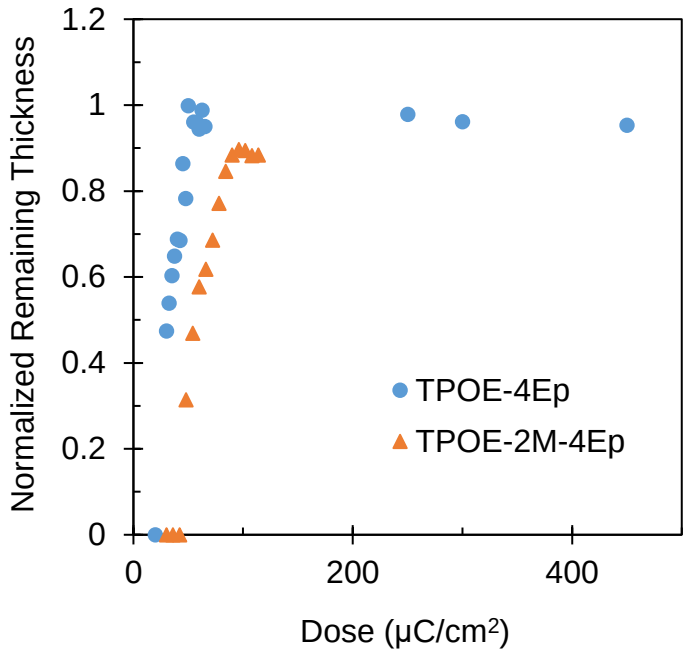

Figure 4.17 E-Beam contrast curves of TPOE-4Ep and TPOE-2M-4Ep. All curves were collected using 5 mol.% TPS-SbF_6, a 2 minute 60 °C PAB and a 1 minute 90 °C PEB.

The effect of ΔT on cross-linking behaviour of the 4-functional resists can be seen in the difference between the e-beam contrast curves of TPOE-4Ep and TPOE-2M-4Ep in Figure 4.17. Similar results to the cross-linking behaviour of most of the 2-functional resists were observed, where increasing the glass transition temperature of the resist by a modest 7 °C resulted in a lower NRT (from 1.0 to 0.9) and sensitivity (E_{100} from 62.5 to 90 μC/cm^2. This further illustrates how moderate structural changes can impact the cross-linking behaviour especially when post-exposure processing conditions (bake temperature and time) are kept the same.

4.3.4 Effect of Glass Transition Temperature on Lithographic Performance

High-resolution patterning of the 2-functional resists was performed using EUV lithography and showed some interesting consequences of using resists with low T_g values.

The resist with the lowest T_g (BPA-2Ep) was unable to resolve features at any dose and it appears that the entire region has been cross-linked (Figure 4.18 left). This suggests that while a low T_g can result in rapid cross-linking and high extent of conversion, the mobility of the propagating chain might be so high that there is rapid uncontrollable propagation of polymerization into unexposed regions. Another possibility is that the T_g was so low that partially cross-linked material could flow during the PEB and distorted the patterns. BPAP-2Ep was somewhat able to resolve lines (Figure 4.18 right), but with extensive bridging and/or pattern flow defects caused by the low T_g (as discussed previously).

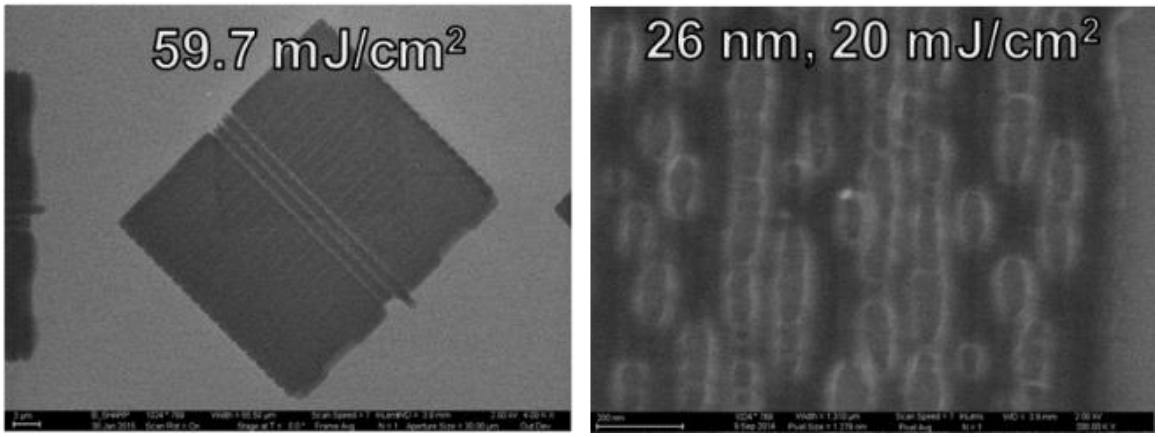

Figure 4.18 Lines patterned using EUV lithography of (left) BPA-2Ep and (right) BPAP-2Ep.

It is interesting to note the difference in the patterning performance between the resists BPBP-2Ep (Figure 4.19) and BHPF-2Ep (Figure 4.20). The structures of these two resists are extremely similar, differing only in a single bond connecting the two aromatic rings in BHPF-2Ep. Likewise, the T_g values are similar and differ by only 8 °C. BPBP-2Ep had much worse coating behaviour however and could only be coated without dewetting on the GT1 underlayer. Despite the use of this underlayer BPBP-2Ep line patterns appear

to have completely dewet/delaminated during development. Only at the highest exposed dose was any material observed, which is likely a residue of BPBP-2Ep cross-linked to the underlayer.

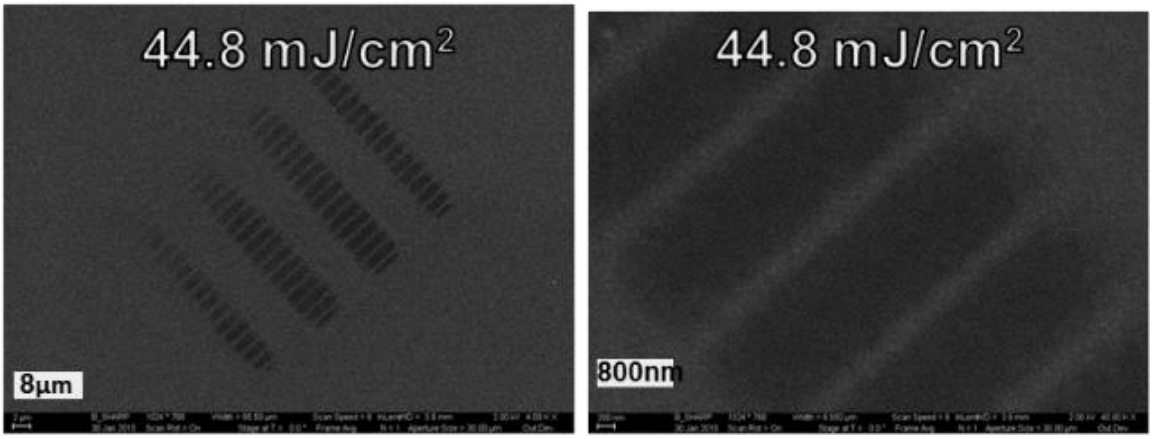

Figure 4.19 Cross-linked residue of BPBP-2Ep after the attempted EUV high resolution patterning.

BHPF-2Ep, however, formed high quality films and could resolve dense 1:1 line/space patterns down to 20 nm despite the small change in molecular structure.

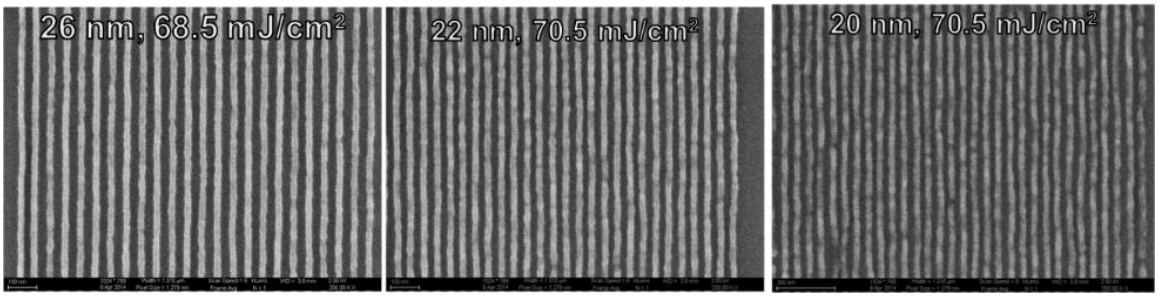

Figure 4.20 EUV high-resolution patterns of BHPF-2Ep at 26 nm L/S, 22 nm L/S, and 20 nm L/S.

High-resolution patterning of the 4-functional resists was obtained using e-beam lithography, and also showed surprisingly different behaviour despite extremely similar

structures and even contrast curves. TPOE-4Ep could resolve lines down to 35 nm (Figure 4.21) with a moderate E_{size} (dose required to resolve the desired feature) of 50 μC/cm^2. 35 nm lines of TPOE-2M-4Ep however were underdosed even at doses as high as 180 μC/cm^2 and required 330 μC/cm^2 to resolve (Figure 4.22).

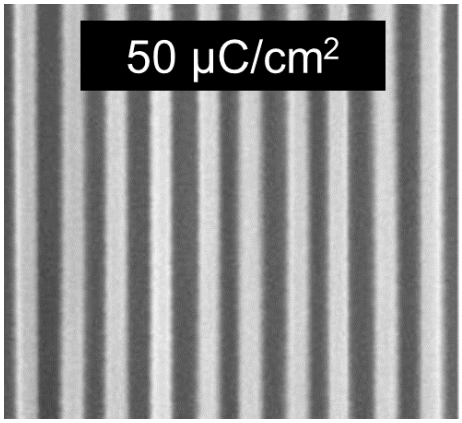

Figure 4.21 SEM images of 35 nm lines of TPOE-4Ep patterned using 100 keV e-beam lithography

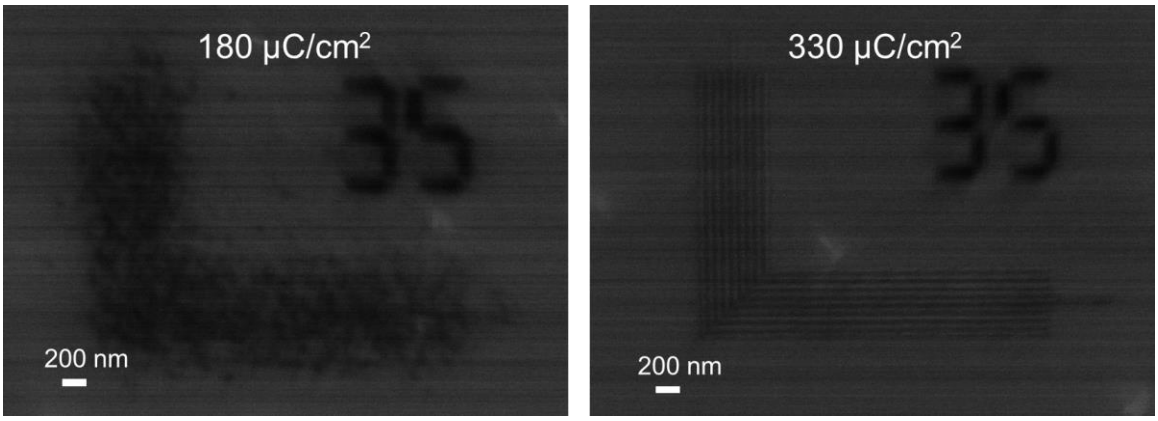

Figure 4.22 SEM images of 35 nm lines of TPOE-2M-4Ep patterned using 100 keV e-beam lithography.

4.4 Summary and Conclusions

A series of 2-functionalized negative tone epoxide functionalized molecular resists were synthesized and patterned using EUV lithography. A trend was observed where the introduction of aromatic rings to the core of each molecule and covalent bonds between these rings resulted in an increase in glass transition temperature of the un-crosslinked resist. These resists were generally found to have poor film stability and adhesion, which was partially overcome with the use of a specially designed underlayer capable of directly cross-linking with epoxide resists. A 4-functionalized negative tone epoxide functionalized molecular resist was also synthesized with methyl groups flanking the epoxide site which was also found to increase the glass transition temperature.

With the exception of one resist, BHPF-2Ep, a trend was observed where increasing the T_g of the resist lowered the sensitivity and NRT when using identical post-exposure processing conditions (bake temperature and time) which was attributed to a lower diffusion coefficient of the active chain end whose mobility is required for the propagation of polymerization. Resists with the lowest T_g values demonstrated the most promising cross-linking behaviour (as measured by dose-response curves) having the largest NRT, sensitivity, and contrast, but the high-resolution patterning of resists with very low (below room temperature) T_g values were found to fail due to some combination of propagation of polymerization outside of exposed regions due an increase in the diffusion coefficient of polymerizing chain ends and/or the flow of partially cross-linked patterns during the PEB step.

While trends in sensitivity and NRT as a function of resist T_g were observed, the relationship between T_g and patterning performance proved to be more complex with moderate structural changes resulting in radically different patterning performances. The

most extreme example of this was the difference between BPBP-2Ep and BHPF-2Ep which had identical structures with the exception of a covalent bond linking two of the aromatic rings together in BHPF-2Ep. BPBP-2Ep could not successfully resolve any features due to adhesion issues, whereas BHPF-2Ep was capable of resolving 20 nm features using EUV lithography. Similarly, TPOE-4Ep and TPOE-2M-4Ep required extremely different E_{size} (50 vs. 330 μC /cm^2) to resolve 35 nm lines despite dose-response curves that suggested only a moderate (~10 μC cm^2) difference in sensitivity. These results provide some methods for modifying the T_g of molecular resists but the relationship between these methods and their effect on the final network structure and patterning performance is complex and does not follow any obvious trends.

4.5 References

1. Lee, C.-T., Lawson, R. A. and Henderson, C. L., Understanding the effects of photoacid distribution homogeneity and diffusivity on critical dimension control and line edge roughness in chemically amplified resists. *Journal of Vacuum Science & Technology B: Microelectronics and Nanometer Structures Processing, Measurement, and Phenomena* **2008,** *26* (6), 2276-2280.

2. Gronheid, R., Pret, A. V., Rathsack, B., Hooge, J., Scheer, S., Nafus, K., Shite, H. and Kitano, J., *EUV RLS performance tradeoffs for a polymer bound PAG resist*. SPIE: 2010; Vol. 7639, p 9.

3. Wang, M., D. Jarnagin, N., Yueh, W., Roberts, J., Tapia-Tapia, M., Batina, N. and Gonsalves, K., *Novel polymeric anionic Photoacid Generators (PAGs) and photoresists for sub-100 nm patterning by 193 nm lithography*. 2007; Vol. 6519.

4. Kang, S. H., Wu, W. L., Choi, K. W., De Silva, A., Ober, C. K. and Prabhu, V. M., Characterization of the Photoacid Diffusion Length and Reaction Kinetics in EUV Photoresists with IR Spectroscopy. *Macromolecules* **2010,** *43* (9), 4275-4286.

5. Lawson, R. A., Chun, J. S., Neisser, M., Tolbert, L. M. and Henderson, C. L., Methods of controlling cross-linking in negative-tone resists. *Advances in Patterning Materials and Processes Xxxi* **2014,** *9051*.

6. Matsuoka, S., Quan, X., Bair, H. E. and Boyle, D. J., A model for the curing reaction of epoxy resins. *Macromolecules* **1989,** *22* (10), 4093-4098.

7. Lawson, R. A., Lee, C. T., Yueh, W., Tolbert, L. and Henderson, C. L., Epoxide functionalized molecular resists for high resolution electron-beam lithography. *Microelectron Eng* **2008,** *85* (5-6), 959-962.

8. Sharp, B. L., Narcross, H. L., Ludovice, P., Tolbert, L. M. and Henderson, C. L., Structural effects on the performance of epoxide-based negative-tone molecular resists. *J Vac Sci Technol B* **2019,** *37* (1).

9. Sharp, B., Lawson, R. A., Fralick, A., Narcross, H., Chun, J. S., Neisser, M., Tolbert, L. M. and Henderson, C. L., Base developable negative-tone molecular resist based on epoxide cross-linking. *Proc Spie* **2015,** *9425*.

10. Sharp, B. Materials for Next-Generation Lithography: Crosslinked Molecular Resists and Photopatternable Underlayers. Georgia Institute of Technology, 2018.

11. Narcross, H., Sharp, B. L., Ludovice, P. J., Tolbert, L. M. and Henderson, C. L., Phenol-functionalized polymerization control additives for negative tone epoxide crosslinking molecular resists. *J Vac Sci Technol B* **2018,** *36* (6).

12. Kim, Y. S., Kim, J. H., Kim, J. S. and No, K. T., Prediction of Glass Transition Temperature (Tg) of Some Compounds in Organic Electroluminescent Devices with Their Molecular Properties. *Journal of Chemical Information and Computer Sciences* **2002,** *42* (1), 75-81.

13. Dusek, K., Diffusion control in the kinetics of cross-linking. *Polym Gels Netw* **1996,** *4* (5-6), 383-404.

14. Lawson, R. Molecular Resists for Advanced Lithography - Design, Synthesis, Characterization, and Simulation. Georgia Institute of Technology, 2011.

CHAPTER 5. NON CHEMICALLY-AMPLIFIED PHOTODEFINABLE UNDERLAYER FOR THE DIRECTED SELF-ASSEMBLY OF BLOCK COPOLYMERS

5.1 Introduction

Maintaining Moore's Law using current photolithographic sources such as 193 and 193i has required the development and use of increasingly complex and expensive multiple patterning techniques such as double, triple, and even quadruple patterning and are rapidly approaching their limit in terms of feasible feature size.[1-3] Alternative light/energy sources such as EUV and multibeam EBL have the ability to achieve smaller pitch patterning without the need for these complex steps, but issues such as inefficient power sources, low throughput, and a lack of suitable photoresists currently prevents their widescale implementation in manufacturing. As such, there is significant interest in alternative patterning technologies which can either extend the use of current 193i nm optical lithographic systems or be used complementarily with next generation lithography techniques. One such technology, the directed self-assembly (DSA) of block copolymers (BCPs), takes advantage of the natural ability of certain block copolymers to microphase separate into periodic well-ordered domains in a variety of morphologies with pitches ranging from just a few to hundreds of nanometers (depending on the volume fraction, molecular weight, and block composition of the BCP).[4] Since some of these morphologies resemble architectures commonly used in lithography, specifically cylinders and lamellae (Figure 5.1), DSA is being explored as an option to meet the requirements of future manufacturing nodes. These microstructures can be transferred onto the substrate by

selectively removing one of the polymer domains typically through etching, and the remaining relief pattern can then be transferred onto the substrate through etch processing. Achieving the desired patterns with long-range order, low defectivity, and correct alignment relative to the substrate requires some method of guiding the BCP phase separation process, typically by means of a topographically[5] (graphoepitaxy) or chemically[6] (chemoepitaxy) patterned underlayer (Figure 5.1).

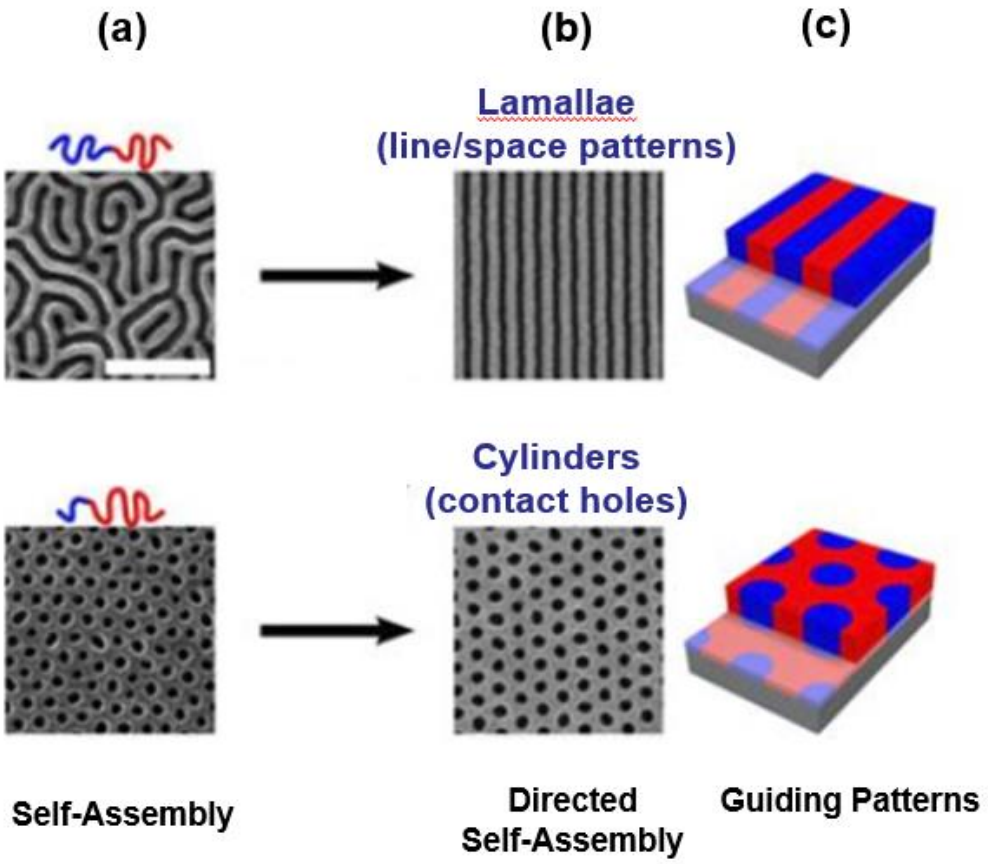

Figure 5.1 Comparison between self-assembled lamella and cylinders on (a) an un-patterned substrate and (b) a substrate patterned with (c) chemical guiding patterns. *Figure adapted from Stein, A 2016.*[7]

A notable advantage of DSA is that these guiding patterns can be printed at a relaxed pitch relative to the polymer domains allowing for pitch subdivision without the use of multiple patterning steps (Figure 5.2).

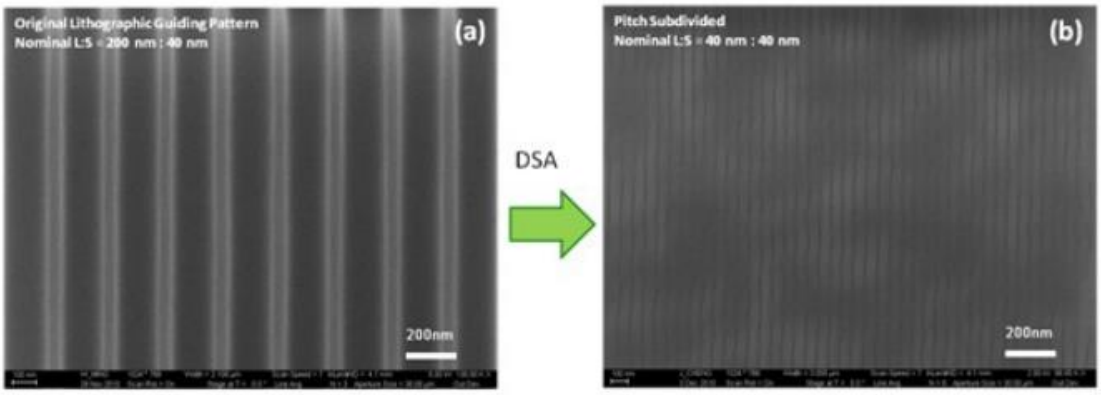

Figure 5.2 A demonstration of pitch subdivision: PS-b-PMMA (L_0 = 80 nm) assembled on a guiding layer patterned at a relaxed pitch.[8]

Forming a chemoepitaxial guiding underlayer typically requires a complex multistep process involving multiple patterning, developing, etching, and backfilling steps to form chemical guiding patterns (also referred to as pinning stripes) that preferentially wet one of the BCP blocks (Figure 5.3 (1)). It would be far preferable to instead have a single photo-definable underlayer which can have arbitrary guiding patterns directly written onto it using a light source (Figure 5.3 (2)).

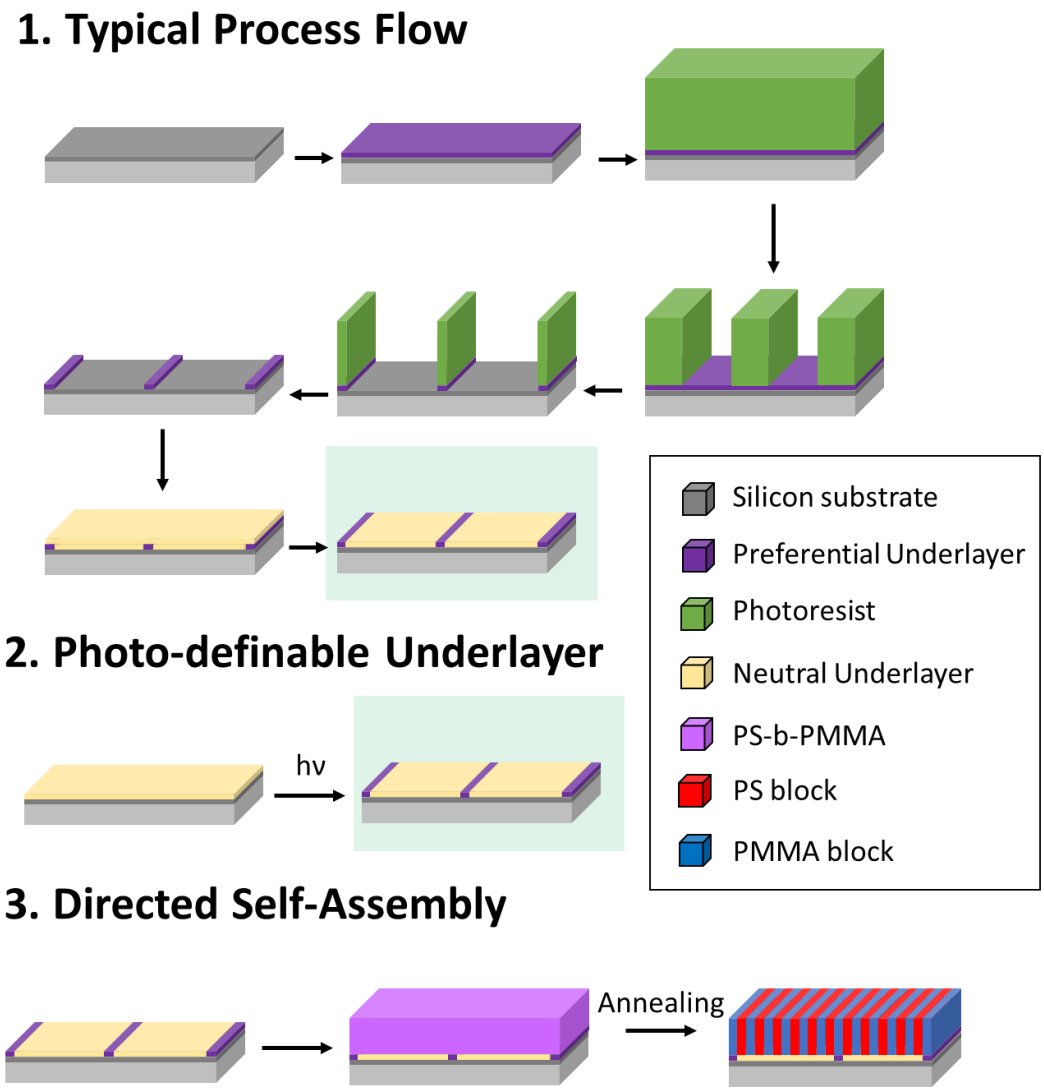

Figure 5.3 Methods for generating a chemoepitaxial guiding underlayer (highlighted in green) using 1) a typical process flow or 2) a directly photo-definable underlayer which is then used for 3) the directed self-assembly of a block copolymer.

The requirements for such an underlayer are that 1) it be capable of producing a sufficient change in contact angle to preferentially wet one of the blocks and guide DSA, 2) the method of producing this change be simple and fast, 3) it is thermally and chemically stable during the annealing of the BCP film, and 4) does not swell or distort during the spin casting of a BCP film onto it out of organic solvent. We have previously investigated a

number of chemically-amplified underlayers of this type, all of which were polymers containing a thermally cross-linkable group and phenols protected with a group that could be removed via acid-catalyzed deprotection chemistry and were blended with a small molecule photoacid generator (PAG).[8, 9] These underlayers have shown promising results (one of which was demonstrated to successfully guide the self-assembly of PS-b-PMMA[8]) however it would be beneficial to design an underlayer that does not require photoacid to cause a change in wettability and instead is protected with directly photo-cleavable protecting groups. This would eliminate the need for a PAG additive, reducing concerns of PAG aggregation and the diffusion of photoacid outside of exposed regions, as well as eliminating the need for a PEB processing step.

An initial underlayer designed and studied in this chapter uses 2-nitrobenzyl as a photolabile protecting group on a polyhydroxystyrene (PHOST) backbone using 4-vinylbenzocyclobutene (BCB) as a thermally cross-linkable group. 2-nitrobenzyl is an extensively known and studied photosensitive protecting group that has demonstrated sensitivity using both 248 nm and 198 nm lithography.[10-14] Upon exposure to light the nitrobenzyl group undergoes a rearrangement to form nitrosobenzaldehyde and releases the phenol, which increases the polarity of the surface and can be used to preferentially wet the more hydrophilic block of the BCP.

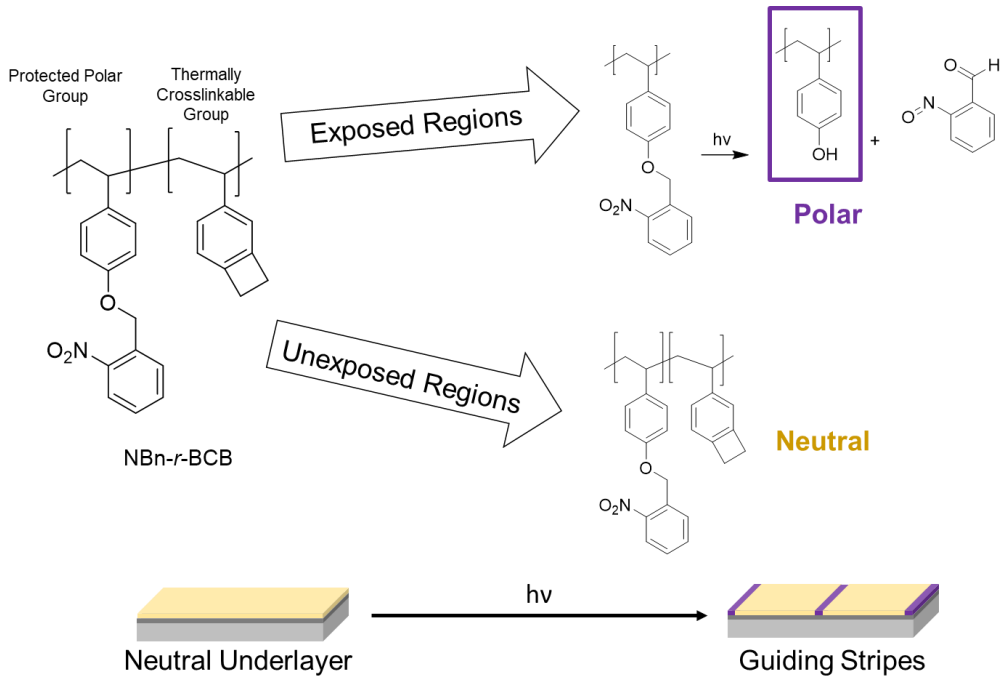

Figure 5.4 Design and structure of the non-chemically amplified photo-definable underlayer studied (NBn-*r*-BCB).

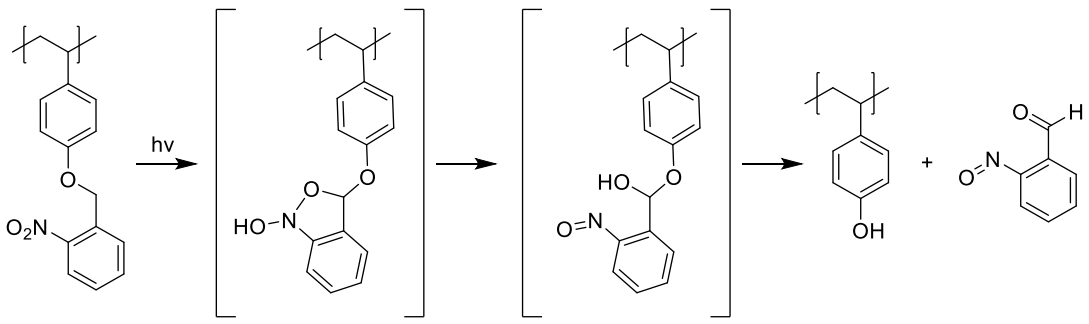

Figure 5.5 Mechanism of the photo-deprotection of PHOST using 2-nitrobenzyl as a protecting group.

5.2 Experimental

5.2.1 Materials and Methods

All reagents unless otherwise noted were purchased from TCI America, Alfa-Aesar, or Sigma-Aldrich and used without further purification. Polystyrene-b-

polymethacrylate (PS_{80}-b-$PMMA_{80}$, 80 kg/mol for PS and 80 kg/mol for PMMA, PDI = 1.09, L_0 = 80 nm) diblock copolymer was purchased from Polymer Source, Inc. and used without further purification. Solutions for spin-casting were prepared using 1 or 2 wt. % solids in propylene glycol methyl ether acetate (PGMEA). Formulations used in exposures were prepared by blending together solutions of 4-Ep with the appropriate amounts of PAG and/or PDN solution. Silicon wafers were obtained from University Wafer, cut into pieces using a diamond scribe, and cleaned with O_2 plasma for 5 min immediately prior to use. Underlayers were thermally cross-linked using a 10 min. PAB at 210 °C and developed in PGMEA for 30 sec followed by drying for 20 seconds using a nitrogen gun.

^{1}H NMR spectra were collected with a Varian Mercury Vx 300 spectrometer. Film thicknesses were measured using a M-2000 Woolam Ellipsometer. Contact angle measurements were taken with an AST VCA-2500XE contact angle system. Thermogravimetric analysis (TGA) was performed using a Perkin Elmer Pyris TGA with a 10 °C/min heating rate. Fourier transform infrared (FTIR) spectroscopy was performed using a Thermo Scientific iS50 FT-IR Spectrometer. Molecular weights and PDIs of polymers were estimated via gel permeation chromatography (GPC) using a Water 1515 isocratic pump coupled to a Waters 2489 UV detector with THF as the elution solvent and a flow rate of 0.3 mL/min at 40 °C. Etch studies were performed using a Harrick Plasma cleaner. Samples were coated onto silicon wafer pieces and placed into the chamber of the cleaner, and O_2 plasma was generated from the air using a radio frequency power setting of 10.5 W. E-beam exposures and patterning were performed with a JEOL JBX-9300FS electron beam lithography system, using a 100 keV acceleration voltage, a 1 nA current, and a 5 nm shot pitch. Film thicknesses for e-beam dose-response curves were measured

using a Tencor KLA P15 Profilometer. Patterns were imaged using a Carl Zeiss Ultra 60 scanning electron microscope (SEM) with a 2 keV acceleration voltage.

5.2.2 Synthesis and Attempted Polymerization of o-Nitrobenzyl Protected 4-Hydroxystyrene

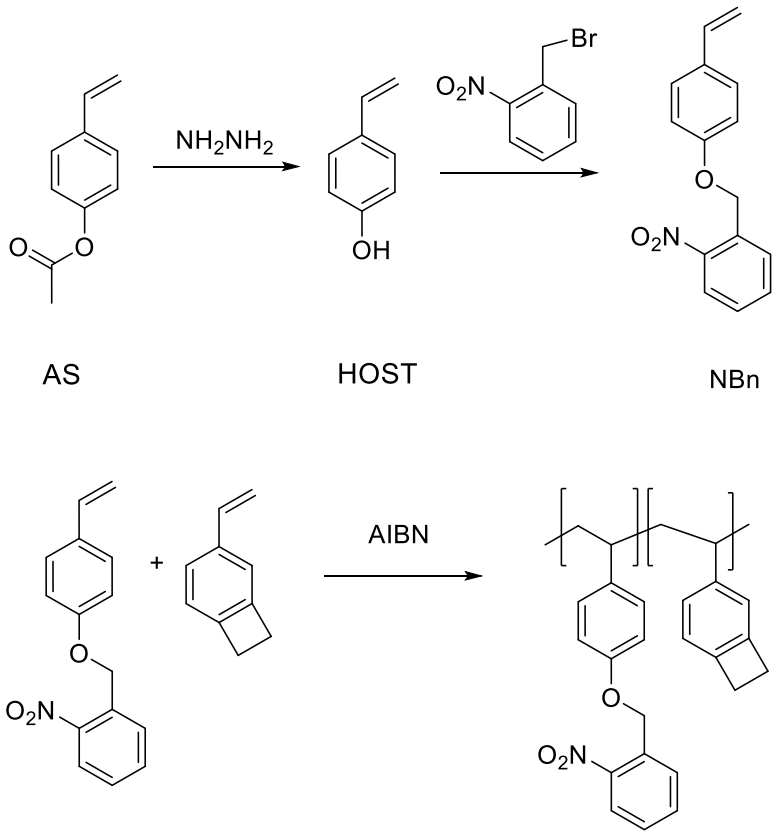

Figure 5.6 Initial (failed) synthetic scheme for NBn-*r*-BCB.

The initial experimental plan was to synthesize 2-nitrobenzyl protected 4-hydroxystyrene monomer (NBn) via the deprotection and reprotection of 4-acetoxystyrene, and radically copolymerize it with vinyl-benzocyclobutene using azobisisobutyronitrile (AIBN) as an initiator. These attempts failed however, as no polymer was synthesized and nearly all of the unreacted NBn monomer was recovered (Figure 5.7). The proposed

explanation for this is that the 2-nitrobenzyl group is acting as an inhibitor/retarder to free radical polymerization, behaviour which has been previously reported in attempts to polymerize *o*-nitrobenzyl methacrylate and acrylate.[15] This behaviour was particularly surprising however, as the successful free radical polymerization of o-nitrobenzyl protected methacrylate and styrene has been reported elsewhere in the literature.[16] Regardless, an alternative synthetic approach was taken where 4-acetoxystyrene was polymerized and subsequently deprotected and re-protected with 2-nitrobenzyl bromide.

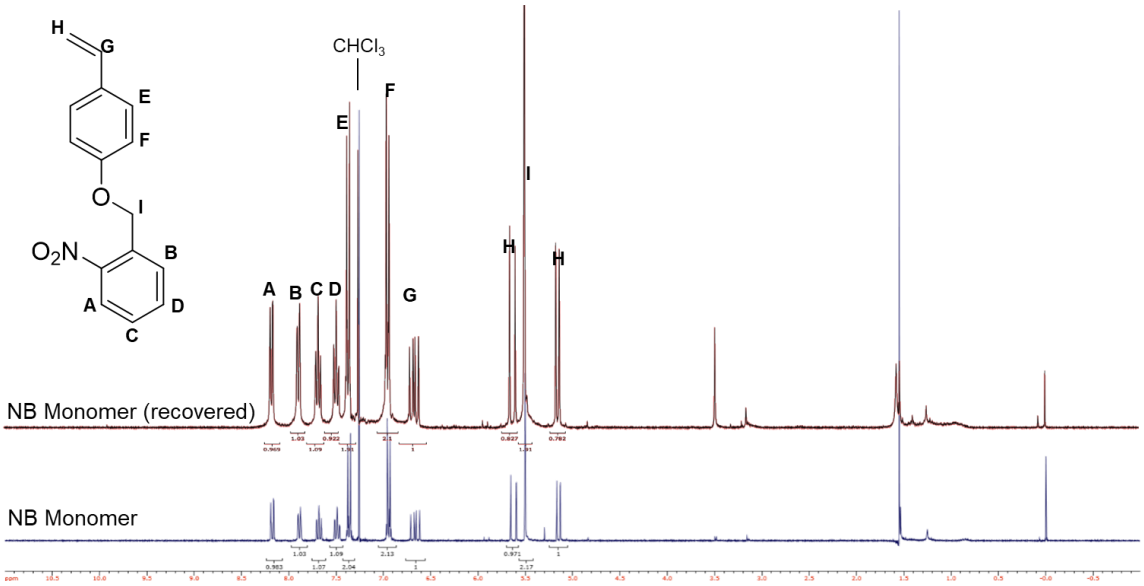

Figure 5.7 ^{1}H NMR (300 MHz) spectrum of NB monomer and unreacted NB monomer recovered after attempted polymerization (in $CDCl_3$).

5.2.3 Synthesis of AS-r-BCB

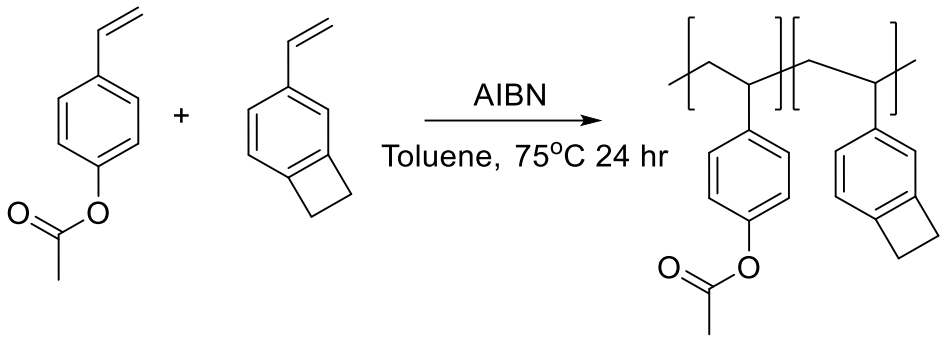

Figure 5.8 Synthetic scheme for AS-*r*-BCB.

Inhibitor was removed from 4-acetoxystyrene (AS) and 4-vinylbenzocyclobutene (BCB) by passing them through a neutral alumina column. AS (1.00 g, 6.16 mmol) and BCB (0.16 g, 1.22 mmol) were then added to a 10 mL Schlenk flask containing 2 mL of dry toluene. AIBN (0.02 g, 0.12 mmol) was added and three freeze-pump-thaw cycles were performed followed by a dry nitrogen backfill. The flask was placed in an oil bath at 75°C and stirred for 24 hours. The polymerization was quenched by opening the flask to air and placing it in an ice bath. A small amount of dichloromethane (DCM) was added to dilute the solution which was then precipitated into methanol, forming a white powder. The solution was filtered, and the polymer was dried under vacuum overnight. The ^{1}H NMR of the collected polymer can be seen in Figure 5.9. Yield: 83 %. M_w = 40,900 g/mol, PDI = 1.6.

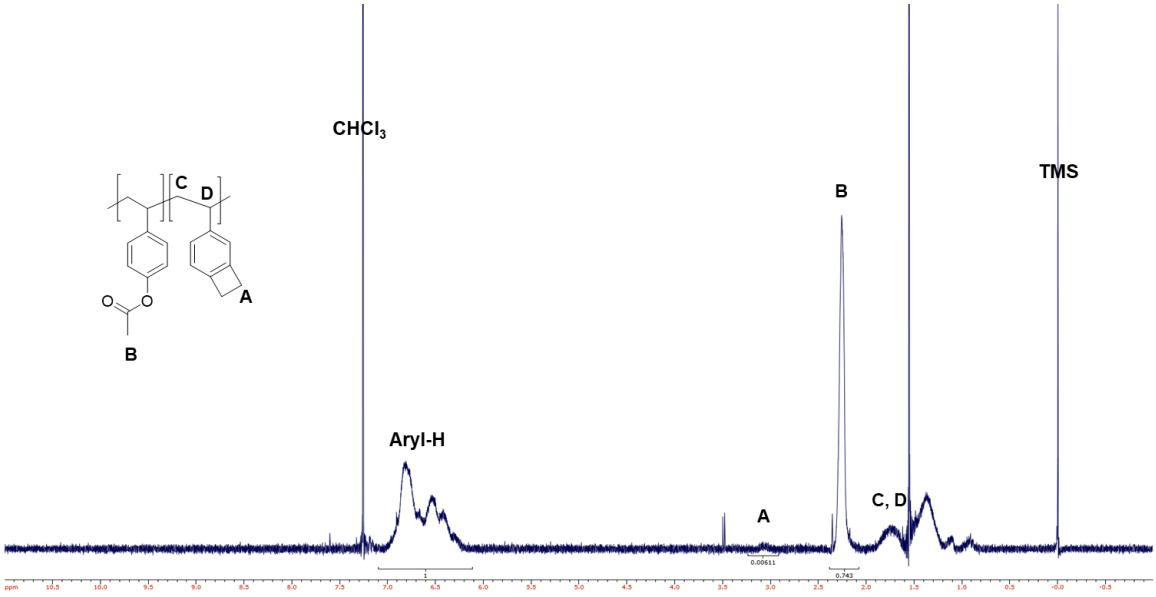

Figure 5.9 ^{1}H NMR (300 MHz) spectrum of AS-*r*-BCB (in $CDCl_3$).

5.2.4 Synthesis of PHOST-r-BCB

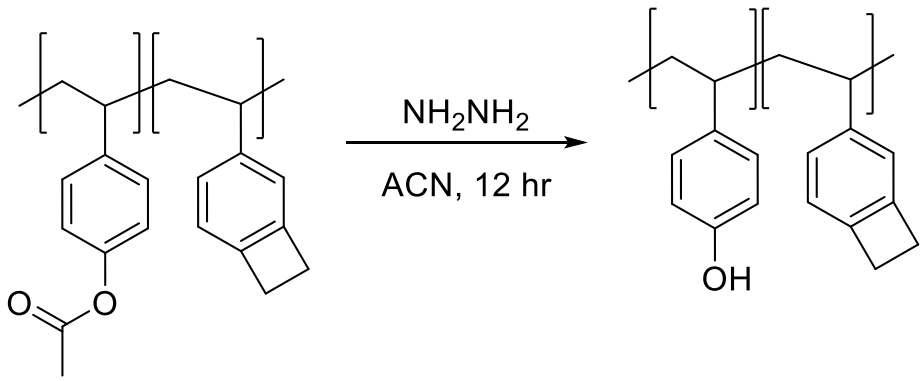

Figure 5.10 Synthetic scheme for PHOST-*r*-BCB.

AS-*r*-BCB (1.0 g) was dissolved in 1.5 mL acetonitrile (ACN) in a 22 mL glass vial. Hydrazine hydrate ($NH_2NH_2 \cdot H_2O$, 1.25 g) was added dropwise to the solution which was then capped and stirred at room temperature for 12 hours. The reaction was quenched via the addition of 3 % HCl solution, and the polymer was extracted with ethyl acetate, concentrated using rotary vacuum evaporation, and precipitated into deionized (DI) water

forming a white powder. The solution was filtered, and the polymer was dried under vacuum overnight. The disappearance of the acetoxy group in the ^{1}H NMR spectra (Figure 5.11) and the appearance of a broad -OH peak indicate the complete deprotection of AS-*r*-BCB. FTIR analysis (Figure 5.12) provides further evidence of this with the disappearance of the C=O carbonyl stretching peak at 1755 cm^{-1} and the appearance of a broad phenol O-H stretching peak from 3550 – 3050 cm^{-1}. Yield: 80 %.

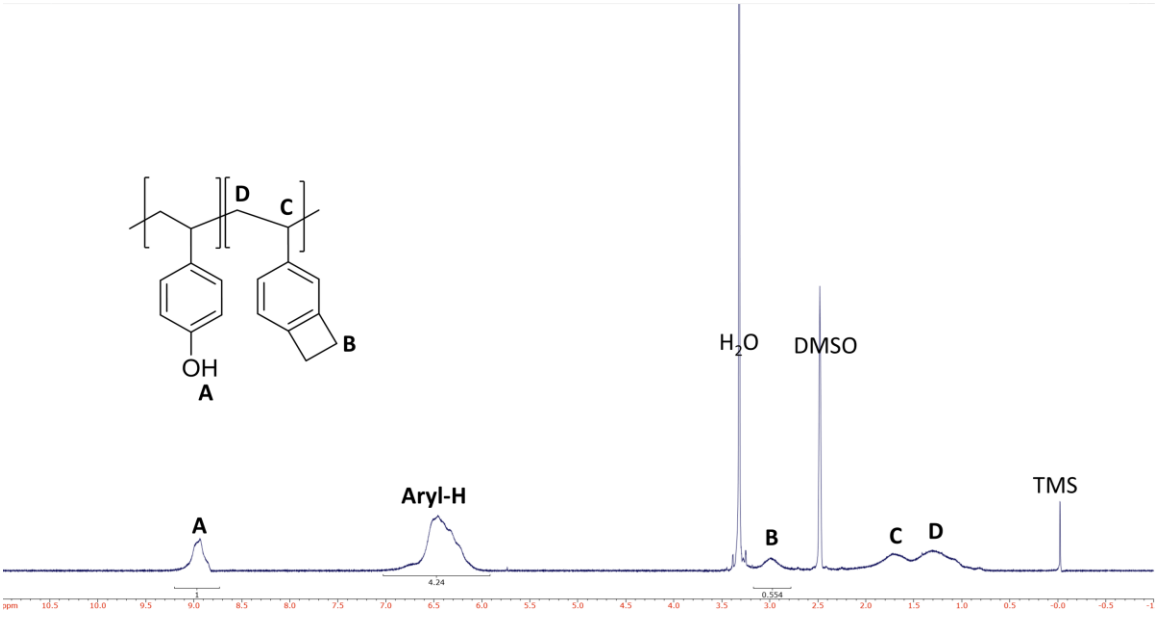

Figure 5.11 ^{1}H NMR (300 MHz) spectrum of PHOST-*r*-BCB (in DMSO-d_6).

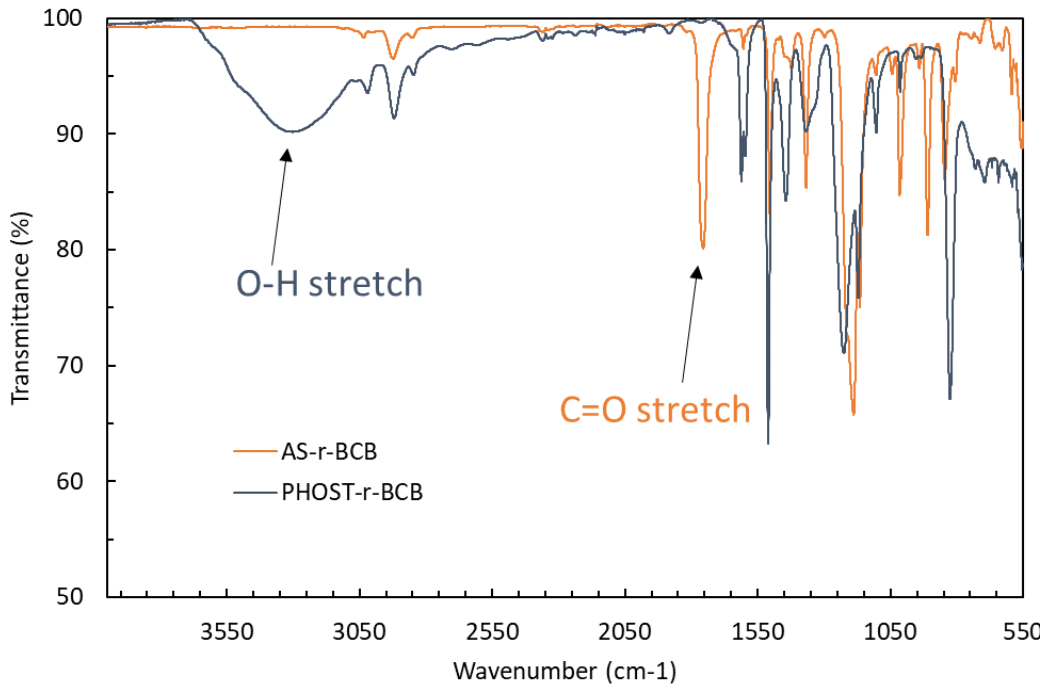

Figure 5.12 FTIR spectra of the deprotection of AS-*r*-BCB to give PHOST-*r*-BCB.

5.2.5 Synthesis of NBn-r-BCB

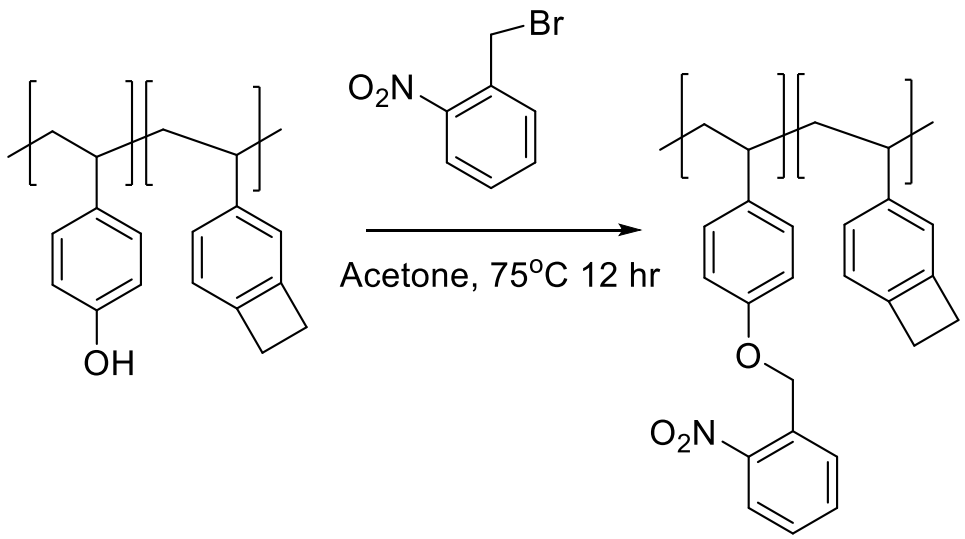

Figure 5.13 Synthetic scheme for NBn-*r*-BCB.

PHOST-*r*-BCB (0.1 g) was dissolved in 3.5 mL acetone in a 22 mL glass vial. Potassium carbonate (K_2CO_3, 0.1 g) was added along with a catalytic amount of 18-crown-6 as a phase transfer catalyst. 2-Nitrobenzyl bromide (0.2 g) was added to the solution which was then capped and placed in a 75 °C oil bath where it was stirred for 12 hours. Once the solution had cooled to room temperature it was extracted with DCM and washed 3 times with DI water. The combined organic layers were concentrated using a rotary evaporator and precipitated in cold methanol to give a light white-yellow powder, which was filtered out of solution and dried under vacuum overnight. The appearance of the aromatic/aliphatic hydrogen peaks from the NBn protecting group in the ^{1}H NMR spectra (Figure 5.14) and the disappearance of the broad -OH peak suggests the complete protection of PHOST-*r*-BCB. FTIR analysis (Figure 5.15) provides further evidence of this with the disappearance of the broad phenol O-H stretching peak from 3550 – 3050 cm^{-1} and the appearance of symmetric aromatic N-O stretching peaks at 1521 cm^{-1} and 1336 cm^{-1}. The molar composition of NBn-*r*-BCB was determined to be 83 % and 17 % respectively via ^{1}H NMR analysis. ^{1}H NMR spectra (Figure 5.14). Yield: 98 %. M_w = 43,500 g/mol, PDI = 1.5.

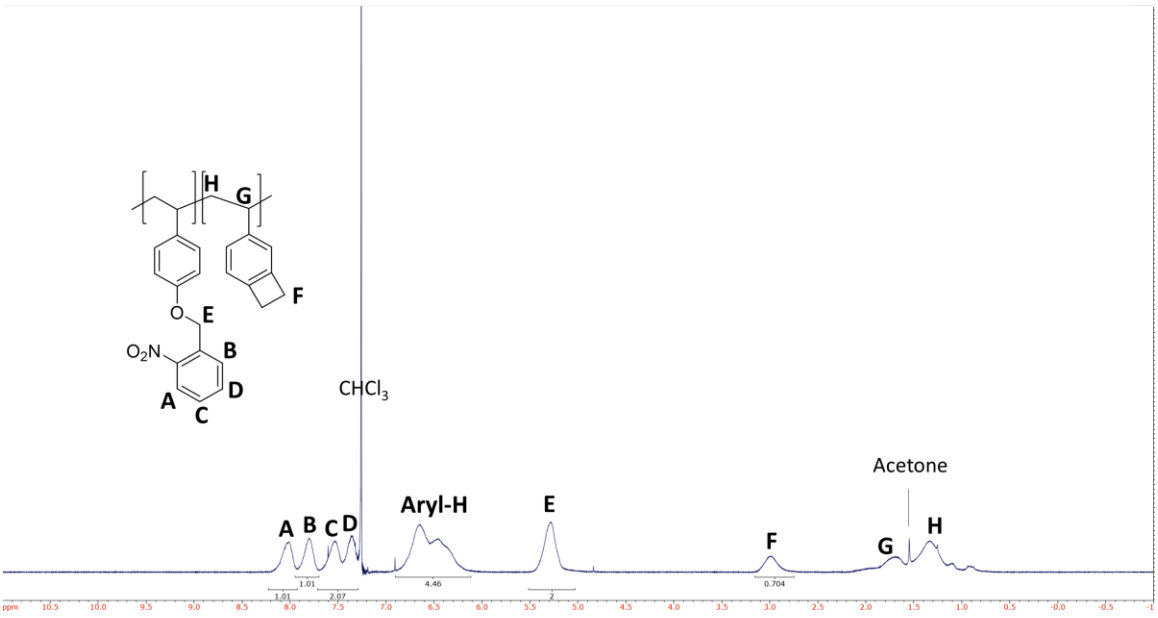

Figure 5.14 ^{1}H NMR (300 MHz) spectrum of NBn-*r*-BCB (in $CDCl_3$).

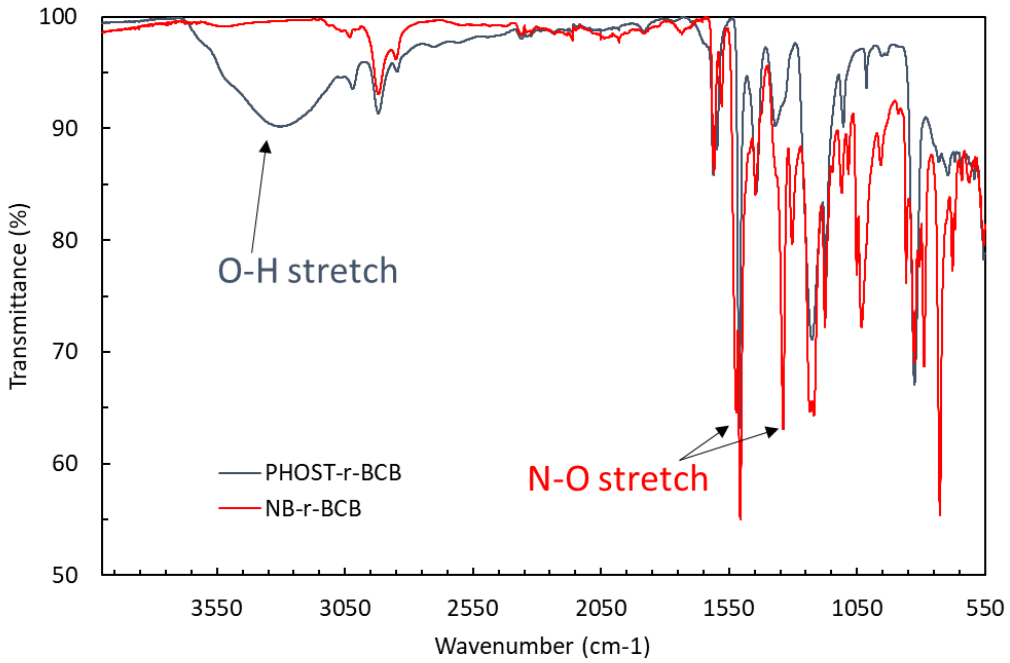

Figure 5.15 FTIR spectra of the protection of PHOST-*r*-BCB to give NBn-*r*-BCB.

5.3 Results and Discussion

5.3.1 Thermal Stability of 2-Nitrobenzyl Protecting Group

If NBn-*r*-BCB or any 2-nitrobenzyl deprotection chemistry is to be used as a guiding layer for BCP DSA, then the 2-nitrobenzyl protecting groups must be thermally stable under the annealing conditions (typically in the range of 250-280 °C[17]) required during the thermal annealing of BCPs as well as stable under the conditions required to thermally cross-link the underlayer (210 °C for 10 minutes). Thermogravimetric analysis (TGA) was used to test the thermal stability of the underlayer (Figure 5.16), showing that it had sufficient thermal stability at all of these temperatures (210-280 °C) with the onset of decomposition or possibly thermally-induced deprotection occurring at approximately 380 °C.

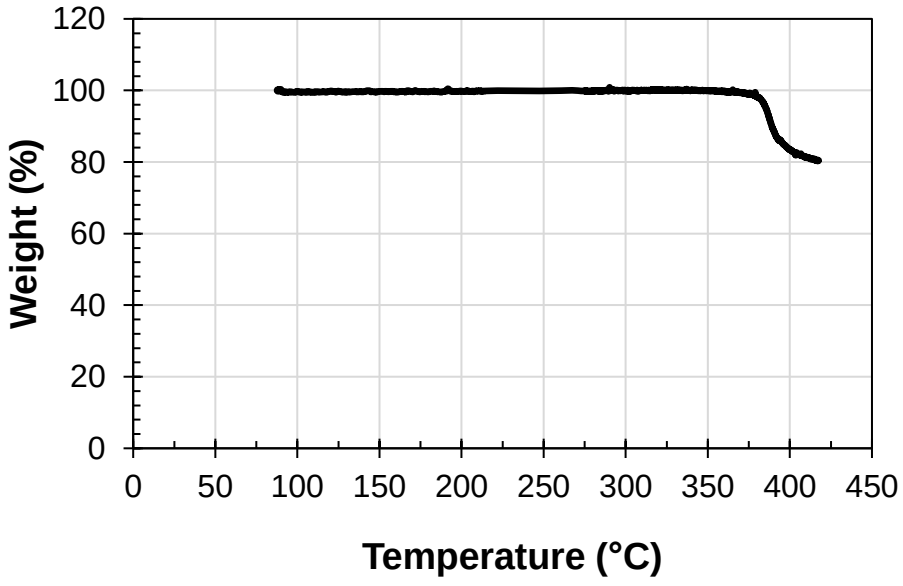

Figure 5.16 TGA (10 °C/min.) of NBn-*r*-BCB.

Measurements of the film thickness and water contact angle of a 30 nm thermally crosslinked NBn-*r*-BCB film at 225 °C and 250 °C were also taken in order to probe other possible effects of baking the underlayer at elevated temperatures. At 250 °C, after 30 minutes (the conditions typically required for the self-assembly of perpendicular PS-b-PMMA lamellae) a drop in NRT of 23 % was observed, but with no change in water contact angle (Table 3). After 60 minutes at 250 °C the NRT dropped even further for a total loss in film thickness of 40 % and the water contact angle dropped 10 °. A drop in contact angle is commonly caused by a change in surface energy, which might seem to suggest that some of the protecting groups are thermally deprotecting at a slow enough rate that it was not detected in the 10 °C/min. ramp rate used when collecting the TGA of NBn-*r*-BCB. An isothermal TGA (Figure 5.17) and ^{1}H NMR spectra of NBn-*r*-BCB before and after a 60 min. bake at 250 °C show that this is not the case however, with no mass change and no changes in peaks or peaks from PHOST-*r*-BCB observed (Figure 5.18 and Figure 5.19). Since PHOST-*r*-BCB is insoluble in $CDCl_3$ and NBn-*r*-BCB is only moderately soluble in DMSO, NMR spectra of the sample was collected using both deuterated solvents. The change in contact angle was therefore attributed to increased surface roughness[18] caused by curing shrinkage in the film as indicated by the loss of film thickness.

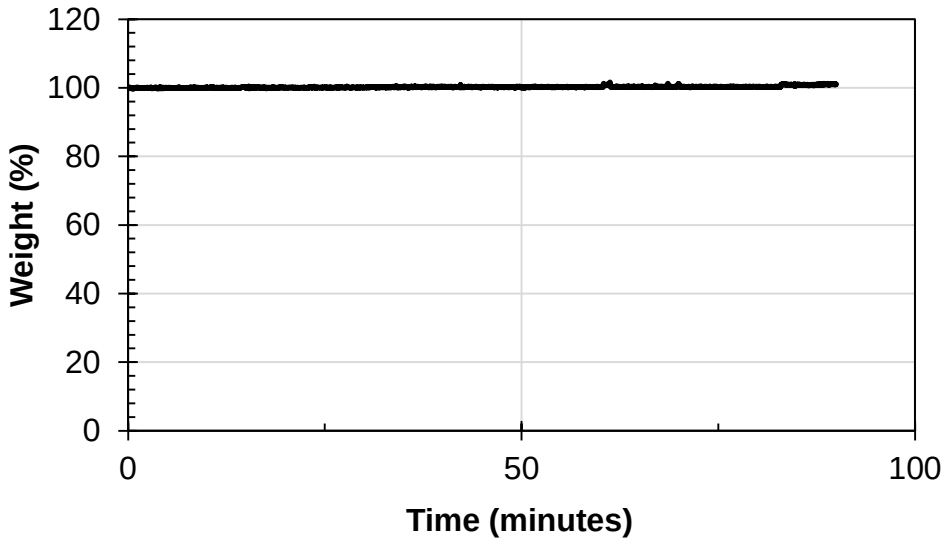

Figure 5.17 Isothermal TGA of NBn-*r*-BCB at 295 °C. No change in mass was observed.

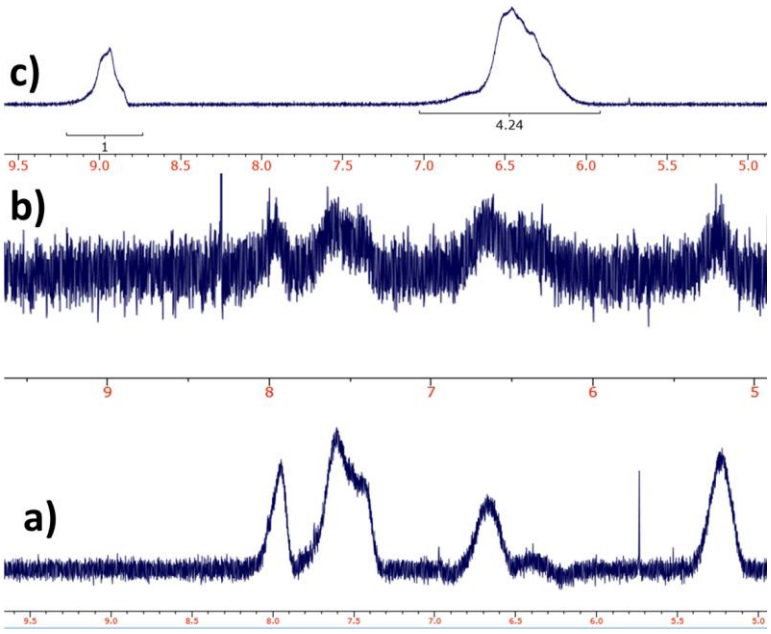

Figure 5.18 ^{1}H NMR (300 MHz) spectra in DMSO-d6 of a) NBn-*r*-BCB b) NBn-*r*-BCB after 60 min. at 250 °C and c) PHOST-*r*-BCB representing unprotected NBn-*r*-BCB as a reference.

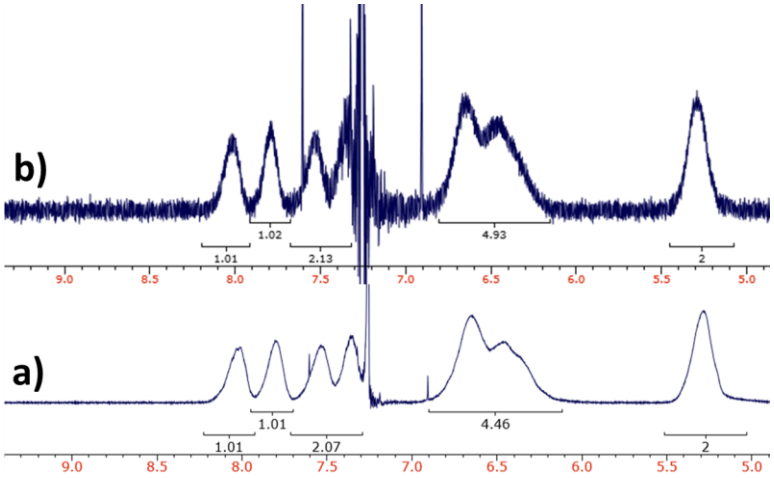

Figure 5.19 ^{1}H NMR (300 MHz) spectra in $CDCl_3$ of a) NBn-*r*-BCB and b) NBn-*r*-BCB after 60 min. at 250 °C

.

Table 3 Normalized Remaining Thicknesses (NRT) and contact angles of a 30 nm film of NBn-*r*-BCB baked at 250 °C.

Bake Time (min.)	NRT	Water Contact Angle (°)
0	1.00	80
30	0.77	80
60	0.60	70

Table 4 Normalized Remaining Thicknesses (NRT) and contact angles of a 30 nm film of NBn-*r*-BCB baked at 225 °C.

Bake Time (min.)	NRT	Water Contact Angle (°)
0	1.00	80
30	0.93	80
60	0.86	78

When baking at 225 °C, a small decrease in the film thickness was observed after 30 minutes but with no change in water contact angle (Table 4). After an additional 30 minutes of annealing time the film thickness dropped further and a very small change in water contact angle was observed. Based on previous results, this was also attributed to an increase in surface roughness caused by film shrinkage. While the effect of annealing temperature on the DSA process can be complicated, generally speaking high annealing temperatures (≥ 250 °C) are desired to allow for faster assembly and defect annihilation.[19] PS-b-PMMA and other BCPs can be self-assembled at lower temperatures such as 225 °C (so long as it is above the T_g of both blocks) albeit at a reduced rate.

5.3.2 Relative Etch Rates

An etch study was done on the unprotected PHOST-*r*-BCB as well as NBn-*r*-BCB to get a general sense of how the etch rate compared to PS and PMMA (PMMA being the block which is preferentially etched due to its higher etch rate). Typically, it is desirable for the underlayer to have a rapid etch rate, as this ensures that the maximum amount of the relief material is left as an etch mask for the substrate and reduces the possibility of undesired removal of the etch mask. When etched using the same conditions (O_2 plasma) NBn-*r*-BCB was found to etch slower than both PS and PMMA. While this does not disqualify its use as an underlayer, as it can either be coated extremely thin and/or a temporary etch-resistant coating can be applied to one of the polymer domains[20, 21] or one of the domains can be infiltrated with an etch-resistant material,[22-26] such techniques are less than ideal. PHOST-*r*-BCB (the deprotected pinning stripe) etched 1.2-1.4x faster than PS and NBn-*r*-BCB under these conditions which is preferable behaviour especially as it is the pinning stripe for the removed PMMA block and would be exposed. However, as

these guiding patterns are generated at a relaxed pitch relative to the assembled PS-b-PMMA domains there would still remain a significant amount of NBn-*r*-BCB that would then need to be removed. It is worth noting that these are unlikely to be the same etch conditions used in manufacturing and that these etch rates are not meant to be accurate measurements, but simply a way to examine their etch rates relative to PS and PMMA under the same conditions.

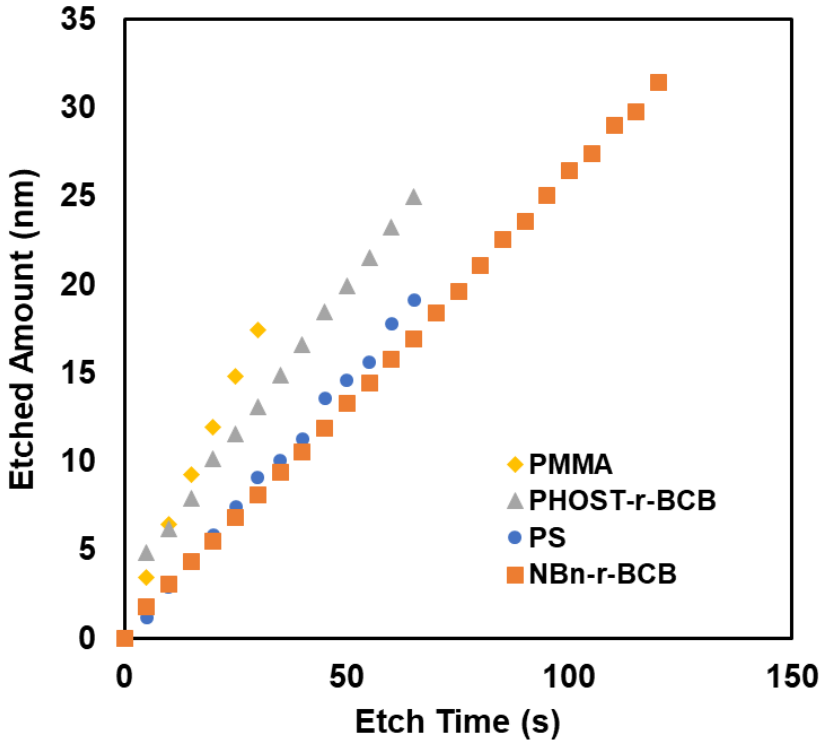

Figure 5.20 O_2 plasma etch study comparing the relative etch rates of PS, PMMA, PHOST-*r*-BCB and NBn-*r*-BCB.

5.3.3 Underlayer Neutrality and Undirected Self-Assembly of PS-b-PMMA

One of the requirements of an underlayer is that it provide perpendicular orientation to ordered domains by not having a strong wetting preference for either block of the BCP during its self-assembly. If the underlayer does preferentially wet either block, this will

result in horizontally aligned lamellae which are not useful when transferring patterns into the substrate for the purposes of lithography (Figure 5.21).

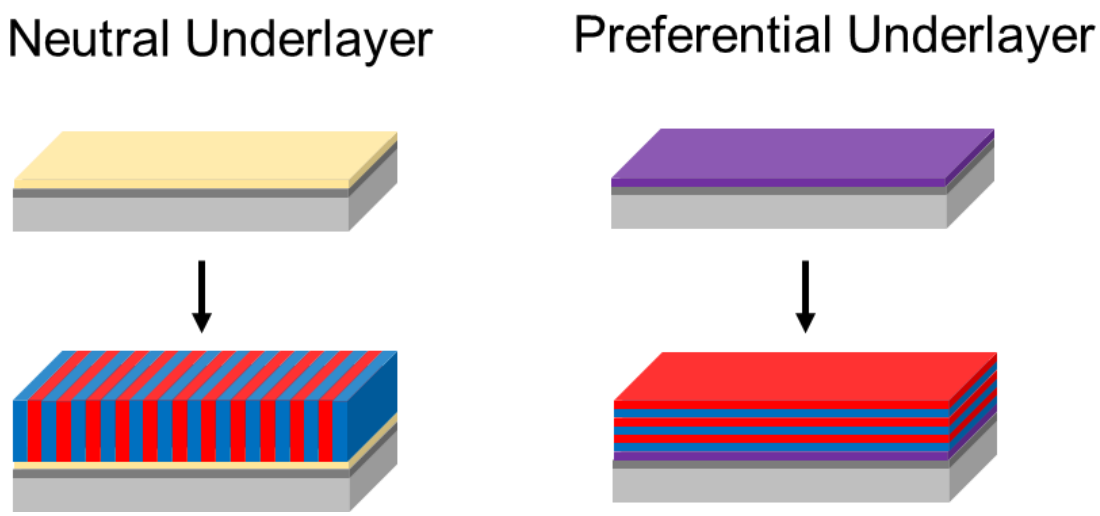

Figure 5.21 Examples of lamellae orientations of a block copolymyer self-assembled on a neutral versus a preferential underlayer.

An underlayer with no preference to either domain is referred to as “neutral”, a property that can be loosely measured by comparing the water contact angle of the underlayer to the water contact angles of either of the blocks of the BCP (here PS-b-PMMA). It is even considered preferable that the “neutral” un-patterned underlayer have a slight preference to the non-polar block as this has been shown to improve the formation of defect free perpendicular lamellae.[27 28]

The water contact angle of the NBn-*r*-BCB polymer was found to be 80 °, which was serendipitously close to the average (77 °) of PS (90 °) and PMMA (65 °) suggesting that it should not have a strong preference towards either block and should allow for the self-assembly of perpendicularly aligned lamellae. Adjusting the contact angle of the unexposed underlayer to extend its use for other BCPs or to minimize defectivity can be

achieved either through the incorporation of a third monomer, through incomplete protection of the PHOST-*r*-BCB ensuring that some of the polar phenol groups remain, or through the blanket exposure of the NBn-BCB underlayer with a dose of light sufficient enough to partially deprotect it.

While contact angles can be informative, the ultimate test of the neutrality of an underlayer is to see if continuous perpendicular lamellae could be successfully assembled on top of an unguided/unpatterned underlayer. A 39 nm film of underlayer was coated onto a silicon wafer piece, thermally cross-linked and developed, and a 72 nm film of PS_{80}-b-$PMMA_{80}$ was spun-coat on top. The wafer was then thermally annealed at 225 °C (chosen for reasons discussed previously) under a continuous flow of dry N_2 gas for 30 minutes and imaged using a SEM. After 30 minutes perpendicular lamellae had started to form but mixed or possibly parallel regions were still observed (Figure 5.22 a). The wafer was cleaved in two and one half was thermally annealed using the same condition for an additional 30 minutes, after which fully formed perpendicular self-assembled lamellae were observed (Figure 5.22 b).

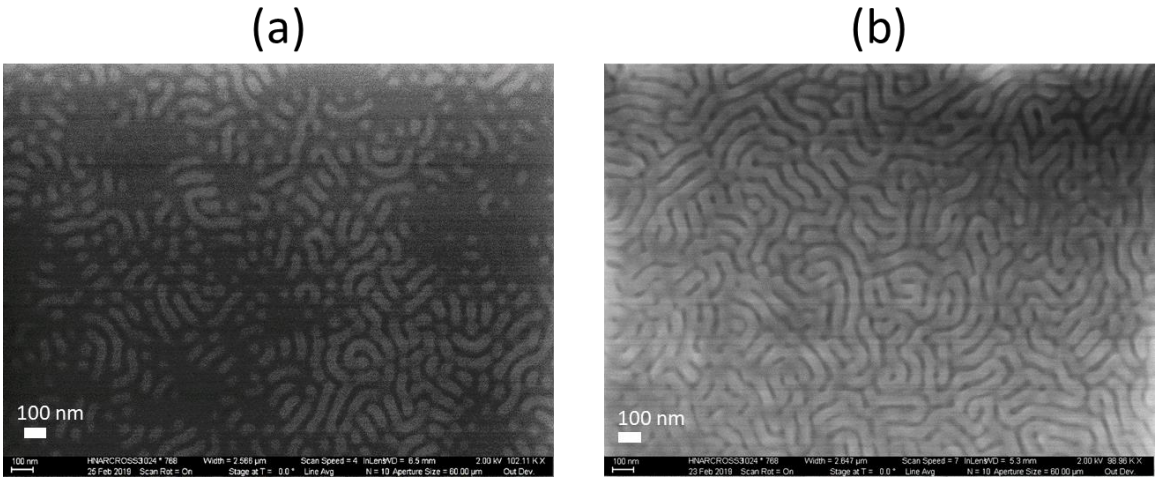

Figure 5.22 SEM of PS_{80}-b-$PMMA_0$ (L_0 ~ 80 nm) lamellae thermally annealed at 225 °C after (a) 30 min. and (b) 60 min.

5.3.4 DUV Dose Response

In order to be used as a photo-writable underlayer it must be demonstrated that the polarity of the surface is tuneable as a function of dose. The water contact angle of the NBn-*r*-BCB precursor PHOST-*r*-BCB, which can be used to represent the fully photo-deprotected NBn-*r*-BCB was measured and found to be 60 °. This provides a theoretical contact angle modulation of 20 ° from the fully protected water contact angle of 80 °, which is close to the modulation and contact angles of a previous underlayer design which was demonstrated to successfully guide the self-assembly of PS-b-PMMA.[8] The film thickness and contact angle change as a function of dose of DUV (298 nm) light of a 39 nm film of NBn-r-BCB were measured and can be seen in Figure 5.23.

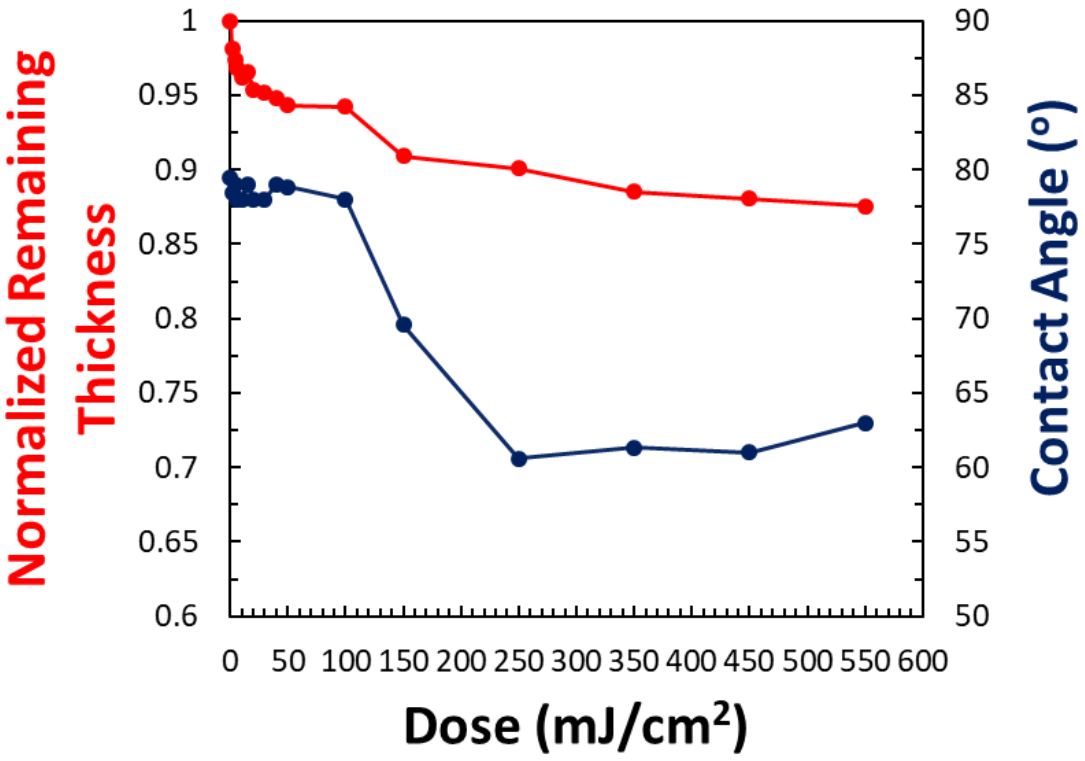

Figure 5.23 DUV dose response curve for NBn-*r*-BCB.

A decrease in film thickness was observed, which occurs due to the loss of the protecting groups as 2-nitrosobenzaldehyde. Interestingly there appeared to be a shift between the onset of deprotection as indicated by the change in film thickness (which starts at low doses) and deprotection as indicated by the change in water contact angle (which does not change significantly until approximately 150 mJ/cm^2. Changes in surface roughness due to deprotection might be affecting contact angle measurements, but previous results suggest that higher roughness should decrease the contact angle meaning that one would expect the dose-response curve to be shifted to lower, not higher doses. One mechanism that could account for this behaviour is surface rearrangement where the polar OH groups bury themselves in the film to reduce its surface energy.[29] This is further

supported by a water contact angle measurement taken of the NBn-*r*-BCB film after 24 hours of storage under ambient conditions after which it had almost completely reverted to the contact angle of the completely unexposed film (from 60 ° to 76 ° after 24 hours compared to the unexposed water contact angle of 80 °). It is important to note that the interface interactions between the underlayer and polymer differ from those between the underlayer and water, thus these contact angle measurements should not be taken as quantitative measurements of a desired dose but instead as qualitative indications of a change in surface chemistry.

5.3.5 E-Beam Patterning and Guided Assembly of PS-b-PMMA

Guiding patterns of 40 nm lines with a 320 nm pitch were imaged using e-beam lithography, and a 72 nm film of PS_{80}-b-$PMMA_{80}$ (L_0 ~ 80 nm) was spun-coat and thermally annealed on top at 250 °C for 30 minutes or at 225 °C for 60 minutes. When thermally annealed at 250 °C, no perpendicular lamellae were observed and instead the BCP formed an island/hole topography throughout the film (Figure 5.24 a). The influence of the guiding patterns can be seen through the presence of periodic stripes pinning the darker PMMA block (Figure 5.24 b) although the apparent width and pitch of these stripes is far different from the original pattern.

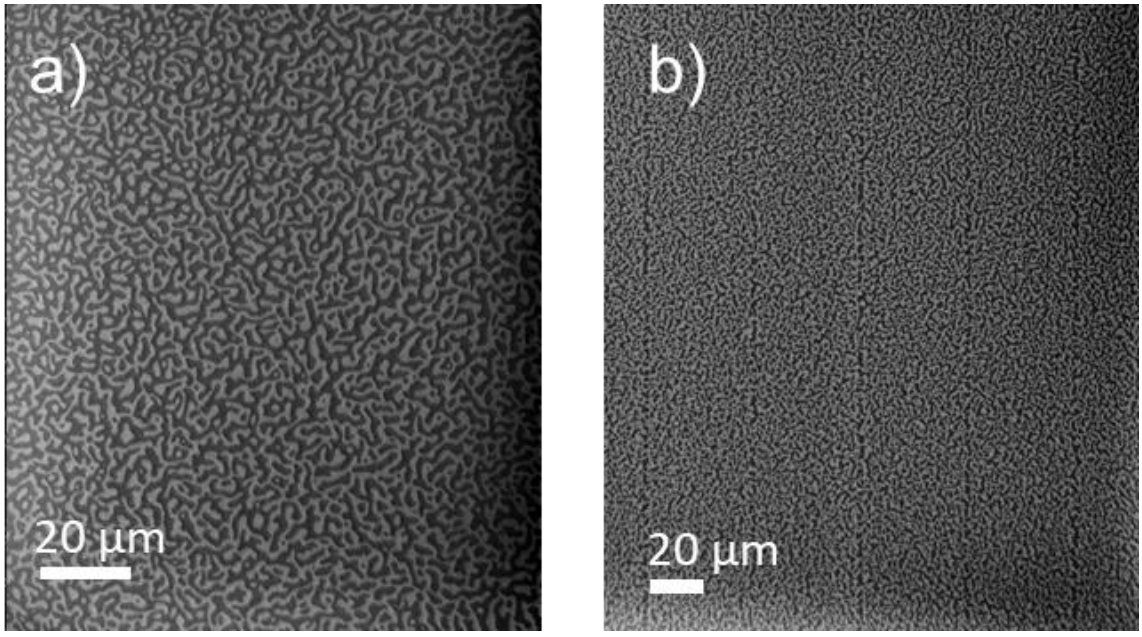

Figure 5.24 SEM of PS_{80}-b-$PMMA_{80}$ (L_0 ~ 80 nm) annealed at 250 °C on NBn-*r*-BCB underlayer in a) an un-patterned region and b) a region patterned with guiding stripes on the same sample.

One explanation is that the high surface roughness of the underlayer is causing the nucleation of holes or islands at the surface. Islands and holes can also form when the underlayer is preferential to one domain, but the film thickness is incommensurate with the polymer domain spacing (not an integer multiple of L_0) meaning it cannot form parallel lamellae (which should apply here since the film thickness was ~70 nm and L_0 of PS-b-PMMA used was 80 nm).[30]

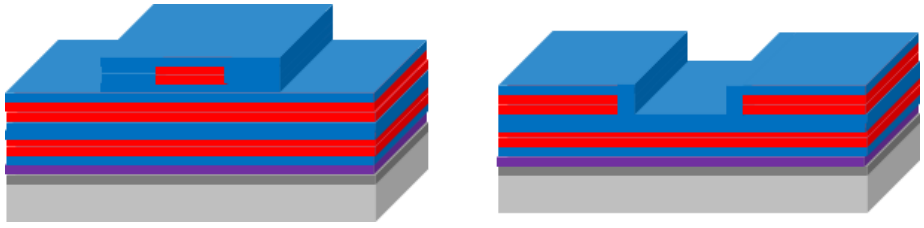

Figure 5.25 Illustrations of island and hole formations which occurs when lamellar films whose thickness is not commensurate with their pitch are assembled on a preferential underlayer.

While the underlayer was previously demonstrated to be sufficiently neutral to assemble perpendicular lamellae when annealed at 225 °C and should not be preferential in un-patterned regions, it is possible that at elevated temperatures surface rearrangement and/or interpenetration of the block copolymer and the underlayer changes the interactions between the two, causing the underlayer to become preferential towards one of the domains.[17] The relatively large thickness of the underlayer and high surface roughness might also contribute towards interpenetration.[31, 32]

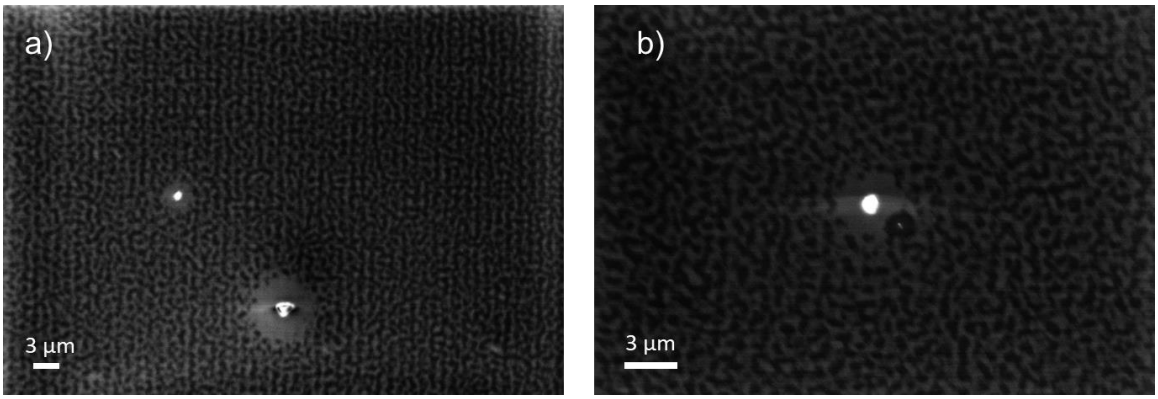

Figure 5.26 SEM of PS_{80}-b-$PMMA_{80}$ (L_0 ~ 80 nm) annealed at 220 °C on NBn-*r*-BCB underlayer in a) a region patterned with guiding stripes and b) an un-patterned region on the same sample.

Interestingly, DSA at 225 °C on e-beam patterned underlayer also showed island/hole formation both in regions with guiding patterns (Figure 5.26 a) and regions without guiding patterns (Figure 5.26 b). SEM images taken suggest that the underlayer preferentially wets the PMMA domain (the darker regions) despite using the exact same solutions and film thicknesses of both the underlayer and PS-b-PMMA as well as the same thermal annealing conditions. The influence of the guiding patterns however can clearly be seen in the straight, periodic stripes of PMMA in guided regions. The size of the island/hole

regions are smaller than those observed after annealing at 250 °C and the pinned stripes have a denser pitch, although these sizes and pitches are still larger than the original guiding patterns (40 nm stripes with a 320 nm pitch). It is unclear what is causing this change in underlayer preference between PS-b-PMMA assembled on un-patterned un-exposed underlayer and PS-b-PMMA assembled on un-patterned regions of exposed underlayer. One possibility is that released iso-benzaldehyde from the deprotection reaction has contaminated the surface of the sample and is affecting its surface energy, which could potentially be removed using a post processing development step. Another possibility is that surface roughness changes caused by exposure to a high vacuum in the e-beam chamber for ~3 hours (potentially from the removal of residual casting solvent) is contributing towards island/hole formation or interpenetration with PS-b-PMMA. Incorporation of a third monomer such as polystyrene or perhaps adjusting the percentage of BCB monomer in the underlayer composition might help to expand the process window and allow for the formation of lamellae. Additionally, increasing the amount of BCB might increase the crosslink density of the underlayer and reduce both cure shrinkage and interpenetration as well as allowing for thermal annealing at higher temperatures.

5.4 Summary and Conclusions

A non-chemically amplified photodefinable polymer underlayer based on the photo-deprotection of PHOST (NBn-*r*-BCB) has been synthesized. The nitrobenzyl protecting groups were found to be thermally stable at the temperatures required to thermally crosslink the underlayer and at typical temperatures used in the thermal annealing of block copolymers (stable up to 360 °C), although film loss due to curing shrinkage and an increase in contact angle attributed to a higher surface roughness was observed when the

underlayer was baked at 250 °C. The initial underlayer design was found to have a lower O_2 plasma etch rate relative to both PS and PMMA which was attributed to the large amounts of aromatic rings in the polymer and the protecting group.

The underlayer surface energy was found to be tunable as a function of dose using DUV light with a water contact angle modulation of ~20 °. The un-patterned and un-exposed underlayer was found be sufficiently non-preferential to align perpendicular lamella of PS_{80}-b-$PMMA_{80}$ (L_0 ~ 80 nm). Electron beam lithography was used to successfully de-protect NBn-*r*-BCB and write guiding patterns preferential to PMMA, however the exposure process changed the surface energy of the film to preferentially wet one of the blocks causing the formation of an island/hole topology instead of perpendicular lamella in all regions including those that were not patterned. The exact cause for this behavior is unclear, but there are multiple methods to adjusting the surface energy of the underlayer through relatively simple changes in the polymer composition which might be used to expand the process window of DSA.

5.5 References

1. Yamauchi, S., Hara, A., Oyama, K., Natori, S., Yamato, M. and Yaegashi, H., *Extendibility of self-aligned type multiple patterning for further scaling*. SPIE: 2013; Vol. 8682, p 7.

2. Chen, Y., Cheng, Q. and Kang, W., *Technological merits, process complexity, and cost analysis of self-aligned multiple patterning*. SPIE: 2012; Vol. 8326, p 14.

3. Shiu, W., Liu, H. J., Wu, J. S., Tseng, T.-L., Liao, C. T., Liao, C. M., Liu, J. and Wang, T., *Advanced self-aligned double patterning development for sub-30-nm DRAM manufacturing*. SPIE: 2009; Vol. 7274, p 7.

4. Bates, F. S. and Fredrickson, G. H., Block Copolymers—Designer Soft Materials. *Physics Today* **1999,** *52* (2), 32-38.

5. Segalman, R. A., Yokoyama, H. and Kramer, E. J., Graphoepitaxy of Spherical Domain Block Copolymer Films. *Advanced Materials* **2001,** *13* (15), 1152-1155.

6. Peters, R. D., Yang, X. M., Wang, Q., Pablo, J. J. d. and Nealey, P. F., Combining advanced lithographic techniques and self-assembly of thin films of diblock copolymers to produce templates for nanofabrication. *Journal of Vacuum Science & Technology B: Microelectronics and Nanometer Structures Processing, Measurement, and Phenomena* **2000,** *18* (6), 3530-3534.

7. Stein, A., Wright, G., Yager, K. G., Doerk, G. S. and Black, C. T., Selective directed self-assembly of coexisting morphologies using block copolymer blends. *Nature Communications* **2016,** *7*, 12366.

8. Cheng, J., Lawson, R. A., Yeh, W.-M., Tolbert, L. M. and Henderson, C. L., *Developing directly photodefinable substrate guiding layers for block copolymer directed self-assembly (DSA) patterning*. SPIE: 2011; Vol. 7972, p 13.

9. Sharp, B. Materials for Next-Generation Lithography: Crosslinked Molecular Resists and Photopatternable Underlayers. Georgia Institute of Technology, 2018.

10. Blanc, A. and Bochet, C. G., Isotope effects in photochemistry. 1. o-Nitrobenzyl alcohol derivatives. *J Am Chem Soc* **2004,** *126* (23), 7174-7175.

11. Houlihan, F. M., Shugard, A., Gooden, R. and Reichmanis, E., Nitrobenzyl Ester Chemistry for Polymer Processes Involving Chemical Amplification. *Macromolecules* **1988,** *21* (7), 2001-2006.

12. Barltrop, J. A., Plant, P. J. and Schofield, P., Photosensitive Protective Groups. *Chem Commun* **1966,** (22), 822-+.

13. Klan, P., Solomek, T., Bochet, C. G., Blanc, A., Givens, R., Rubina, M., Popik, V., Kostikov, A. and Wirz, J., Photoremovable Protecting Groups in Chemistry and Biology: Reaction Mechanisms and Efficacy. *Chem Rev* **2013,** *113* (1), 119-191.

14. Chen, L., Goh, Y. K., Cheng, H. H., Smith, B. W., Xie, P., Montgomery, W., Whittaker, A. K. and Blakey, I., Aqueous developable dual switching photoresists for nanolithography. *Journal of Polymer Science Part A: Polymer Chemistry* **2012,** *50* (20), 4255-4265.

15. Schumers, J.-M., Fustin, C.-A., Can, A., Hoogenboom, R., Schubert, U. S. and Gohy, J.-F., Are o-nitrobenzyl (meth)acrylate monomers polymerizable by controlled-radical polymerization? *Journal of Polymer Science Part A: Polymer Chemistry* **2009,** *47* (23), 6504-6513.

16. Doh, J. and Irvine, D. J., Photogenerated Polyelectrolyte Bilayers from an Aqueous-Processible Photoresist for Multicomponent Protein Patterning. *J Am Chem Soc* **2004,** *126* (30), 9170-9171.

17. Han, E., Stuen, K. O., La, Y. H., Nealey, P. F. and Gopalan, P., Effect of Composition of Substrate-Modifying Random Copolymers on the Orientation of Symmetric and Asymmetric Diblock Copolymer Domains. *Macromolecules* **2008,** *41* (23), 9090-9097.

18. Wenzel, R. N., Surface Roughness and Contact Angle. *The Journal of Physical and Colloid Chemistry* **1949,** *53* (9), 1466-1467.

19. Suh, H. S., Nair, A., Delgadillo, P. R., Doise, J., Lorusso, G., Nealey, P., Monreal, V., Baskaran, D., Cao, Y., Padmanaban, M., Li, J., Kato, T., Sutani, T., Ishimoto, T., Ikota, M. and Koshihara, S., *Impact of annealing temperature on DSA process: toward faster assembly kinetics (Conference Presentation)*. SPIE: 2018; Vol. 10586.

20. Peng, Q., Tseng, Y. C., Darling, S. B. and Elam, J. W., Nanoscopic Patterned Materials with Tunable Dimensions via Atomic Layer Deposition on Block Copolymers. *Advanced Materials* **2010,** *22* (45), 5129-+.

21. Peng, Q., Tseng, Y. C., Darling, S. B. and Elam, J. W., Nanoscopic patterned materials with tunable dimensions via atomic layer deposition on block copolymers. *Abstr Pap Am Chem S* **2010,** *240*.

22. Tseng, Y. C., Peng, Q., Ocola, L. E., Elam, J. W. and Darling, S. B., Enhanced Block Copolymer Lithography Using Sequential Infiltration Synthesis. *J Phys Chem C* **2011,** *115* (36), 17725-17729.

23. Darling, S. B., Ramanathan, M., Peng, Q., Tseng, Y. C. and Elam, J. W., Self-assembly of metal-containing block copolymers and sequential infiltration synthesis of metal/block copolymer composites. *Abstr Pap Am Chem S* **2011,** *242*.

24. Peng, Q., Tseng, Y. C., Darling, S. B. and Elam, J. W., A Route to Nanoscopic Materials via Sequential Infiltration Synthesis on Block Copolymer Templates. *Acs Nano* **2011,** *5* (6), 4600-4606.

25. Tseng, Y. C., Peng, Q., Ocola, L. E., Czaplewski, D. A., Elam, J. W. and Darling, S. B., Enhanced polymeric lithography resists via sequential infiltration synthesis. *J Mater Chem* **2011,** *21* (32), 11722-11725.

26. Peng, Q., Tseng, Y. C., Long, Y., Mane, A. U., DiDona, S., Darling, S. B. and Elam, J. W., Effect of Nanostructured Domains in Self-Assembled Block Copolymer Films on Sequential Infiltration Synthesis. *Langmuir* **2017,** *33* (46), 13214-13223.

27. Detcheverry, F. A., Liu, G. L., Nealey, P. F. and de Pablo, J. J., Interpolation in the Directed Assembly of Block Copolymers on Nanopatterned Substrates: Simulation and Experiments. *Macromolecules* **2010,** *43* (7), 3446-3454.

28. Liu, C. C., Ramirez-Hernandez, A., Han, E., Craig, G. S. W., Tada, Y., Yoshida, H., Kang, H. M., Ji, S. X., Gopalan, P., de Pablo, J. J. and Nealey, P. F., Chemical Patterns

for Directed Self-Assembly of Lamellae-Forming Block Copolymers with Density Multiplication of Features. *Macromolecules* **2013,** *46* (4), 1415-1424.

29. Ikada, Y., Matsunaga, T. and Suzuki, M., *Overturn of Polar Groups on Polymer Surface*. 1985; Vol. 1985, p 1079-1086.

30. Mansky, P., Russell, T. P., Hawker, C. J., Pitsikalis, M. and Mays, J., Ordered diblock copolymer films on random copolymer brushes. *Macromolecules* **1997,** *30* (22), 6810-6813.

31. Stuen, K. O., In, I., Han, E., Streifer, J. A., Hamers, R. J., Nealey, P. F. and Gopalan, P., Imaging layers for the directed assembly of block copolymer films: Dependence of the physical and chemical properties of patterned polymer brushes on brush molecular weight. *J Vac Sci Technol B* **2007,** *25* (6), 1958-1962.

32. Evangelio, L., Fernandez-Regulez, M., Fraxedas, J., Muller, M. and Perez-Murano, F., Role of Penetrability into a Brush-Coated Surface in Directed Self-Assembly of Block Copolymers. *Acs Appl Mater Inter* **2019,** *11* (3), 3571-3581.

CHAPTER 6. SUMMARY AND RECOMMENDATIONS FOR FUTURE WORK

6.1 Summary

The challenges to developing resists that are capable of meeting the strict performance requirements at current and future technology nodes cannot be understated and have required a monumental amount of research from both academia and the semi-conductor manufacturing industry. Understanding the structure-property relationships in epoxide resists is critical for the prediction of patterning performance and the ability to rationally design resists capable of higher resolution patterning. New additives that can be added to any resist of this type to improve their performance will also be valuable tools in developing high performing resist formulations. Alternative technologies such as DSA will certainly be useful for specific lithographic applications such as flash memory patterning. This thesis details some of the efforts made towards these goals so far.

Chapter 2 describes the investigation into the effect of elevated loading of un-crosslinkable additives on the extent of conversion of the resist, and the design and synthesis of a series of PAGs that could be integrated into the network through epoxide-epoxide and epoxide-phenol crosslinking and which could be used at higher loadings. It was found that un-functionalized PAG decreased the extent of crosslinking in the resist when used at loadings above 10 mol. %, and two novel additives (TAS-3Ep-SbF_6 and TPS-OH-SbF_6) were reported which could be used at higher loadings (up to 100 % and 50 % respectively) without decreasing the extent of cross-linking. Using these PAGs at

moderately high loadings improved sensitivity under DUV and e-beam exposure sources, but was found to decrease sensitivity about 30 - 55 mol. % under e-beam but not DUV. Phenol functionalized PAGs were also found to have lower sensitivity than epoxide functionalized PAGs when exposing using e-beam, but the same sensitivity when exposing using DUV.

Chapter 3 describes two phenol functionalized additives, a photoacid generator (PAG) and a photodecomposable nucleophile (PDN), used to improve the resolution of negative tone epoxide resists through the addition of an additional phenol-epoxide chain-transfer like cross-linking mechanism. These additives were found to slow the overall rate of cross-linking and reduce the sensitivity of a model epoxide resist (4-Ep) when using both DUV (298 nm) and 100 keV e-beam exposure sources, and demonstrated reduced acid generation efficiency when using 100 keV e-beam lithography. At 15 mol. % loading the resolution of 4-Ep was improved from 35 nm down to 25 nm half-pitch features without the use of PDN, and 15 nm half-pitch features using 50 % PDN relative to the amount of PAG.

Chapter 4 describes efforts made to understand structure-property relationships in epoxide resists, specifically the effects of structural modifications on the glass transition temperature of the resist and the effects of glass transition temperatures on crosslinking and patterning performance. The introduction of aromatic rings to the core of each molecule was found to increase the glass transition temperature, as was the introduction of methyl groups ortho to the epoxide on the aromatic ring. Resists with the lowest Tg values demonstrated the most promising cross-linking behaviour (as measured by dose-response curves) having the largest NRT, sensitivity, and contrast, but could not resolve high

resolution features due to some combination of propagation of polymerization outside of exposed regions and/or the flow of partially cross-linked patterns during the PEB step. The relationship between structure and patterning performance proved to be more complex with moderate structural changes resulting in radically different patterning performances.

Chapter 5 describes the design of a non-chemically amplified photodefinable underlayer, NBn-*r*-BCB, which was derived from polyhydroxystyrene protected with a photolabile 2-nitrobenzyl protecting group. This underlayer was shown to be patternable by DUV light as well as e-beam lithography and was used as an underlayer for the unguided self-assembly of perpendicular lamellae of PS-b-PMMA, although perpendicular lamellae could not be successfully self-assembled on the underlayer following e-beam patterning.

6.2 Recommendations for Future Work

As discussed in Chapters 2 and 3, there appears to be a change in acid generation efficiency unique to high energy exposure sources between both functionalized and un-functionalized photoacid generators as well as when using high (> 30 %) PAG loadings. It would be helpful to directly measure the acid generation efficiency of these new PAGs as well as their efficiency as a function of loading instead of inferring information from dose-response curves. A simple method for doing so would be using on-wafer ellipsometry to determine the absorption of an acid sensitive Courmarin 6 (C6) dye that could be blended into resist formulations.[1] This could provide some insight into the acid generation mechanisms when using EUV and e-beam lithography which are currently poorly understood. Process and loading optimization studies would also be helpful to determine the ultimate resolution of 4-Ep using the novel additives developed.

The first generation non-chemically amplified photo-definable underlayer reported showed promising initial results, but could not assemble guided lamellae using e-beam lithography. Modifying the surface chemistry through the incorporation of a third monomer such as polystyrene or adjusting the percentage of BCB monomer in the underlayer composition is necessary to expand the process window and allow for the formation of lamellae. Additionally, it would be useful to study the effect of the amount of BCB on the cure shrinkage and surface roughness to allow for the thermal annealing of block copolymers at higher temperatures. While the initial underlayer design was based on the deprotection of polyhydroxystyrene, designs based on the deprotection of polymethylmethacrylate[2] would likely have a faster etch rate and be more useful for implementation in high-volume nanofabrication. A dose response curve would also be helpful to determine the optimal dose for writing guiding patterns.

Nitrobenzyl groups are the most commonly used photolabile protecting group, however they form potentially toxic and strongly absorbing byproducts such as o-nitrosobenzaldehyde.[3] It would be advantageous to explore other photolabile groups capable of releasing phenol such as 3,5-dimethoxybenzoin (DMB).[4]

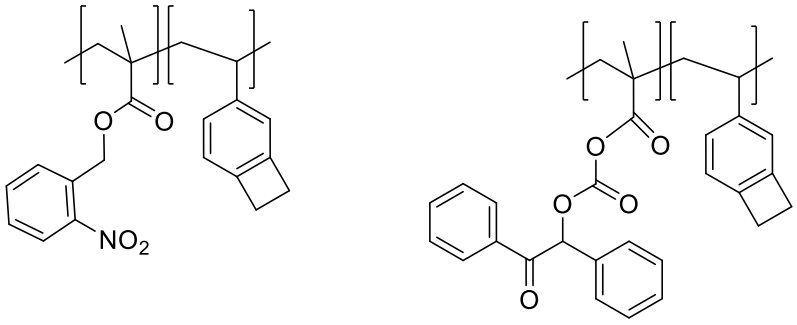

Figure 6.1 Second generation designs of a non-chemically amplified directly photo-definable underlayer for DSA.

6.3 References

1. Lee, C.-T., Yueh, W., Roberts, J., R. Younkin, T. and Henderson, C., *A new technique for studying photo-acid generator chemistry and physics in polymer films using on-wafer ellipsometry and acid-sensitive dyes*. 2008; Vol. 6923.

2. Doh, J. and Irvine, D. J., Photogenerated Polyelectrolyte Bilayers from an Aqueous-Processible Photoresist for Multicomponent Protein Patterning. *J Am Chem Soc* **2004,** *126* (30), 9170-9171.

3. Klán, P., Šolomek, T., Bochet, C. G., Blanc, A., Givens, R., Rubina, M., Popik, V., Kostikov, A. and Wirz, J., Photoremovable Protecting Groups in Chemistry and Biology: Reaction Mechanisms and Efficacy. *Chem Rev* **2013,** *113* (1), 119-191.

4. Pirrung, M. C. and Bradley, J.-C., Dimethoxybenzoin Carbonates: Photochemically-Removable Alcohol Protecting Groups Suitable for Phosphoramidite-Based DNA Synthesis. *The Journal of Organic Chemistry* **1995,** *60* (5), 1116-1117.

CHAPTER 7. APPENDIX: CHARACTERIZATION DATA

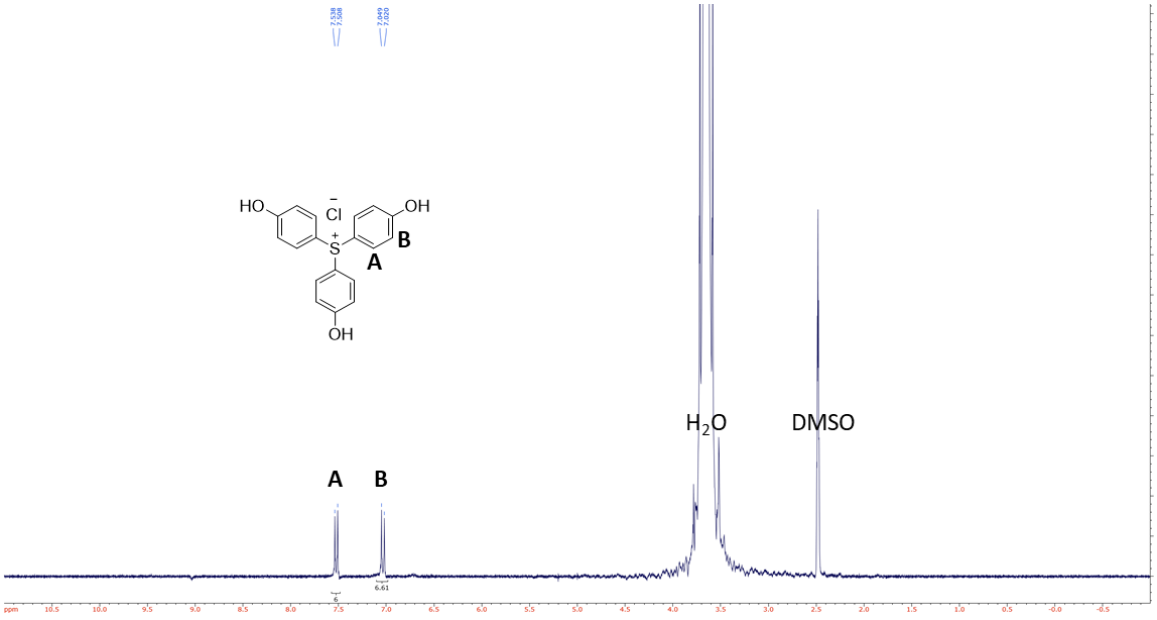

Figure 7.1 ^{1}H NMR (300 MHz) spectrum of TPS-OH-Cl in DMSO-d6.

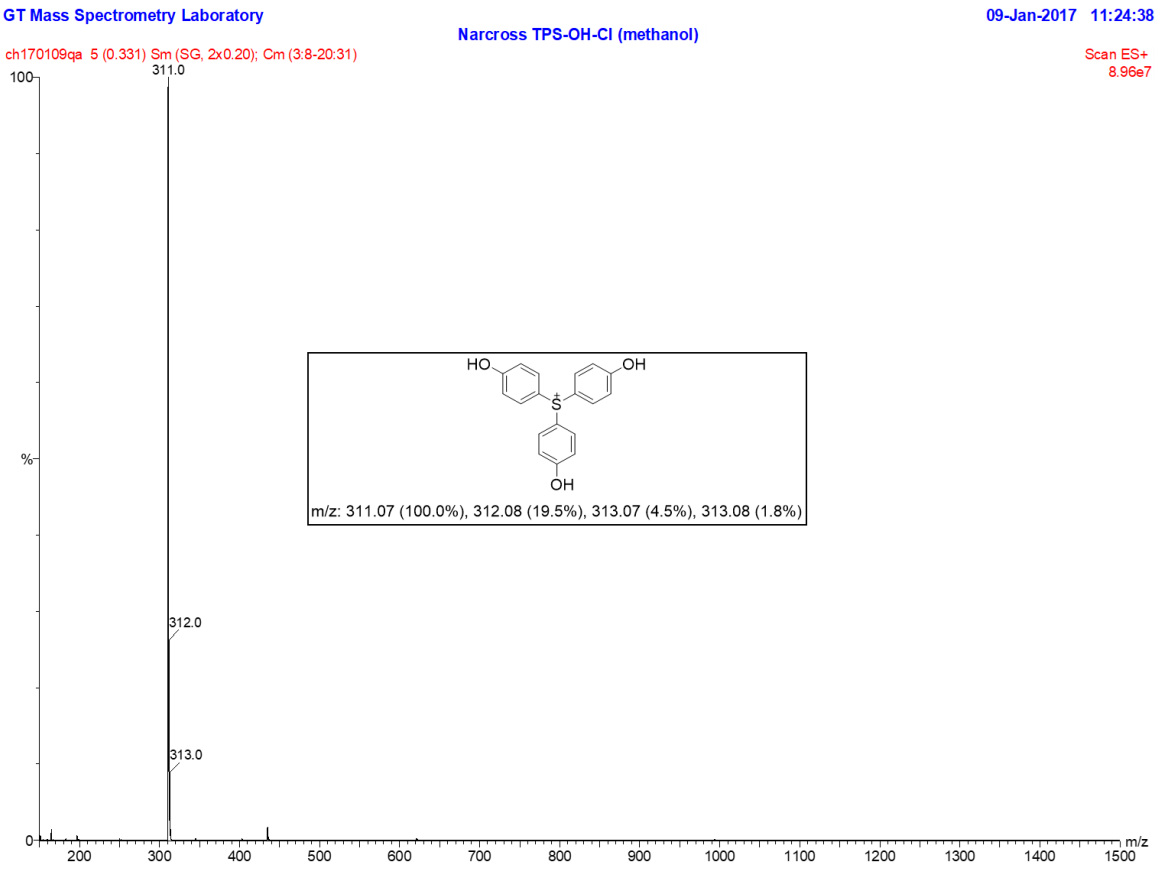

Figure 7.2 Positive ion ESI mass spectrum of TPS-OH-Cl.

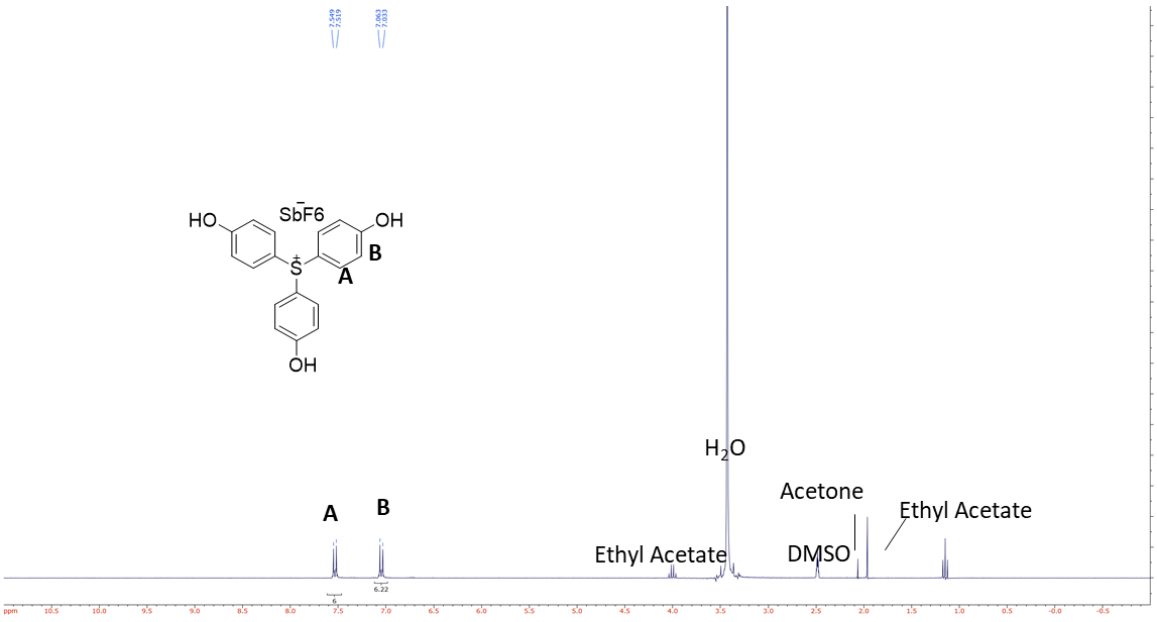

Figure 7.3 ^{1}H NMR (300 MHz) spectrum of TPS-OH-SbF_6 in DMSO-d6.

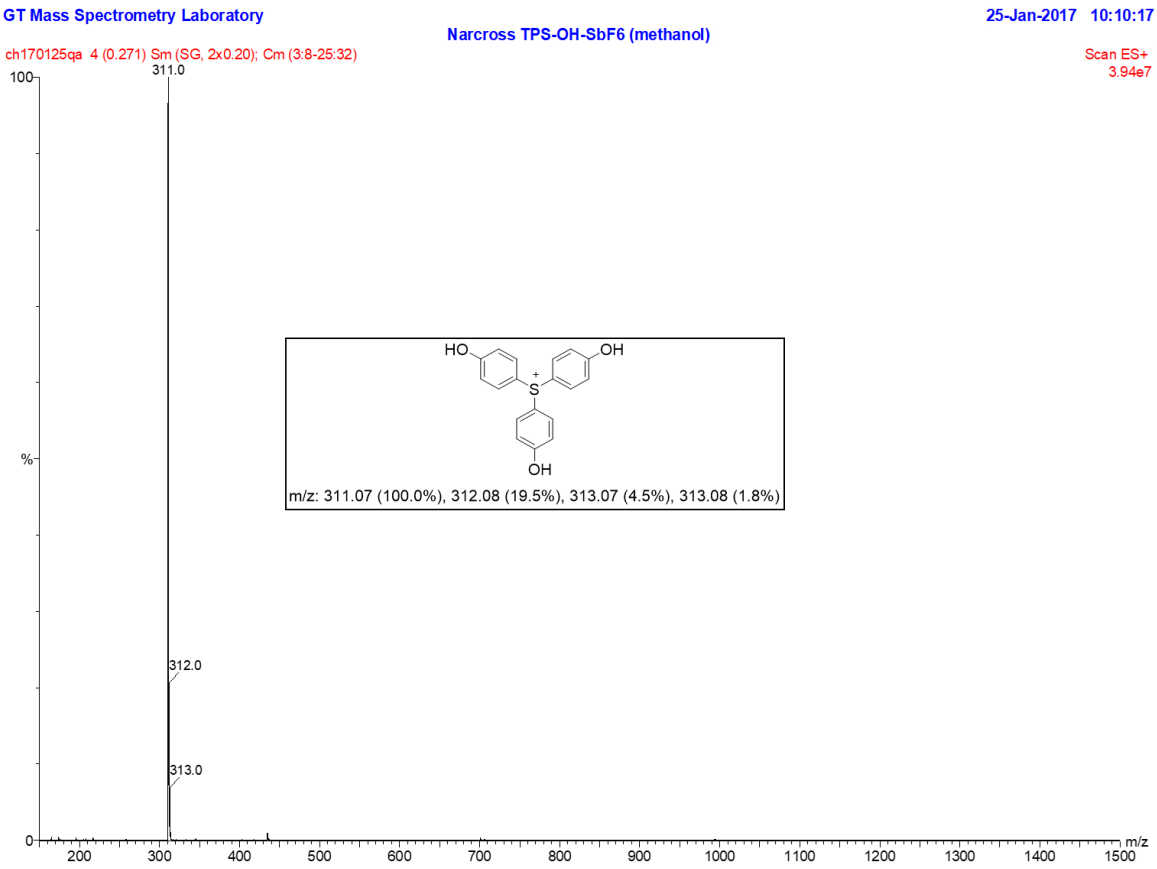

Figure 7.4 Positive ion ESI mass spectrum of TPS-OH-SbF_6.

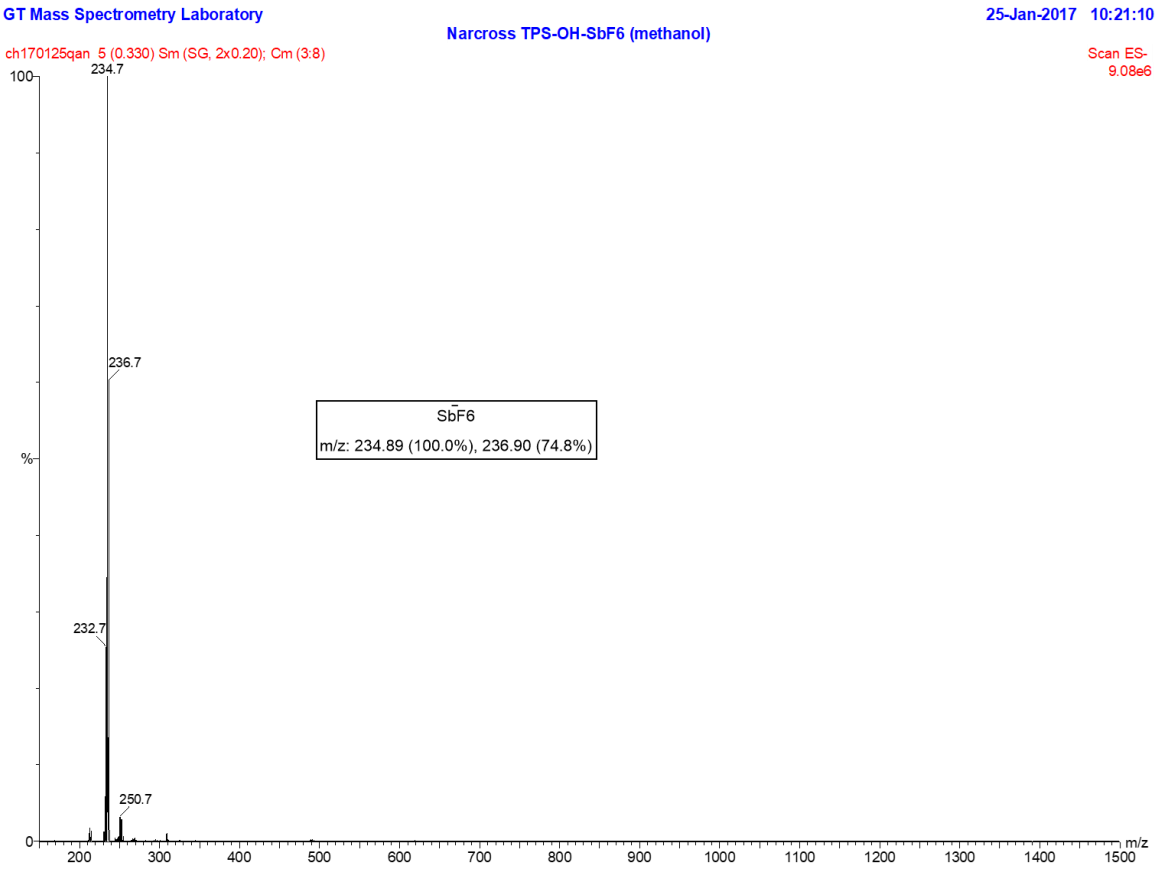

Figure 7.5 Negative ion ESI mass spectrum of TPS-OH-SbF_6.

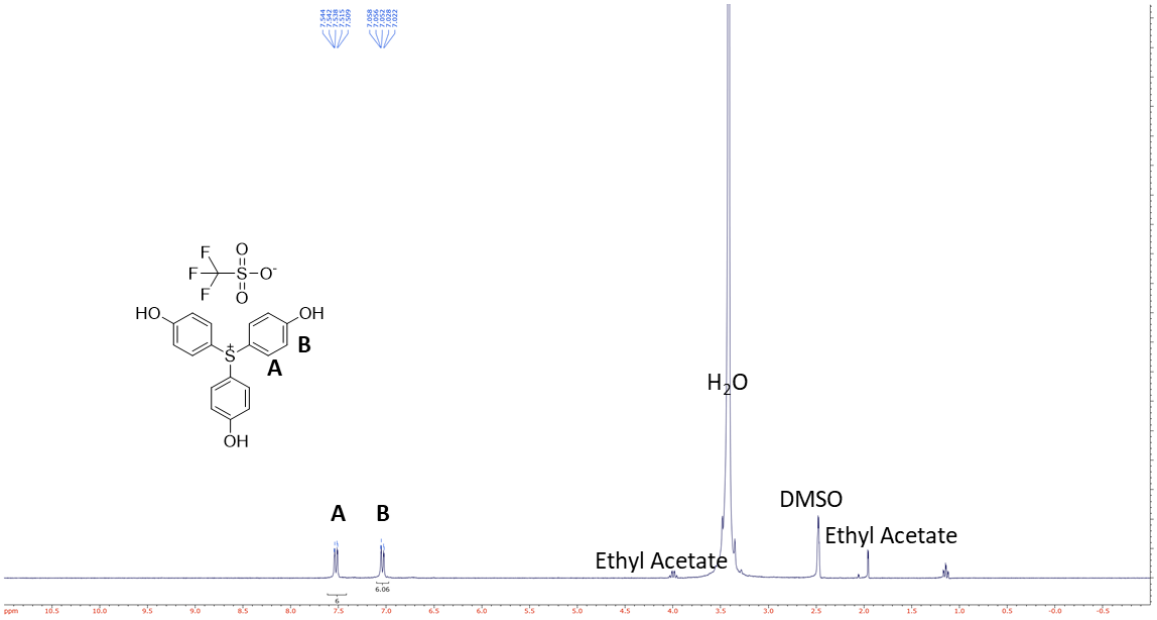

Figure 7.6 ^{1}H NMR (300 MHz) spectrum of TPS-OH-Tf in DMSO-d6.

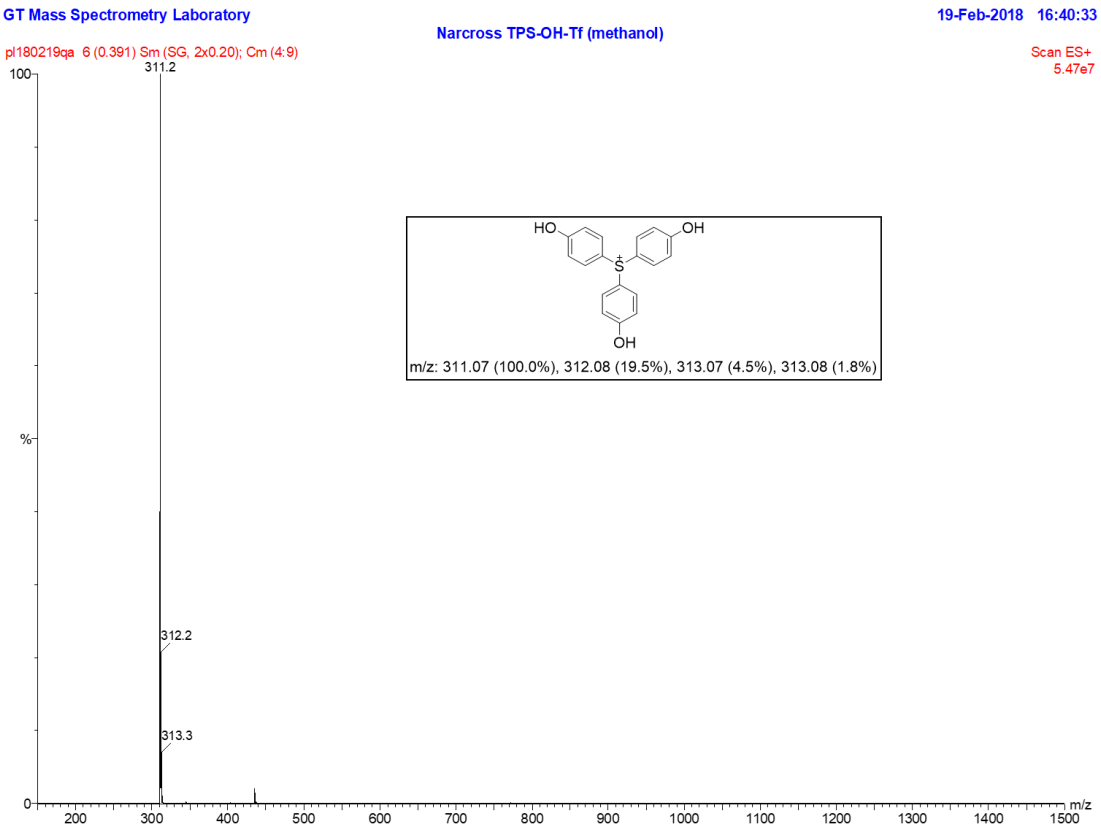

Figure 7.7 Positive ion ESI mass spectrum of TPS-OH-Tf.

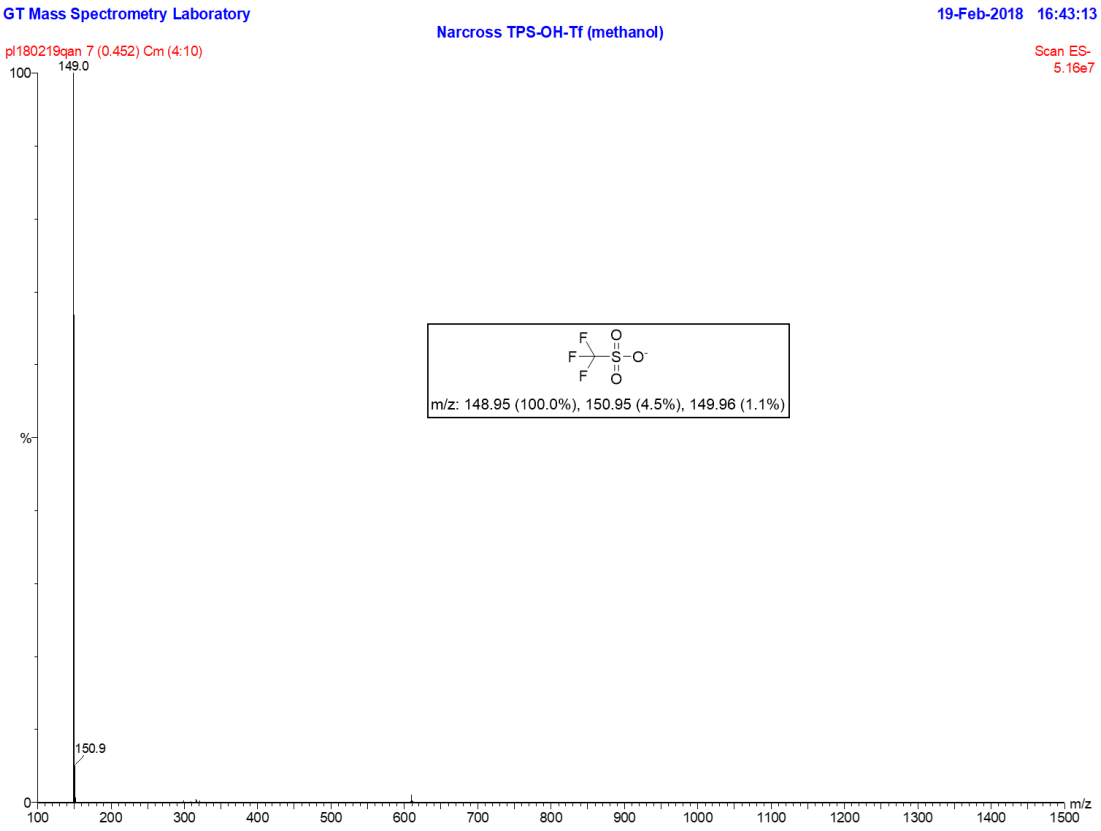

Figure 7.8 Negative ion ESI mass spectrum of TPS-OH-Tf.

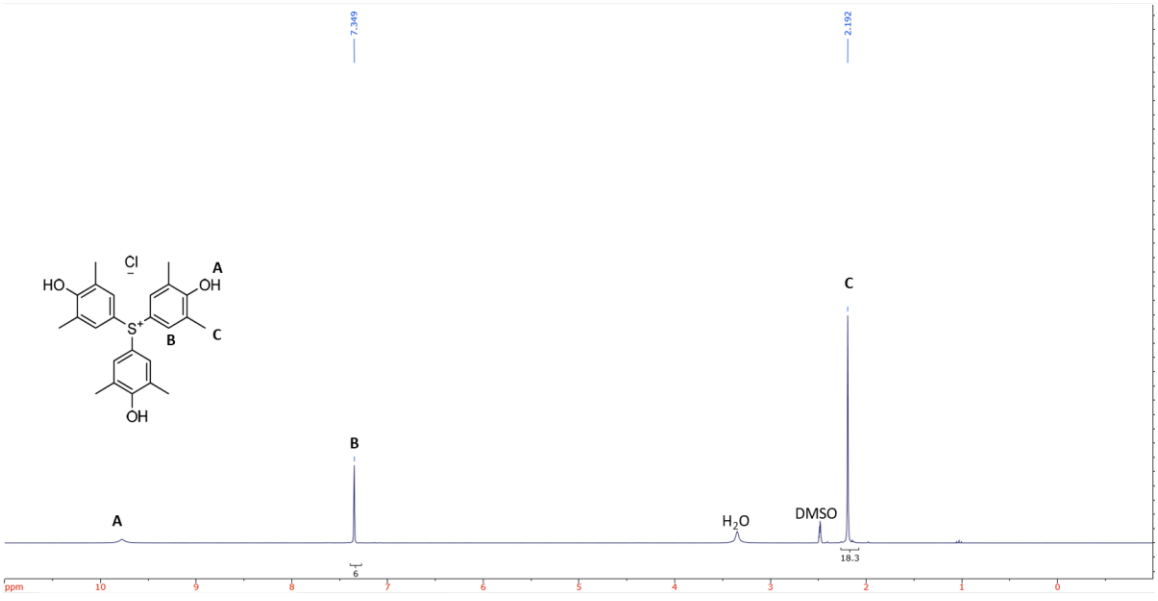

Figure 7.9 ^{1}H NMR (300 MHz) spectrum of TAS-OH-Cl in DMSO-d6.

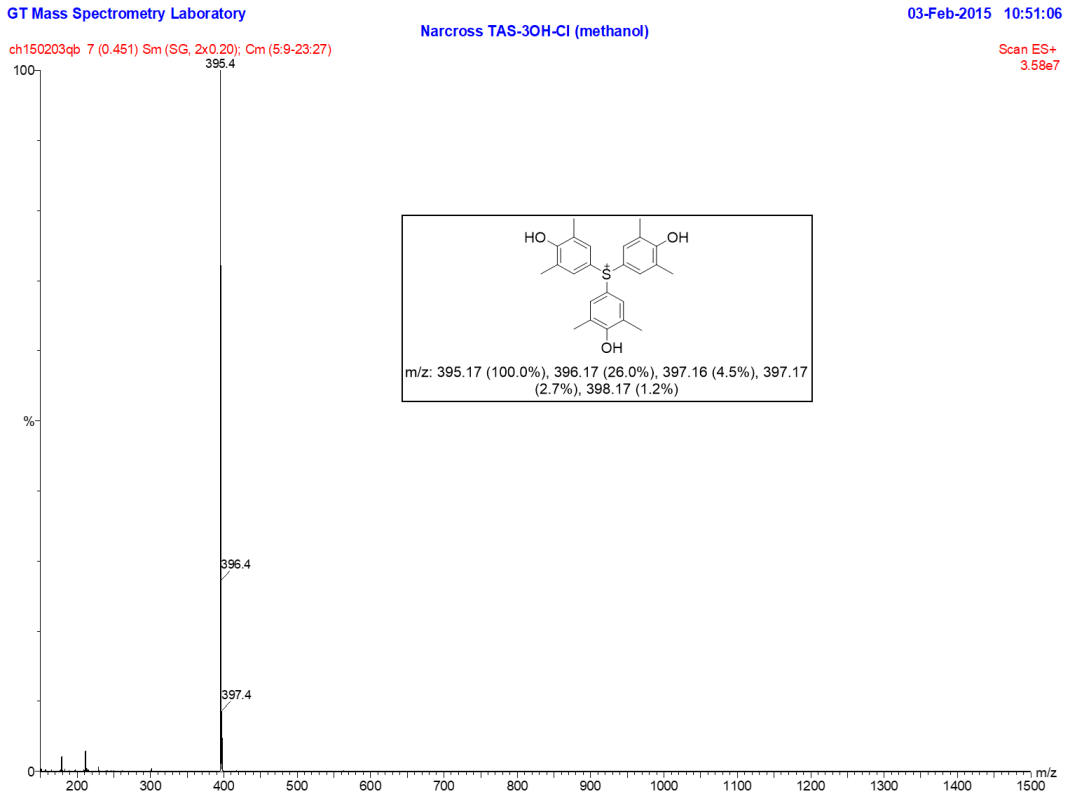

Figure 7.10 Positive ion ESI mass spectrum of TAS-OH-Cl.

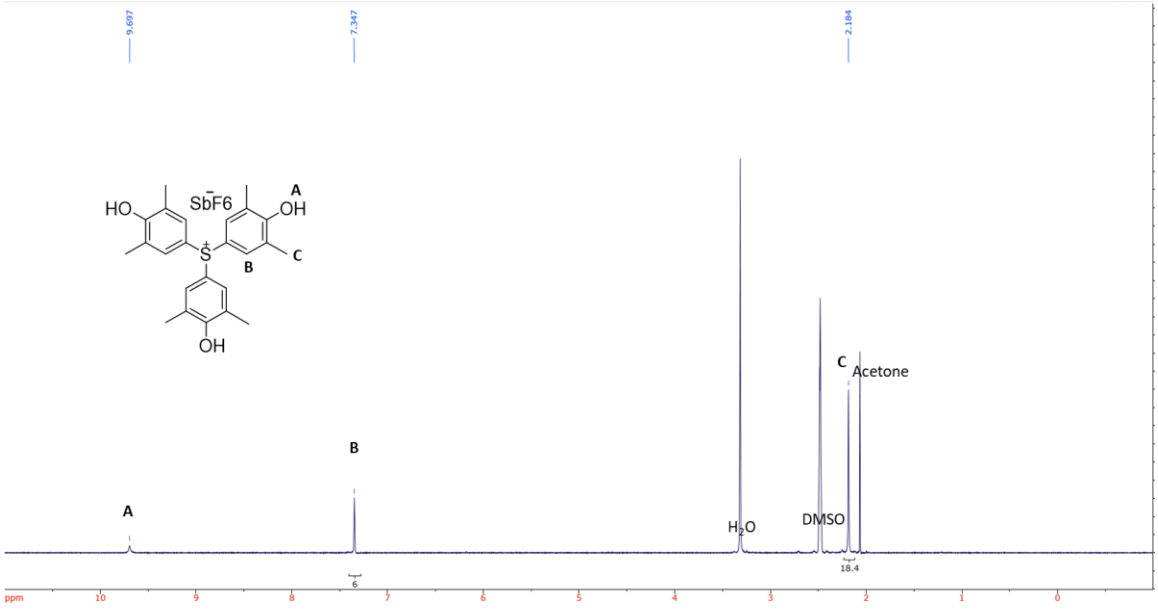

Figure 7.11 ^{1}H NMR (300 MHz) spectrum of TAS-OH-SbF_6 in DMSO-d6.

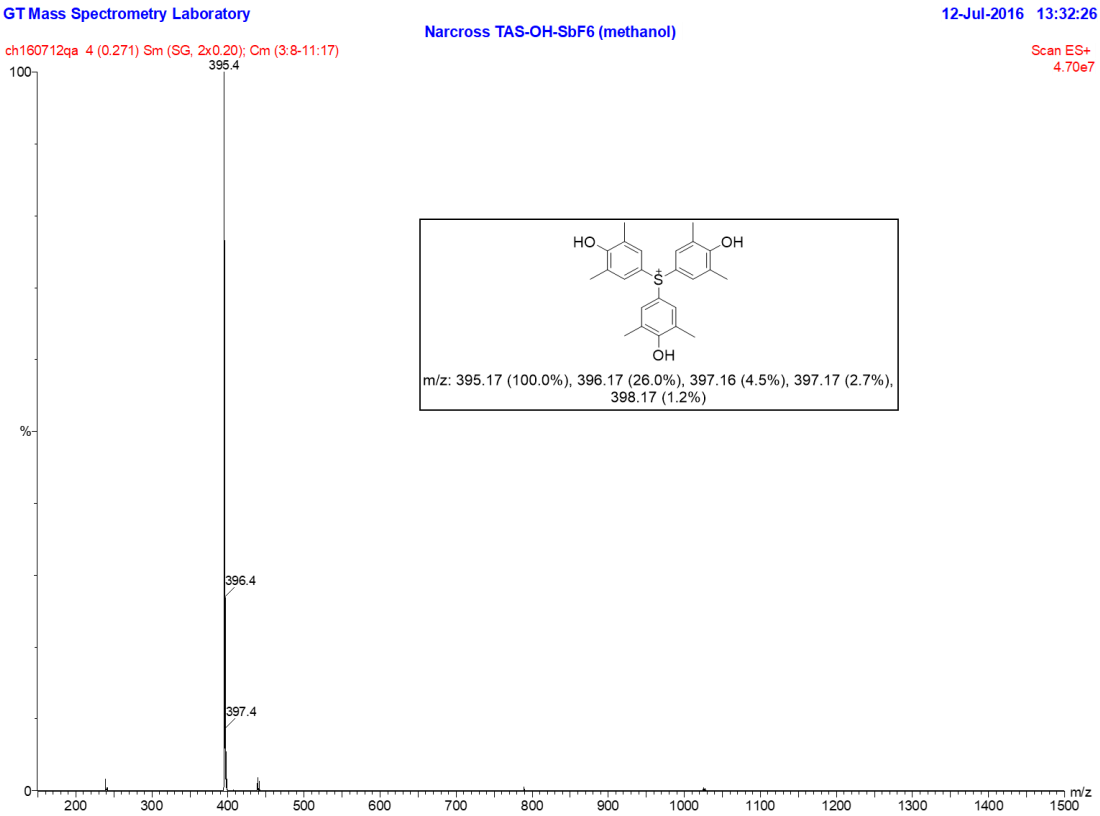

Figure 7.12 Positive ion ESI mass spectrum of TAS-OH-SbF_6.

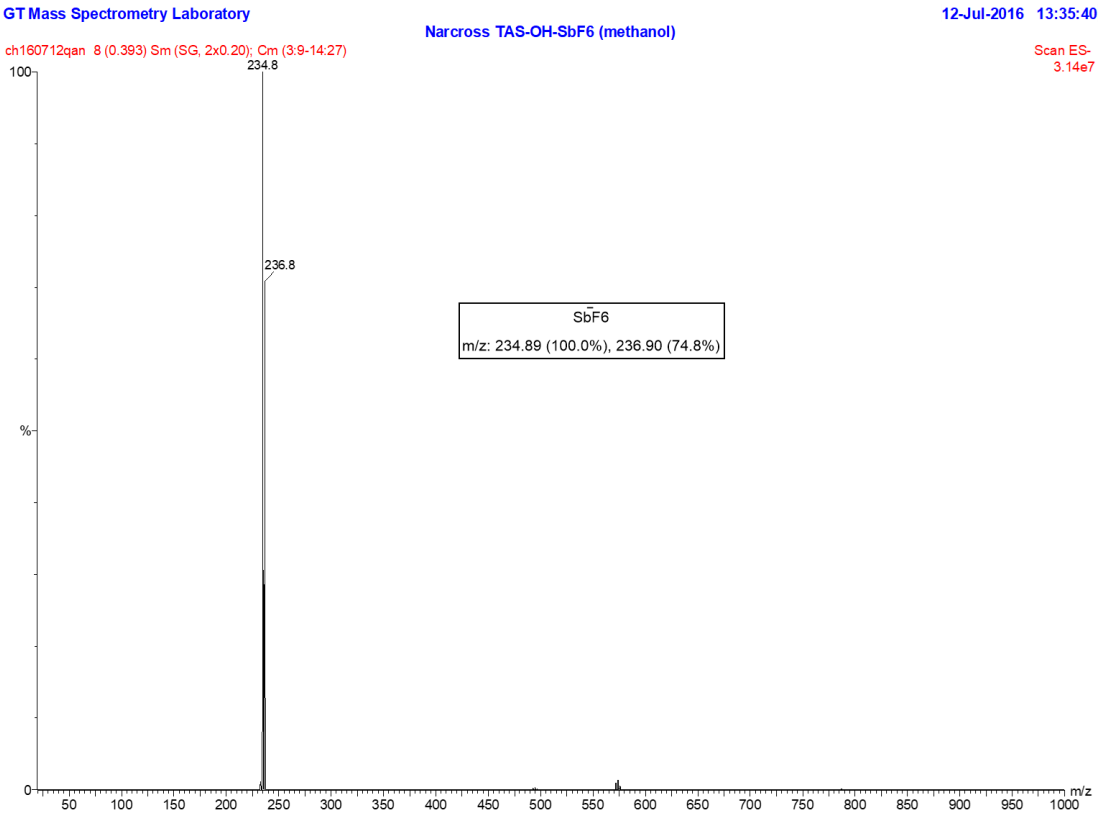

Figure 7.13 Negative ion ESI mass spectrum of TAS-OH-SbF_6.

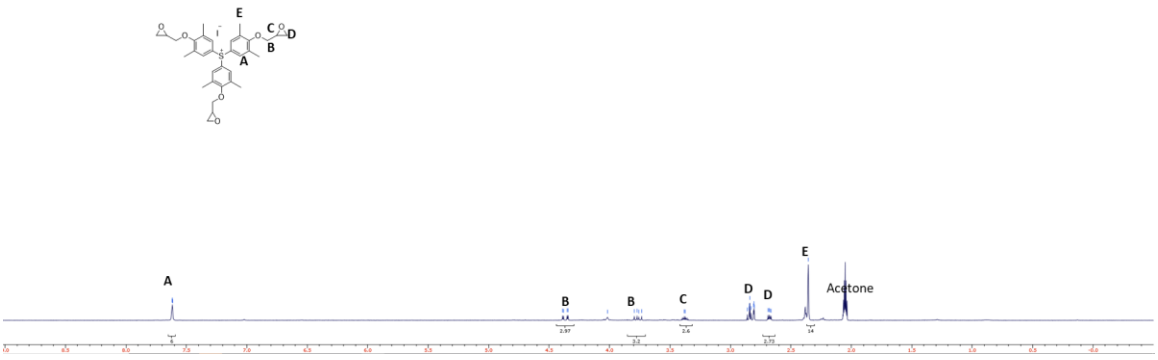

Figure 7.14 ^{1}H NMR (300 MHz) spectrum of TAS-3Ep-I in Acetone-d_6.

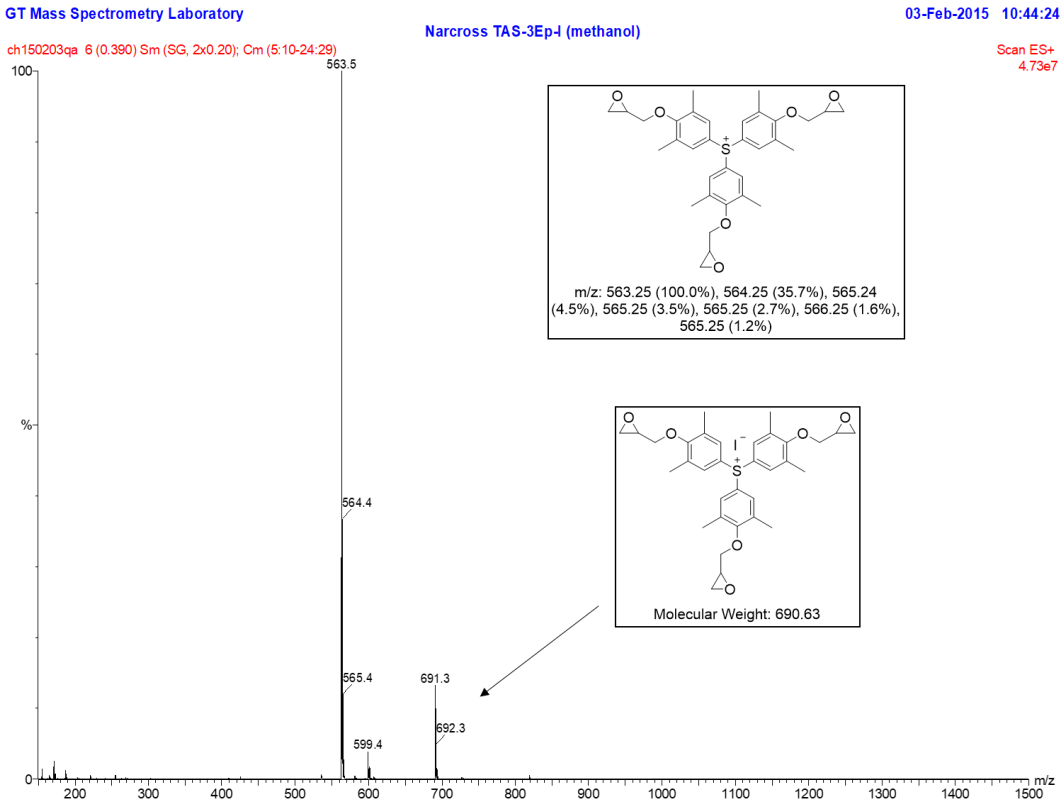

Figure 7.15 Positive ion ESI mass spectrum of TAS-3Ep-I.

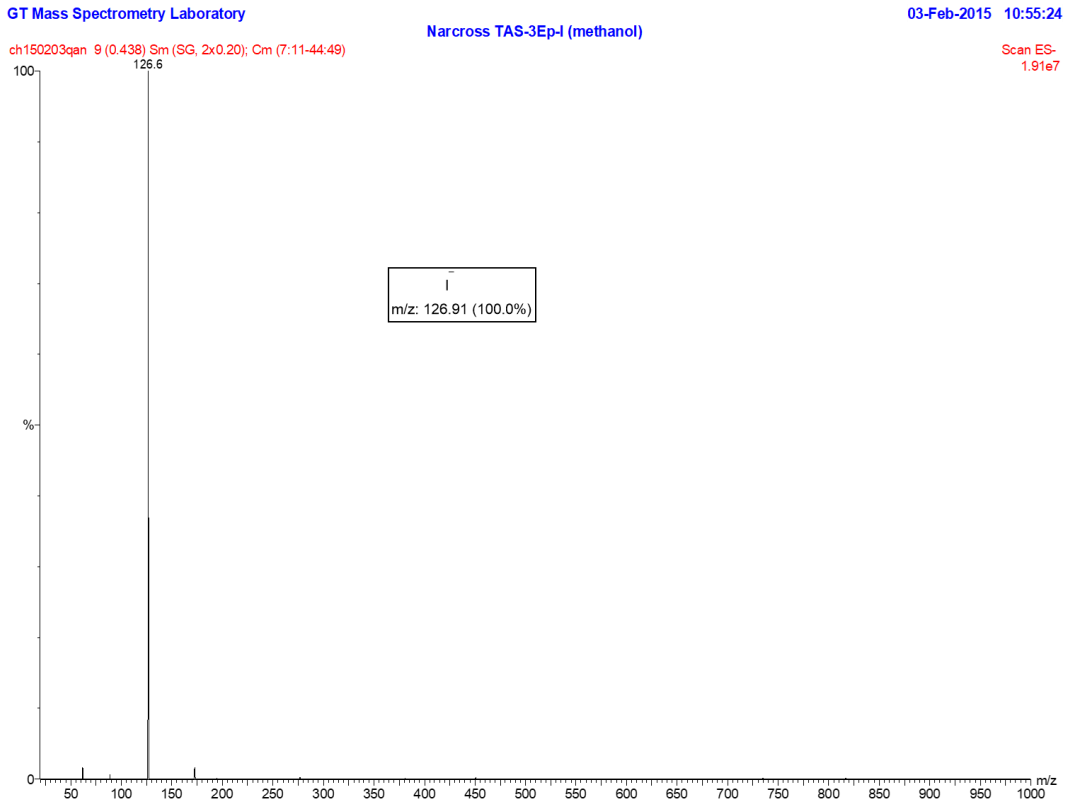

Figure 7.16 Negative ion ESI mass spectrum of TAS-3Ep-I.

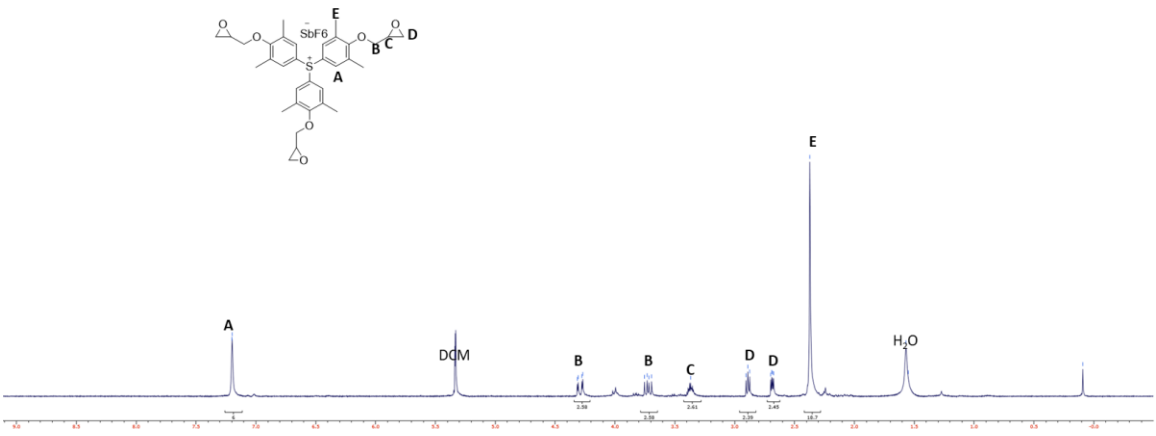

Figure 7.17 ^{1}H NMR (300 MHz) spectrum of TAS-3Ep-SbF_6 in CD_2Cl_2.

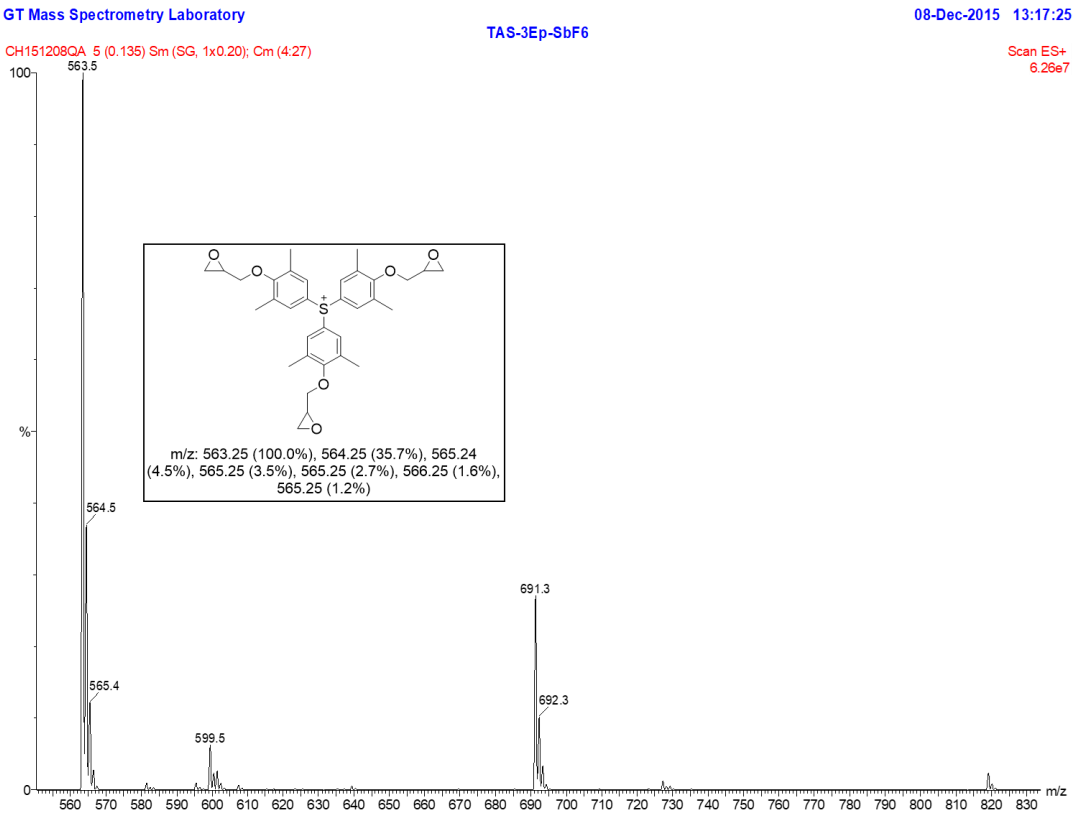

Figure 7.18 Positive ion ESI mass spectrum of TAS-3Ep-SbF_6.

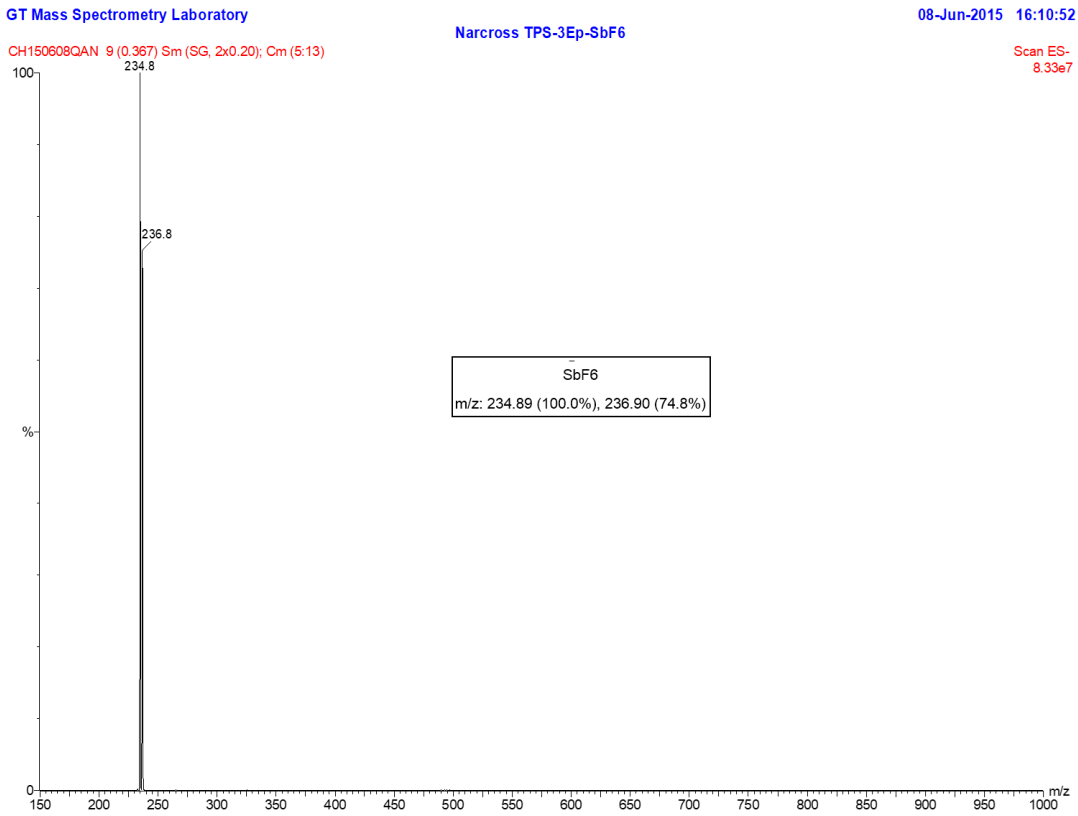

Figure 7.19 Negative ion ESI mass spectrum of TAS-3Ep-SbF_6.

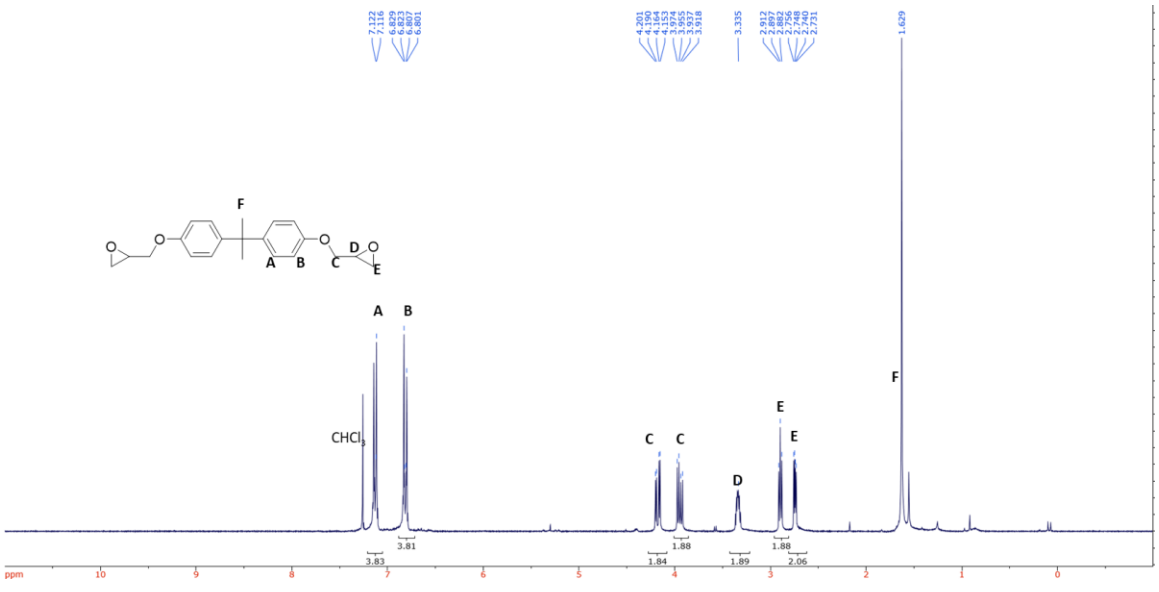

Figure 7.20 ^{1}H NMR (300 MHz) spectrum of BPA-2Ep in $CDCl_3$.

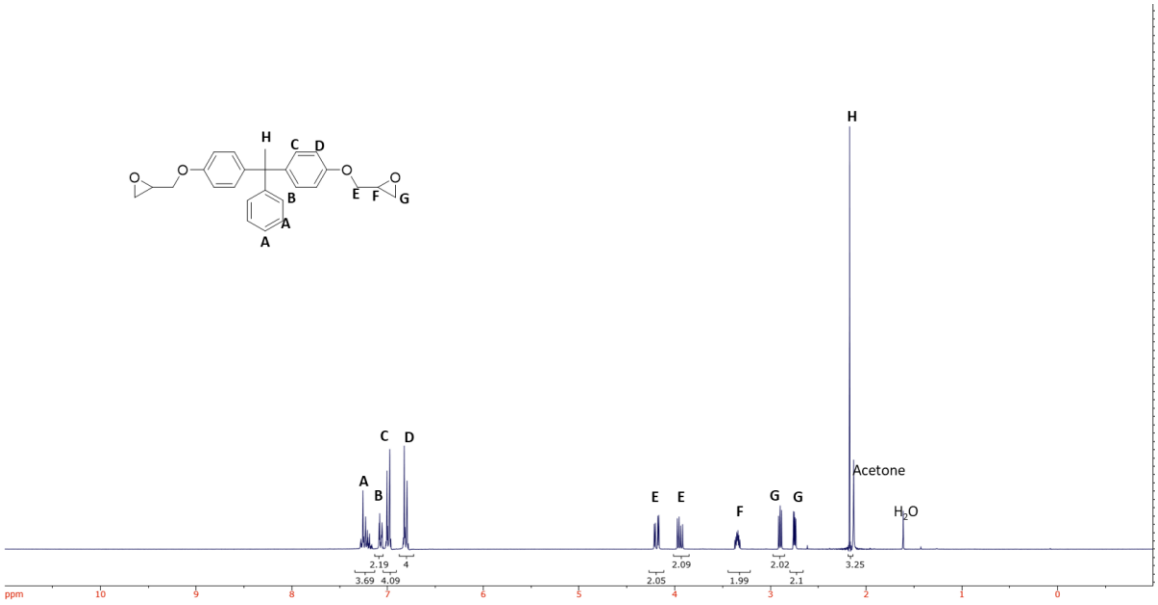

Figure 7.21 ^{1}H NMR (300 MHz) spectrum of BPAP-2Ep in $CDCl_3$.

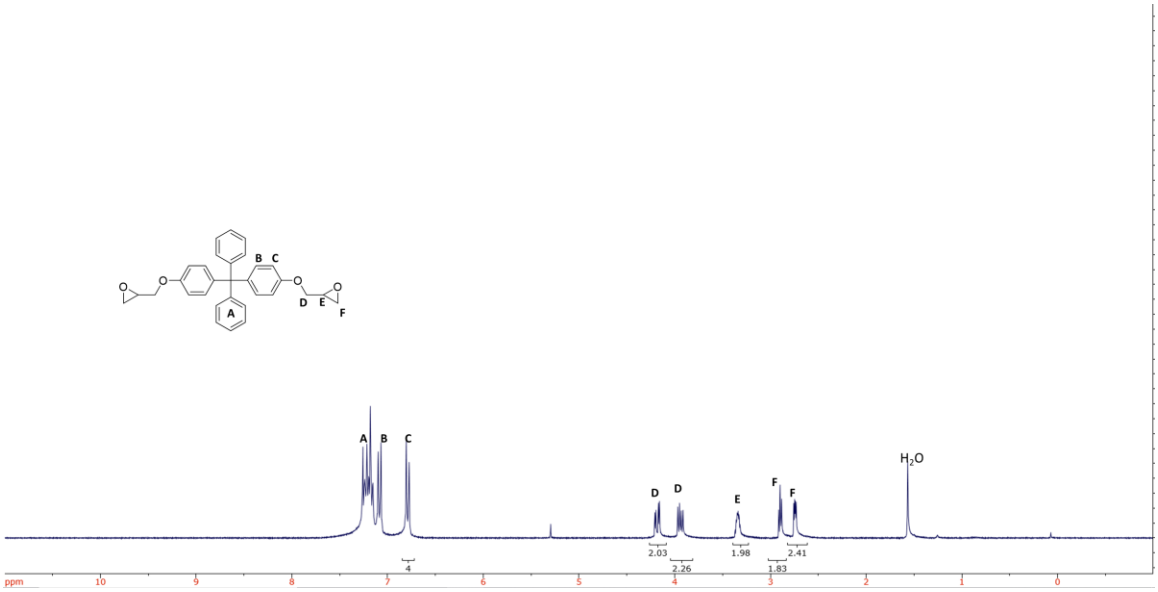

Figure 7.22 ^{1}H NMR (300 MHz) spectrum of BPBP-2Ep in $CDCl_3$.

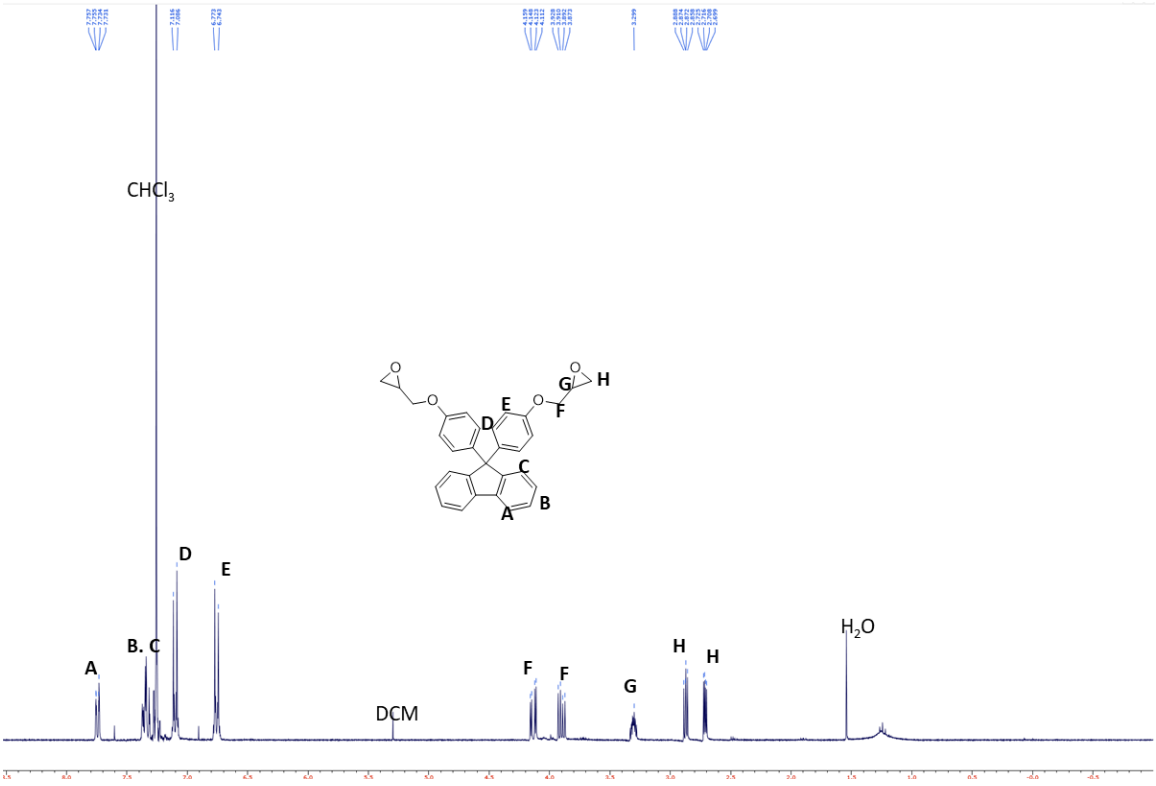

Figure 7.23 ^{1}H NMR (300 MHz) spectrum of BHPF-2Ep in $CDCl_3$.

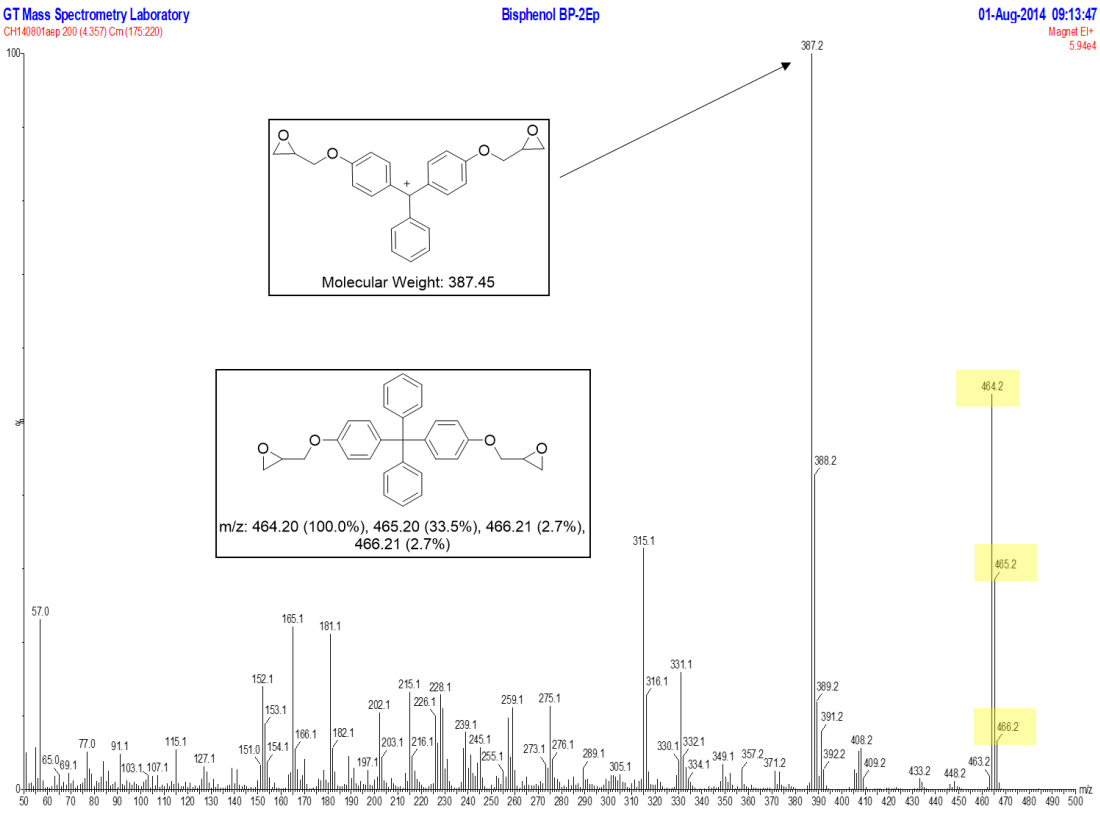

Figure 7.24 EI mass spectrum of BPBP-2Ep.

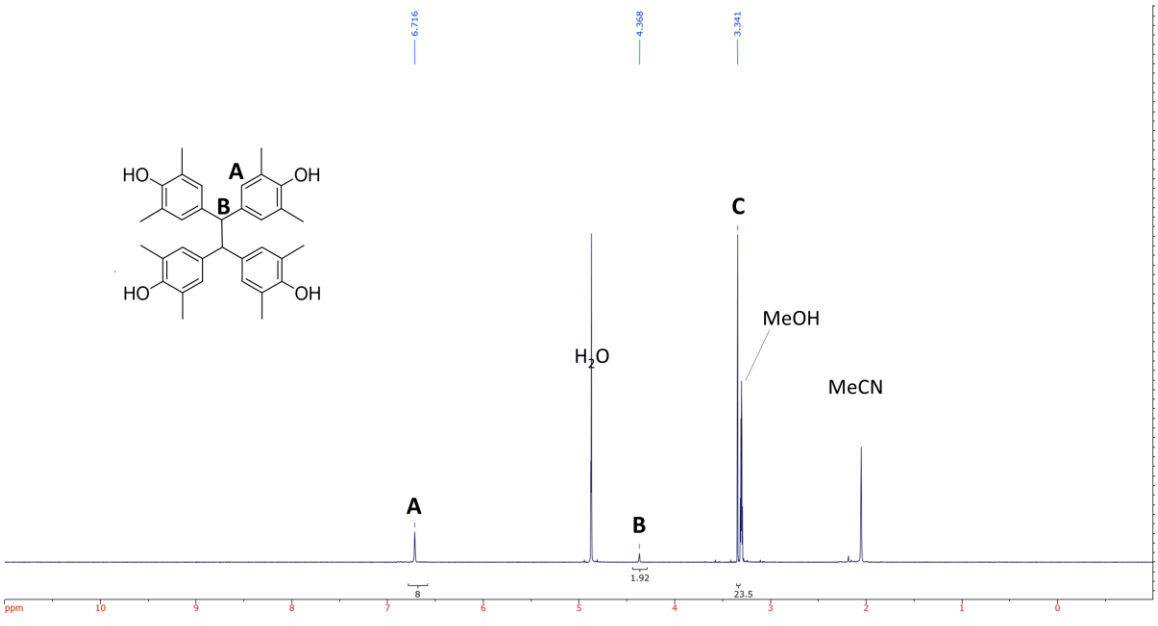

Figure 7.25 ^{1}H NMR (300 MHz) spectrum of TPOE-2M-4OH in CD_3OD.

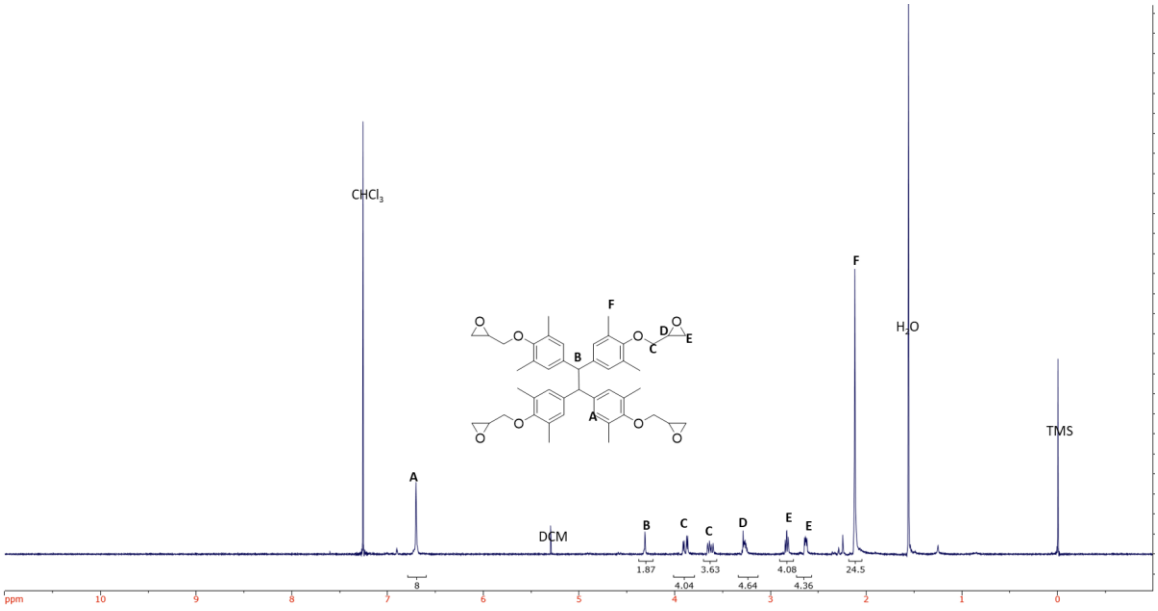

Figure 7.26 ^{1}H NMR (300 MHz) spectrum of TPOE-2M-4Ep in $CDCl_3$.

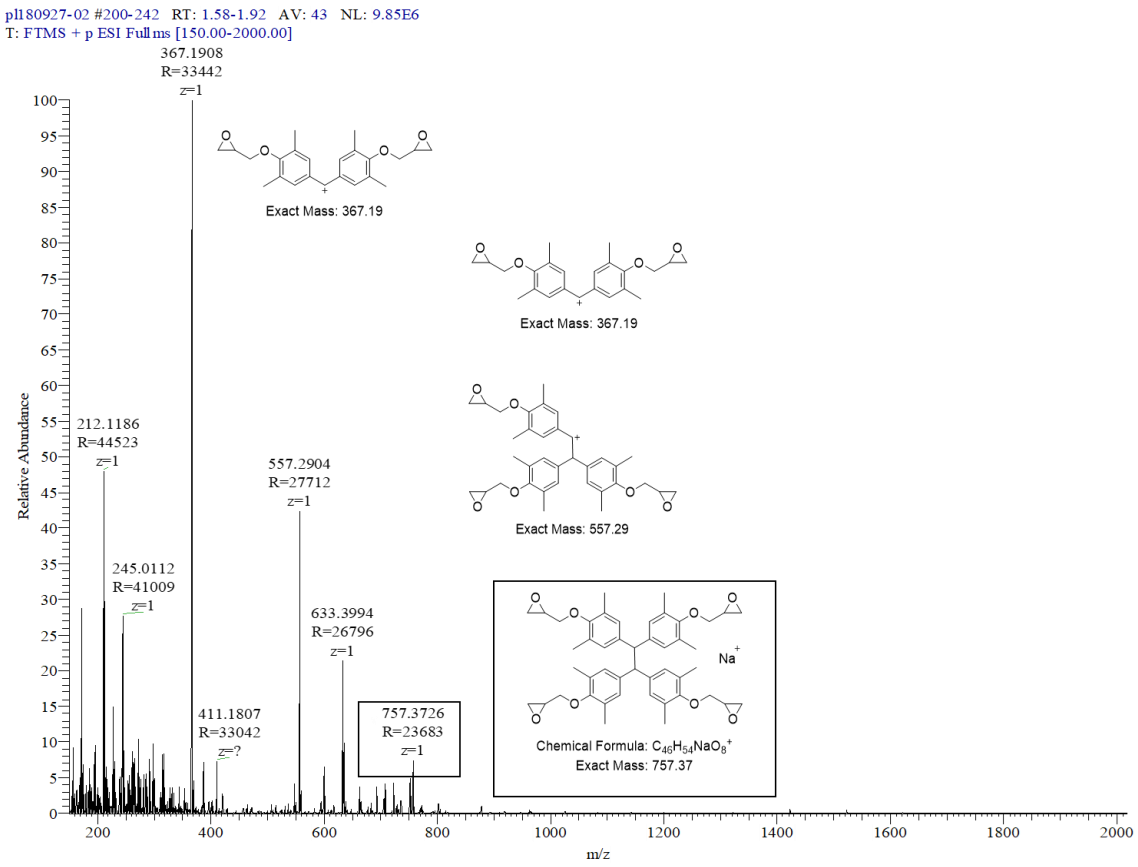

Figure 7.27 Positive ion ESI mass spectrum of TPOE-2M-4Ep.

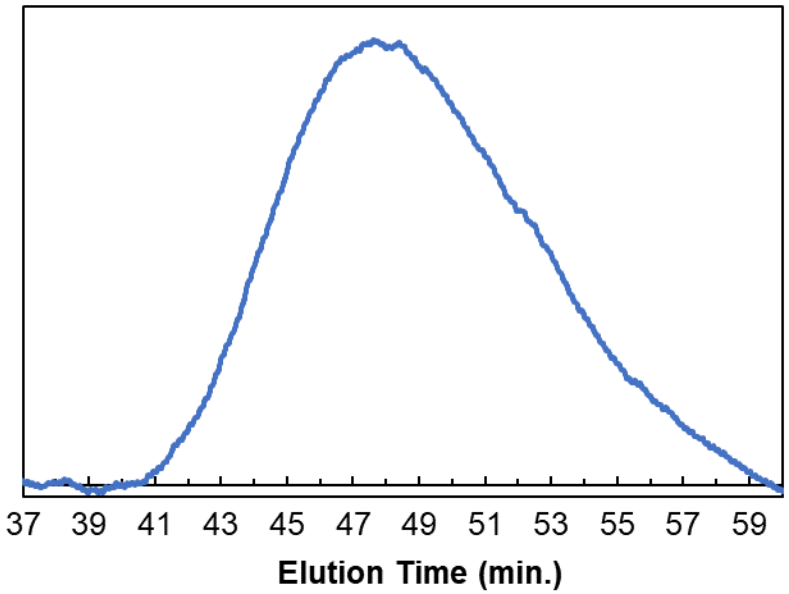

Figure 7.28 GPC trace of AS-*r*-BCB M_w = 40,900 g/mol; PDI = 1.6.

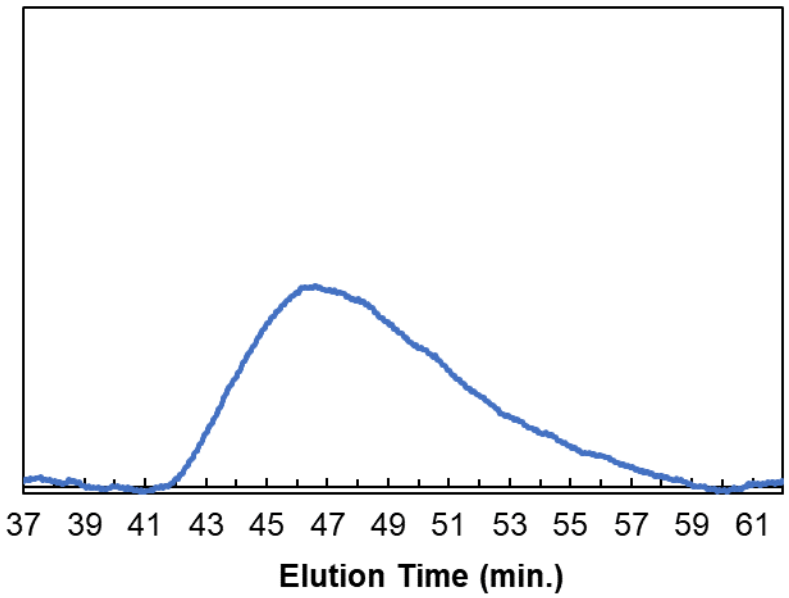

Figure 7.29 GPC trace of NBn-*r*-BCB M_w = 43,500 g/mol; PDI = 1.5.